Quasi-free Pi0 and Pi- electroproduction on 4He in the Delta-resonance region (Pi en Delta in symbolen) - Zie als voorbeeld titelblad -

Steenbakkers, M.F.M.

2004

document version
Publisher's PDF, also known as Version of record

Quasi-free π^0 and π^- electroproduction on ^{4}He in the Δ-resonance region

Martijn Steenbakkers

The work described in this thesis is part of the research programme of the "Stichting voor Fundamenteel Onderzoek der Materie (FOM)", which is financially supported by the "Nederlandse Organisatie voor Wetenschappelijk Onderzoek (NWO)"

VRIJE UNIVERSITEIT

Quasi-free π^0 and π^- electroproduction on ^{4}He in the Δ-resonance region

ACADEMISCH PROEFSCHRIFT

ter verkrijging van de graad van doctor aan
de Vrije Universiteit Amsterdam,
op gezag van de rector magnificus
prof.dr. T. Sminia,
in het openbaar te verdedigen
ten overstaan van de promotiecommissie
van de faculteit der Exacte Wetenschappen
op woensdag 21 januari 2004 om 15.45 uur
in de aula van de universiteit,
De Boelelaan 1105

door

Martijn Franciscus Maria Steenbakkers

geboren te Uden

promotor:	prof.dr. G. van Middelkoop
copromotoren:	dr. H.P. Blok
	dr.ir. W.H.A. Hesselink

Contents

1 Introduction

The constituents of atomic nuclei, protons and neutrons, are bound by the 'strong' nucleon-nucleon interaction. At the nucleon level this force is described by the exchange of (virtual) mesons. Nucleons, other baryons, and mesons are composite particles as well. They consist of point-like quarks, bound by the strong force, which is mediated by the exchange of (massless) gluons. The strongly interacting quarks and gluons in nucleons and mesons are described within the Quantum Chromo Dynamics (QCD) quantum field theory. In principle, also the strong force between nucleons and that between nucleons and mesons can be described by the exchange of gluons. However, no QCD based models exist yet that successfully describe the strong interaction at the energy scale of the nucleon-nucleon interactions in atomic nuclei, not even for the smallest systems. Instead, many phenomena on the scale of the nucleon mass have been described successfully by effective theories based on the exchange of mesons. In this respect the excitation and the decay of the Delta is particularly interesting.

The Delta is the baryon resonance with the smallest energy and it consists of the same quarks as the nucleon. The Delta can be excited in the interaction of a nucleon with a real or virtual photon, in a nucleon-nucleon interaction and in a pion-nucleon interaction. Excitation of the Delta implies recoupling of the spins of the quarks. In the nucleon the three quarks, each with spin $\frac{1}{2}\hbar$, are coupled to a total spin $S = \frac{1}{2}\hbar$. In the excitation of a Delta through a photo-nucleon interaction a total angular momentum of $1\hbar$ is transferred to the nucleon, leading to a total spin of $S = \frac{3}{2}\hbar$ (spin flip of one of the quarks).

The isospin of the Delta is $T = \frac{3}{2}$ and the corresponding isospin quadruplet consists of the charge states Δ^{++}, Δ^{+}, Δ^{0} and Δ^{-}. In photo-nucleon interactions on the proton and neutron only the Δ^{+} and Δ^{0} are created, respectively. The Delta has a very short lifetime. A free Delta decays almost exclusively ($> 99\%$) into a nucleon and a pion. In a nucleus, the Delta can also decay through the interaction with a nucleon. In this case no pion is emitted.

There are significant differences between cross sections for photoproduction of neutral and charged pions on a nucleon. Whereas the cross sections for the

reactions $\gamma + N \rightarrow \pi^0 + N$ (N being a proton or a neutron) reflect the characteristic features of intermediate Delta excitation, those for the reactions $\gamma + N \rightarrow \pi^{\pm} + N$ show in addition large contributions from non-resonant interactions (Born terms). Therefore, neutral pion production on a free nucleon and on a nucleon bound in a nucleus are of particular interest for studying the properties of the Delta.

Various approaches have been made to calculate the amplitude for electromagnetically induced pion production. They include dispersion calculations [Che57], calculations in the framework of an effective Lagrangian [Pec69, Ols75], dynamical models including off-shell effects [Noz90], and fully relativistic calculations [Dav91, Car94, Vdh95a].

The properties of the Δ-resonance excited on a free nucleon have been measured to great detail in various γN and πN reactions. However, much less is known about excitation of the Delta in a nucleus, and particularly about the $N\Delta$ interaction in nuclei. The differential cross sections for pion production by a real or virtual photon on nucleons bound in a nucleus differ from those on a free nucleon, because in a nuclear medium the production amplitudes are modified by the strong NN, πN and $N\Delta$ interactions. The Delta plays a prominent role in these interactions. Hence, a proper understanding of this interaction is of great importance for studies of any reaction involving mesons, nucleons and nuclei.

Medium modifications of the Δ-propagator were calculated for the first time within the Δ-hole model [Hir79, Ose79, Koc84, Tak88], and references therein. The total cross sections for photoabsorption and the cross sections for quasi-free charged pion production for the doubly closed shell nuclei ^{4}He and ^{16}O are satisfactorily reproduced by these calculations [Koc84].

More recently, two models were developed for quasi-free pion photoproduction (electroproduction) on nuclei in the Δ-resonance region [Vdh95b, Lee97]. In ref. [Vdh95b] a non-relativistic pion-production operator, derived from the fully relativistic one, has been used. Lee et al. [Lee97] used the techniques of Blomqvist and Laget, based on an effective Lagrangian approach and a diagrammatic method, to calculate the various Born amplitudes and the pion production amplitude via intermediate Δ-resonance excitation [Blo77]. Other differences between the two models include the wave functions of the nucleons in the initial and final states, and the final-state interactions between the pion and the residual nucleus.

So far, experimental studies on Delta excitation in nuclei were mainly performed with charged pions (quasi-free pion scattering and pion absorption) or

contained charged pions in the final state (pion photo- and electroproduction). For example it was demonstrated recently that the partial cross sections $\frac{d^2\sigma_T}{d\Omega_\pi}$, $\frac{d^2\sigma_L}{d\Omega_\pi}$, and $\frac{d^2\sigma_{LT}}{d\Omega_\pi}$, measured for the reaction ^{3}He$(e,e'\pi^+)$, can be described only after a medium modification of the self-energy for the pion and Delta propagator [Blo97, Koh02]. As mentioned above, such reactions contain large contributions from non-resonant interactions. A more dedicated study of the dynamics of the Delta in a nucleus requires measurements on π^0 production by real or virtual photons.

Until now, the π^0 measurements are confined to coherent production, implying the same nuclear initial and final states. In the most advanced study [Bot99] the recoiling ^{4}He nucleus was detected instead of the two photons emitted in the decay of π^0 particle. This largely increases the figure of merit of the experiment.

Experimental studies on quasi-free pion production are scarce and were focused on photoproduction of charged pions. They comprise measurements with real photons of the reactions ^{4}He(γ,π^+p), ^{4}He(γ,π^+n) [Bra02], ^{12}C(γ,π^+n) [MKe96, Bra99], and ^{16}O(γ,π^-p) [Pha92, Ude98].

In the present thesis the reactions ^{4}He$(e,e'p\,^3$H$)\pi^0$ and ^{4}He$(e,e'p\,^3$He$)\pi^-$ are described in the Δ-resonance region. It is the first study in which the $(\gamma^*,p\pi^0)$ and $(\gamma^*,p\pi^-)$ channels were investigated, at the same kinematic conditions. The measurements were performed simultaneously using the Internal Target Facility (ITF) of the Amsterdam Pulse Stretcher (AmPS) at the National Institute for Nuclear Physics and High Energy Physics (NIKHEF) with the following objectives:

- to study pion production in a nuclear medium and the role of the Delta in this process.
- to study the importance of the Born contributions by comparing neutral and charged pion production.
- to address the question if the process can be described as quasi-free mechanism.

The use of these reaction channels has a number of advantages: in the first place the electromagnetic probe is well understood and, as distinct from pion probes, samples the whole nuclear volume. In addition the transferred energy and three-momentum can be varied independently. The ^{4}He nucleus provides a nuclear medium to the intermediate Delta that is comparable to that of heavier nuclei.

Furthermore, because of the limited number of nucleons high precision wave functions are available for the remaining nuclei, ^{3}He and ^{3}H, and, to a lesser extent, ^{4}He. From the experimental point of view, the choice of ^{4}He and the use of an internal target enables recoil detection, i.e. the detection of the recoiling nuclei, ^{3}He and ^{3}H, instead of the (neutral) pions, which is very difficult in electron scattering environments. The fact that the recoiling nuclei ^{3}He and ^{3}H have no excited states simplifies the data analysis.

The kinematics of the $A(e, e'p\pi)A-1$ reaction, the relevant kinematic variables and theoretical models for (quasi-)free pion production are discussed in chapter 2. In chapter 3 the experimental setup is described in detail. The analysis of the data taken with the three detectors, the identification of events corresponding to both reaction channels, and the method applied to extract the pion production cross sections are discussed in chapter 4. Finally in chapter 5 the cross sections are presented as a function of various observables and a comparison is made with the results of calculations using the model of Lee et al. [Lee97]. The last section comprises a summary of this study.

2 Theory

2.1 Kinematics for the reaction $A(e,e'p\pi)A-1$

In quasi-free pion electroproduction, the pion is produced by electron scattering on a nucleon in a nucleus, the residual $A-1$ system being a spectator. In this process the four-momenta of six particles are involved, i.e. the nucleus in the initial state, the incoming and the scattered electron, the emitted proton and pion, and the recoiling nucleus. The incident and scattered electron have four-momenta (E_e, $\mathbf{p}_\mathrm{e}$) and ($E_{\mathrm{e}'}$, $\mathbf{p}_{\mathrm{e}'}$). At the interaction vertex a virtual photon with four-momentum (ω, $\mathbf{q}$), with $\omega = E_\mathrm{e} - E_{\mathrm{e}'}$ and $\mathbf{q} = \mathbf{p}_\mathrm{e} - \mathbf{p}_{\mathrm{e}'}$, is transferred to the nucleon (natural units $\hbar = 1$ and $c = 1$ are used). The nuclei in the initial and final state are characterized by the four-momenta (E_A, $\mathbf{p}_\mathrm{A}$), with $\mathbf{p}_\mathrm{A} = 0$, and ($E_{\mathrm{A}-1}$, $\mathbf{p}_{\mathrm{A}-1}$). The emitted pion and proton have four-momenta (E_π, $\mathbf{p}_\pi$) and (E_p, $\mathbf{p}_\mathrm{p}$).

The kinematics for the reaction $A(e,e'p\pi)A-1$, in the present experiment $^4\mathrm{He}(e,e'p\pi^0)^3\mathrm{H}$ and $^4\mathrm{He}(e,e'p\pi^-)^3\mathrm{He}$, is schematically depicted in fig. 2.1. The momenta of the incoming and scattered electron define the scattering plane. Two other planes are defined by $\mathbf{q}$ and $\mathbf{p}_\pi$, and by $\mathbf{q}$ and $\mathbf{p}_\mathrm{p}$. The relative orientations of these planes with respect to the scattering plane are given by the azimuthal angles $\phi_{\pi,\mathrm{q}}$ and $\phi_{\mathrm{p,q}}$, and the polar angles of the pion and proton momenta with respect to $\mathbf{q}$ are $\theta_{\pi,\mathrm{q}}$ and $\theta_{\mathrm{p,q}}$. In section 2.3 it is argued that it may be more appropiate to define the angles with respect to $\mathbf{q'} = \mathbf{q} - \mathbf{p}_{\mathrm{A}-1}$. Then the polar and azimuthal angles for the pion and proton are ($\theta_{\pi,\mathrm{q}'}$, $\phi_{\pi,\mathrm{q}'}$) and ($\theta_{\mathrm{p,q}'}$, $\phi_{\mathrm{p,q}'}$), respectively.

If the energy and momentum of the exchanged photon are known, the final state is completely determined by measuring two out of the three momenta $\mathbf{p}_\mathrm{p}$, $\mathbf{p}_\pi$ and $\mathbf{p}_{\mathrm{A}-1}$. In this experiment the momenta of the emitted proton and the recoiling nucleus are measured. Hence, the missing momentum is

$$\mathbf{p}_\mathrm{m} = \mathbf{q} - \mathbf{p}_{\mathrm{A}-1} - \mathbf{p}_\mathrm{p} = \mathbf{q'} - \mathbf{p}_\mathrm{p} = \mathbf{p}_\pi. \tag{2.1}$$

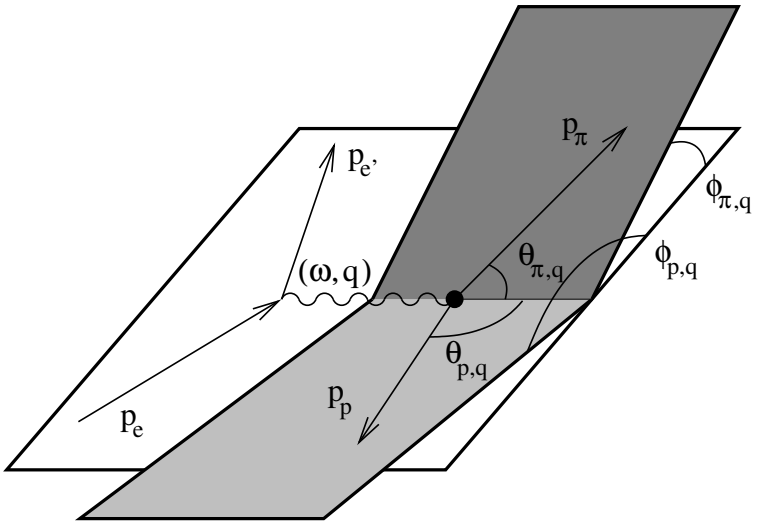

Figure 2.1: *The coordinate system and the momenta of the particles in the reaction* $A(e,e'p\pi)A{-}1$. *The momentum vector of the recoiling nucleus,* $\mathbf{p}_{\mathrm{A}-1}$, *is not shown.*

Furthermore, the missing energy reads as

$$E_{\mathrm{m}} = \omega + E_{\mathrm{A}} - E_{\mathrm{A}-1} - E_{\mathrm{p}} = E_{\pi}, \tag{2.2}$$

or, alternatively as

$$E_{\mathrm{m}} = \omega - S_{\mathrm{p}} - T_{\mathrm{p}} - T_{\mathrm{A}-1}, \tag{2.3}$$

where the proton separation energy S_{p} is equal to $S_{\mathrm{p}} = m_{\mathrm{A}-1} + m_{\mathrm{p}} - m_{\mathrm{A}}$. The quantities T_{p} and $T_{\mathrm{A}-1}$ are the kinetic energies of the emitted proton and the recoiling nucleus. Note that the measured recoiling ^{3}He and ^{3}H nuclei have no excited states. From equations (2.1) and (2.2) one obtains the missing mass

$$M_{\mathrm{m}} = \sqrt{E_{\mathrm{m}}^2 - p_{\mathrm{m}}^2} = m_{\pi}. \tag{2.4}$$

Another useful variable is the invariant mass of the proton-pion system in the final state, defined as

$$W_{\pi\mathrm{N}} = \sqrt{(E_{\mathrm{p}} + E_{\pi})^2 - |\mathbf{p}_{\pi} + \mathbf{p}_{\mathrm{p}}|^2}. \tag{2.5}$$

One can express $W_{\pi\mathrm{N}}$ in terms of ω, $\mathbf{q}$ and the momentum of the recoiling nucleus. Using equations (2.1), (2.2), and (2.5) one obtains:

$$W_{\pi\mathrm{N}} = \sqrt{(\omega + m_\mathrm{p} - S_\mathrm{p} - T_{\mathrm{A}-1})^2 - |\mathbf{q} - \mathbf{p}_{\mathrm{A}-1}|^2}. \tag{2.6}$$

In the proton-pion center-of-momentum system $W_{\pi\mathrm{N}} = \sqrt{(E_\mathrm{p} + E_\pi)^2}$. In the case that these particles originate from the decay of a Delta particle, $W_{\pi\mathrm{N}}$ is equal to m_Δ, the mass of the Delta.

2.2 Pion electroproduction on a nucleon

The amplitude for electroproduction of a pion on a (free) nucleon, $\gamma^* + N \rightarrow \pi + N$, is expressed by the T-matrix [Ama79, Eri88]:

$$T_\mathrm{fi} = \epsilon_\mu J^\mu_\mathrm{fi} = \epsilon_\mu u_\mathrm{f} J^\mu u_\mathrm{i}, \tag{2.7}$$

where u_i and u_f are the Dirac spinors for the nucleons in the initial and final states, ϵ_μ is the polarization vector of the virtual photon and J^μ represents the hadronic current.

The pion production amplitudes are often expressed in multipoles. These multipoles $\mathcal{M}_{l_\pi\pm}$ are classified to their electromagnetic character ($\mathcal{M} = L, E, M$) and the pion angular momentum l_π; the $\pm$ signs refer to the angular momentum coupling of the pion and nucleon in the final state: $J = l_\pi \pm \frac{1}{2}$. At momentum transfers $|\mathbf{q}| \leq 400$ MeV/c the relevant multipoles are L_{0^+}, E_{0^+}, L_{1^+}, E_{1^+}, M_{1^-} and M_{1^+}. Pion production via intermediate Delta excitation is dominated by the M_{1^+} multipole.

Pion production amplitudes can be calculated using an effective Lagrangian approach to describe the nucleon and pion fields and their interaction [Pec69, Ols75]. The resulting hadronic current then reads

$$J_\mu = J^\mathrm{N}_\mu + J^\pi_\mu + J^{\pi\mathrm{N}}_\mu. \tag{2.8}$$

The last term in this relativistic current operator is the pion production current. The coupling of the electromagnetic field to the hadronic currents is introduced by minimal substitution, i.e $\partial_\mu \rightarrow \partial_\mu + ieA_\mu$. A diagrammatic representation of the various ways the photon can couple to the proton and pion fields is shown in fig. 2.2. These diagrams include the Delta terms (e, f) and the Born terms: the Kroll-Ruderman (a), pion-pole (b), and nucleon terms (c, d). These diagrams

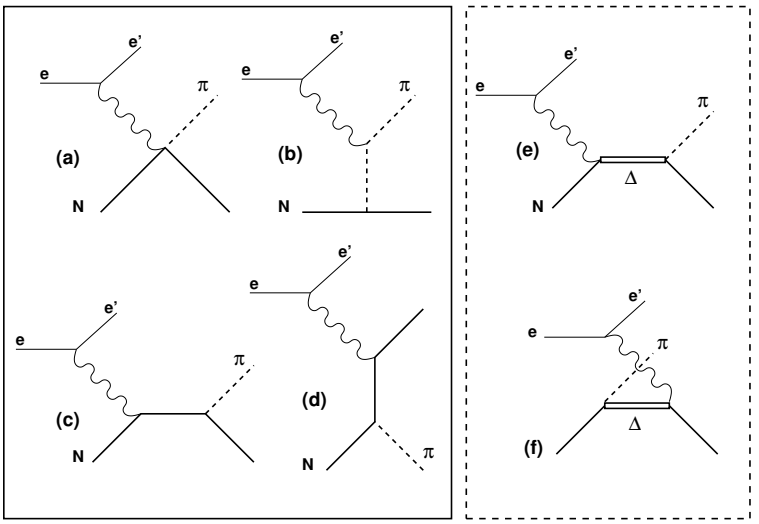

Figure 2.2: *The diagrams that contribute to the pion production cross section in the energy regime up to the Delta excitation region.*

satisfactorily describe pion production in the $W_{\pi N}$ region up to the $\Delta(1232)$ excitation region. For the π^0 reaction channel an ω exchange term is added in order to describe the data.

In the case of π^0 production the diagrams (a) and (b) vanish, because a (virtual) photon cannot couple to a neutral pion. This gives a strong reduction of the contribution of the Born terms to the cross section for π^0 production relative to the contribution of the intermediate Delta excitation, as is illustrated in fig. 2.3, where the total cross sections for π^+ and π^0 photoproduction on a proton are compared. Within the effective Lagrangian approach the cross sections for pion electroproduction have been calculated in fully relativistic models (e.g. [Ols75], [Vdh95a]) and in the non-relativistic approximation of [Blo77]. It appeared that the latter calculations, in which each of the diagrams shown in fig. 2.2 is calculated up to order $(\frac{p^2}{m_N^2})$, reproduce the experimental cross section up to the Δ-resonance satisfactorily.

In the non-relativistic calculations, the transition amplitudes corresponding to the various diagrams are functions of the four-momenta of the virtual photon, the pion and the proton in the final state, multiplied with the appropriate products of the photon polarization vector $\boldsymbol{\epsilon}$ and the Pauli spinors $\boldsymbol{\sigma}$ with the

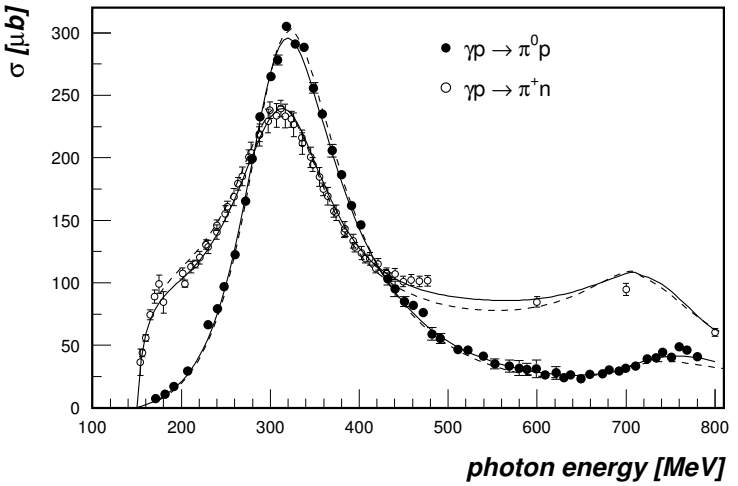

Figure 2.3: *The cross sections for the reactions* $^1\mathrm{H}(\gamma,\pi^+)n$ *(open circles) [Eri88] and* $^1\mathrm{H}(\gamma,\pi^0)p$ *(solid circles) [SAI03]. The solid curves represent the predictions from the SAID program [Arn02] and the dashed curves those from the MAID-DMT model [Kam01].*

unit vectors of $\mathbf{q}$ and $\mathbf{p}_\pi$. These products determine the responses to the longitudinal and transverse polarizations of the virtual-photon field and their interferences. The matrix element that accounts for intermediate Delta excitation reflects the coupling to transversely (M_{1+} and E_{1+}) and longitudinally (L_{1+}) polarized photons. It has a characteristic behaviour due to the Delta propagator $G_\Delta = 1/(W_{\pi\mathrm{N}} - m_\Delta^2 + i m_\Delta \Gamma)$. The mass m_Δ and width Γ of the Delta, and the coupling constants for the $\gamma N\Delta$ and $\pi N\Delta$ vertices are obtained from fits to the δ_{33} phase shift in πN scattering and the measured resonant multipoles.

The cross section for pion production on an unpolarized nucleon with unpolarized electrons can be expressed as a flux factor Γ_v times the cross section for absorption of a virtual photon:

$$\frac{d^5\sigma}{dE_{\mathrm{e}'}d\Omega_{\mathrm{e}'}d\Omega_\pi} = \Gamma_\mathrm{v}\frac{d^2\sigma_v}{d\Omega_\pi}, \tag{2.9}$$

with

$$\frac{d^2\sigma_v}{d\Omega_\pi} = \epsilon\frac{d^2\sigma_\mathrm{L}}{d\Omega_\pi} + \frac{d^2\sigma_\mathrm{T}}{d\Omega_\pi} + \sqrt{\epsilon(1+\epsilon)}\frac{d^2\sigma_\mathrm{LT}}{d\Omega_\pi}\cos\phi_{\pi,\mathrm{q}} + \epsilon\frac{d^2\sigma_\mathrm{TT}}{d\Omega_\pi}\cos 2\phi_{\pi,\mathrm{q}} \tag{2.10}$$

and

$$\Gamma_{\mathrm{v}} = \frac{\alpha}{2\pi^2}\frac{E_{\mathrm{e}'}}{E_{\mathrm{e}}}\frac{(W^2 - m_{\mathrm{A}}^2)/2m_{\mathrm{A}}}{Q^2}\frac{1}{1-\epsilon}. \tag{2.11}$$

In this expression, α is the fine structure constant, W is the invariant mass of the γ^*-nucleus system, in this case equal to $W_{\pi\mathrm{N}}$, and m_{A} is the mass of the target nucleus, in this case equal to the mass of the nucleon. The four cross sections $\frac{d^2\sigma_{\mathrm{L}}}{d\Omega_\pi}$, $\frac{d^2\sigma_{\mathrm{T}}}{d\Omega_\pi}$, $\frac{d^2\sigma_{\mathrm{LT}}}{d\Omega_\pi}$, and $\frac{d^2\sigma_{\mathrm{TT}}}{d\Omega_\pi}$ depend on $W_{\pi\mathrm{N}}$, Q^2, and $\theta_{\pi,\mathrm{q}}$. The variables $\theta_{\pi,\mathrm{q}}$ and $\phi_{\pi,\mathrm{q}}$ have been indicated in fig. 2.1.

2.3 The cross section for quasi-free pion production in a nucleus

In calculations of the cross section for pion electroproduction on a nucleon inside a nucleus, the use of multipoles is not convenient, because they cannot be converted easily to the pion-nucleus center-of-momentum system. Therefore, in this case a production operator based on an effective Lagrangian approach is commonly used to describe the nucleon and pion fields and their interaction. Furthermore, these calculations are generally performed using pion production amplitudes calculated with non-relativistic operators.

The nucleon has a momentum $\mathbf{p}_{\mathrm{N}}$ in the initial state, which introduces additional degrees of freedom, so the five-fold differential cross section becomes an eight-fold differential cross section. This cross section can be written in the form [Lee97]

$$\frac{d^8\sigma}{dE_{\mathrm{e}'}d\Omega_{\mathrm{e}'}dE_\pi d\Omega_\pi d\Omega_{\mathrm{p}}} = \Gamma_{\mathrm{v}}\frac{d^5\sigma_v}{dE_\pi d\Omega_\pi d\Omega_{\mathrm{p}}}, \tag{2.12}$$

with

$$\frac{d^5\sigma_v}{dE_\pi d\Omega_\pi d\Omega_{\mathrm{p}}} = \sigma_v = \epsilon\sigma_{\mathrm{L}} + \sigma_{\mathrm{T}} + \sqrt{\epsilon(1+\epsilon)}\sigma_{\mathrm{LT}} + \epsilon\sigma_{\mathrm{TT}}, \tag{2.13}$$

where the short-hand notations $\sigma_{\rm X} = \frac{d^5\sigma_{\rm X}}{dE_\pi d\Omega_\pi d\Omega_{\rm p}}$ (X=L,T,LT,TT) have been introduced. The cross sections $\sigma_{\rm X}$ now depend on 7 † independent variables. Following Donnelly [Don84], two of them can be taken to be

$$\Phi = (\phi_{\pi,{\rm q}} + \phi_{\rm p,q})/2 \quad \text{and} \tag{2.14}$$

$$\Delta\Phi = \phi_{\pi,{\rm q}} - \phi_{\rm p,q}. \tag{2.15}$$

In terms of these variables $\sigma_{\rm LT}$ and $\sigma_{\rm TT}$ can be written as

$$\sigma_{\rm LT} = \sigma^a_{\rm LT}\cos\Phi \quad + \sigma^b_{\rm LT}\sin\Phi \quad \text{and} \tag{2.16}$$

$$\sigma_{\rm TT} = \sigma^a_{\rm TT}\cos 2\Phi + \sigma^b_{\rm TT}\sin 2\Phi. \tag{2.17}$$

The six cross sections $\sigma_{\rm L}$, $\sigma_{\rm T}$, $\sigma^{a,b}_{\rm LT}$, and $\sigma^{a,b}_{\rm TT}$ now do not depend on Φ, but on 6 variables only. Often ω (E_π), q (Q^2), $p_{\rm A-1}$, $W_{\pi\rm N}$, $\theta_{\pi,\rm q}$ ($\theta_{\pi,\rm q'}$) and $\Delta\Phi$ are taken. Formulas (2.12)–(2.17) represent the most general cross section for an $A(e,e'p\pi)A-1$ reaction.

In quasi-free pion production it is assumed that the virtual photon is absorbed by a single nucleon and that the other nucleons are spectators. In this case single-particle wave functions can be used to calculate the matrix elements for the hadronic current. Analogue to free pion production, the z-axis of the reference coordinate system is defined in the direction of the momentum $\mathbf{q'} = \mathbf{q} - \mathbf{p}_{\rm A-1}$ that is transferred to the nucleon. Furthermore, one can argue that the cross section, apart from a kinematical factor, will not depend on the direction of $\mathbf{p}_{\rm A-1}$ ($= -\mathbf{p}_{\rm N}$), only on its magnitude, and that the dependence on the latter follows the momentum density $\rho(p_{\rm A-1})$. Thus, a suitable ansatz for quasi-free pion production is

$$d^5\sigma_v = \rho(p_{\rm A-1})d^5\sigma_{v1}, \tag{2.18}$$

with $d^5\sigma_{v1}$ depending only on 4 independent variables, $\mathbf{p}_{\rm A-1}$ not being among them. From nuclear many-body calculations it is known that for nucleon momenta $p_N \geq 250$ MeV/c (short-range) nucleon correlations become important. This sets an upper limit on the momentum of the recoiling nucleus when comparing the data with the results of quasi-free calculations. Finally, the pion, as well as the ejected nucleon, interacts with the nucleons of the residual nucleus in the final state. In

† This can easily be understood by realizing that in the most general case the cross section will depend on the 4 variables mentioned in section 2.2 ($W_{\pi\rm N}$, Q^2, $\theta_{\pi,\rm q}$ and $\phi_{\pi,\rm q}$) plus the recoil momentum $\mathbf{p}_{\rm A-1}$.

the distorted-wave impulse approximation (DWIA) this is usually described by an optical model.

Lee writes the cross section for quasi-free pion production as [Lee97]

$$\frac{d^8\sigma}{dE_{e'}d\Omega_{e'}dE_\pi d\Omega_\pi d\Omega_p} = \Gamma_v C(\mathbf{q}, \mathbf{p}_\pi, \mathbf{p}_N, E_{A-1})\Sigma\frac{S_\alpha}{2j+1}|T(s,s',m_s,\alpha)|^2, \quad (2.19)$$

where C is a kinematic factor, S_α is the spectroscopic factor, and $T(s,s',m_s,\alpha)$ is the transition matrix element. The summation is over the electron spins in the initial and final states s and s', the quantum numbers of the bound nucleon $\alpha = (nljm)$ and the spin projection of the outgoing nucleon m_s. The transition matrix element reads as:

$$T(s,s',m_s,\alpha) = \int d^3\mathbf{r}\,\Psi^{(+)}_{m_s}(\mathbf{r},-\mathbf{p}_N)\,\phi^{(+)}_\pi(\mathbf{r},-\mathbf{p}_\pi)\,j_\mu\frac{e}{Q^2}J^\mu e^{i\mathbf{q}\cdot\mathbf{r}}\,\Psi_\alpha(\mathbf{r}). \quad (2.20)$$

In this equation j_μ and J^μ are the lepton and the hadron transition currents, respectively, and Ψ_α, $\Psi^{(+)}_{m_s}$ and $\phi^{(+)}_\pi$ are wave functions for the bound-state nucleon, the outgoing nucleon and the pion, respectively. The expression for the cross section of eq. (2.19) can be cast into the form of equations (2.12)–(2.17) [Lee97]. In the calculations described in refs. [Lee93, Vdh95b] the integration of eq. (2.20) is performed numerically.

2.4 Pions and Deltas in a nuclear medium

The propagation of Deltas and pions in a nuclear medium has been the subject of many theoretical studies. As mentioned in chapter 1, this addresses the role of meson degrees of freedom and the dynamics of a Delta in a nucleus.

The most advanced model that describes medium effects in pion-nuclear scattering and pion photoproduction in a nucleus, is the Δ-hole model [Hir79, Ose79, Koc83, Tak88]. In this microscopic model a coherent sum of Δ-hole states is created by the incident particle, that can be either a pion or a (real or virtual) photon. The development of the initial state to the final state is described by the Δ-hole Green function [Hir79]:

$$G_{\Delta_h} = \frac{1}{D(E-H_\Delta)-\delta W - W_\pi - V_{sp}}. \quad (2.21)$$

In this propagator, medium effects like intermediate coupling of the Δ-hole state to a pion and a nucleon include various contributions. The first term represents

the free Delta propagator evaluated in a nuclear medium at an energy $E - H_\Delta$, with $H_\Delta = T_\Delta + V_\Delta - H_{A-1}$. The three terms account for the kinetic and binding energies of the Delta, and for the 'hole-energy'. They cause a shift of the Δ-resonance energy in a nuclear medium. The term δW represents the Pauli-blocking, i.e., the blocking of the decay of the Delta into occupied nuclear states, and W_π accounts for coupling of the Delta to the nuclear ground state and a pion (intermediate elastic pion scattering). Finally, $V_{\rm sp}$ is a phenomenological complex 'spreading potential', which describes the coupling of the Δ-hole state to more complicated configurations like $\Delta N \rightarrow NN$. In the various versions of the Δ-hole model, different approaches have been used to calculate the ingredients of the Δ-hole propagator [Koc83, Gom95].

The Δ-hole model has been very successful in describing pion-nucleus elastic and inelastic scattering, pion absorption and coherent pion photoproduction in the Δ-resonance region, and would be most appropriate to apply in this study. In a consistent treatment of the medium effects of Deltas and pions in pion photo- and electroproduction, the final state interactions of the pions have to be incorporated into the Δ-hole propagator of eq. (2.21). However, such calculations do not exist for quasi-free pion electroproduction.

In the DWIA calculation of Vanderhaeghen [Vdh95b] medium effects in the Δ-propagator are implemented using the prescription of Gómez Tejedor *et al.* [Gom95], and the interaction of the pions with the residual nucleus in the final state is taken into account, like that for the protons, using an optical potential. At present this model has not yet been applied to pion electroproduction in ^{4}He.

Lee *et al.* [Lee97] use an optical potential to describe the final state interaction of the pions as well as the protons in their DWIA calculations. The bound state single-particle wave functions are described by harmonic-oscillator wave functions. The parameters for the proton and pion optical potentials are deduced from the analysis of pA and πA scattering data, respectively. Unfortunately, medium effects of the intermediate Delta are not explicitly accounted for in these calculations. In fig. 2.4 the effect of the pion and proton distortions on the cross sections calculated with this model is shown. The pion absorption is largest in the Δ-resonance region, while the pion distortions give rise to a slight enhancement of the cross section in the Born region. The reduction in the cross section due to the proton distortions is approximately 25% over the whole range in $W_{\pi \rm N}$.

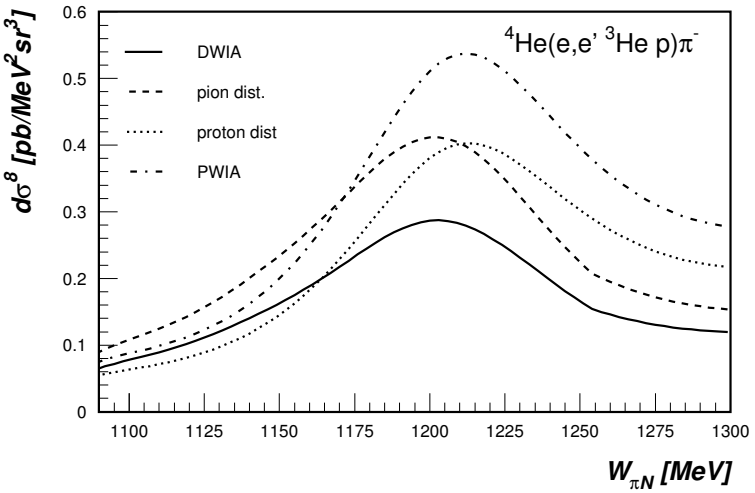

Figure 2.4: *The pion electroproduction cross section for* $^4\mathrm{He}(e,e'p\pi^-)^3\mathrm{He}$*, calculated with the model of Lee as a function of* $W_{\pi\mathrm{N}}$*, while keeping most of the other variables constant at* $p_{\mathrm{A}-1} = 120$ MeV/c*,* $\theta_{\pi,\mathrm{q}'} = 60°$*,* $\phi_{\pi,\mathrm{q}'} = 0°$*,* $\phi_{\mathrm{A}-1,\mathrm{q}} = 0°$ *and* $\theta_{\mathrm{e}'} = 31°$*. The variable* ω *had to vary with* $W_{\pi\mathrm{N}}$ *between 260-520 MeV because of the limited phase space. The calculations including both pion and proton distortions (DWIA), only pion distortions, only proton distortions, and no distortions (PWIA), are indicated by the solid, dashed, dotted, and dashed-dotted curves, respectively.*

2.5 Presentation of the cross section

As discussed in section 2.3, the cross section for quasi-free pion production depends on seven independent observables. The statistical precision of the data does not allow an investigation of the cross section as a function of each of these variables without averaging over some of the others.

Since the aim of this study is to investigate medium effects of pions and Delta particles, employing the properties of the virtual-photon probe, the choice of $W_{\pi\mathrm{N}}$ and Q^2 as variables is a logical one. However, eq. (2.6) shows that these quantities are correlated, if the detection volume does not allow one to vary ω (q) and $\mathbf{p}_{\mathrm{A}-1}$, while keeping Q^2 constant. The correlation between Q^2 and $W_{\pi\mathrm{N}}$ in the detection volume of this experiment is shown in fig. 2.5. In view of the fact that the most

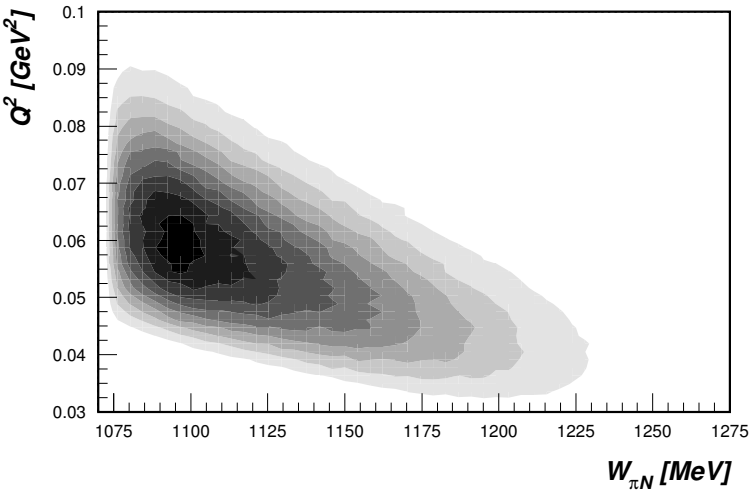

Figure 2.5: *A greyscale plot showing the covered detection volume (kinematic coverage of the experiment) in Q^2 and $W_{\pi\mathrm{N}}$.*

of the dependence of the cross section on Q^2 is contained in the virtual photon flux Γ_v, this dependence is not studied. In addition to $W_{\pi\mathrm{N}}$, as in the case of pion production on a free nucleon, we consider $\theta_{\pi,\mathrm{q}}$ ($\theta_{\pi,\mathrm{q}'}$) as a quantity of interest. The four remaining variables are $p_{\mathrm{A}-1}$, T_π, $\Delta\Phi$ and Φ.

Since the experimental cross section is always integrated (averaged) over parts of the detection volume, the same integration has to be performed for the theoretical cross section in order to be able to compare the two. The expression for the integrated theoretical cross section is (cf. eq. (4.17))

$$\left\langle \frac{d^8\sigma_{th}}{d\mathcal{V}}(\mathbf{X}) \right\rangle = \frac{1}{\int \mathcal{L}dt} \frac{N_{th}(\Delta\mathbf{X})}{V(\Delta\mathbf{X})}, \tag{2.22}$$

where the theoretical yield

$$N_{th}(\Delta\mathbf{X}) = \int \mathcal{L}dt \int \frac{1}{g(\mathbf{v})} \frac{d^8\sigma_{th}}{d\mathcal{V}}(\mathbf{v}) D(\mathbf{X}(\mathbf{v}); \Delta\mathbf{X}) D(\mathbf{w}(\mathbf{v}), z; \mathbf{A}) f(z)\, d\mathbf{v} dz, \tag{2.23}$$

and the detection volume $V(\Delta\mathbf{X})$, $\mathbf{v}$ and $\mathbf{w}$ are given by eq. (4.19) and the text following this equation. For the reaction $^4\mathrm{He}(e,e'p\,A)\pi$ the volume element $d\mathcal{V}$ is equal to e.g. $(dE_{\mathrm{e}'}d\Omega_{\mathrm{e}'}dE_\pi d\Omega_\pi d\Omega_\mathrm{p})$. The normalization function $g(\mathbf{v})$ is introduced to 'remove' certain dependences from the cross section. The assignment

$g(\mathbf{v}) = 1$ results in the 'normal' eight-fold differential cross section $d^8\sigma$. The integrals of equations (2.23) and (4.19) are calculated by doing a Monte Carlo integration in the way illustrated in section 4.7. For both reaction channels the DWIA cross section has been calculated using the program of Lee for $3{\cdot}10^5$ combinations of $\mathbf{v}$ within the detection volume. This calculation took 180 hours on twenty 1-GHz Pentium-III machines.

The dependence of the averaged cross section on the electron variables can be reduced by dividing Γ_v out of the experimental and theoretical cross sections on an event-by-event basis ($g(\mathbf{v}) = \Gamma_v(\mathbf{v})$) using equations (2.11) and (2.12). This leaves us with the five-fold differential cross section $d^5\sigma_v$.

As discussed in section 2.3 the variable p_{A-1} ($=p_{rec}$) has a strong impact on the cross section, because in a quasi-free reaction it is equal to the proton momentum in the initial state. In transitions to ^{3}H and ^{3}He the initial state of the nucleon is a $1s$ state. Hence, the momentum density decreases approximately exponentially with proton momentum. Because of the strong variation of the cross section with p_{rec} in combination with correlations of p_{rec} with other variables within the detection volume, the averaging of the cross section over this observable could introduce false dependences of the cross section as a function of other observables. Therefore, also results are presented in which the dependence on this variable has been largely removed from the experimental as well as the calculated cross sections by dividing each by $\rho(p_{rec})$, the momentum density for a $1s$ state in ^{4}He (in eq. (2.23) $g(\mathbf{v}) = \Gamma_v(\mathbf{v})\rho(p_{rec})$). This momentum density was extracted using a Woods-Saxon potential that describes the $^4\mathrm{He}(e,e'p)^3\mathrm{H}$ data from other experiments [Bra88, Lee96] well (cf. section 5.1). The resulting reduced cross section is referred to as $d^5\sigma_{v1}$.

In a similar way the strong dependence of the cross section on $W_{\pi N}$ affects the presentation of the averaged cross section as a function of θ_π ($\theta_{\pi,q'}$), $\Delta\Phi$ and Φ, because the limited detection volume introduces correlations between these variables and $W_{\pi N}$. Therefore, the reduced cross section has been divided into a $W_{\pi N}$ dependent part $f(W_{\pi N})$ and a non-$W_{\pi N}$ dependent part $d^5\sigma_{v2}$:

$$d^5\sigma_{v1} = f(W_{\pi N}) \times d^5\sigma_{v2}. \tag{2.24}$$

For the function $f(W_{\pi N})$ an empirical function has been taken that describes the $W_{\pi N}$ dependence of the theoretical cross section $d^5\sigma_{v1}$ averaged over the total detection volume. The normalization function is set to $g(\mathbf{v}) = \Gamma_v(\mathbf{v})\rho(p_{rec})f(W_{\pi N})$.

This procedure is illustrated in fig. 2.6. Here the DWIA cross sections $d^8\sigma$,

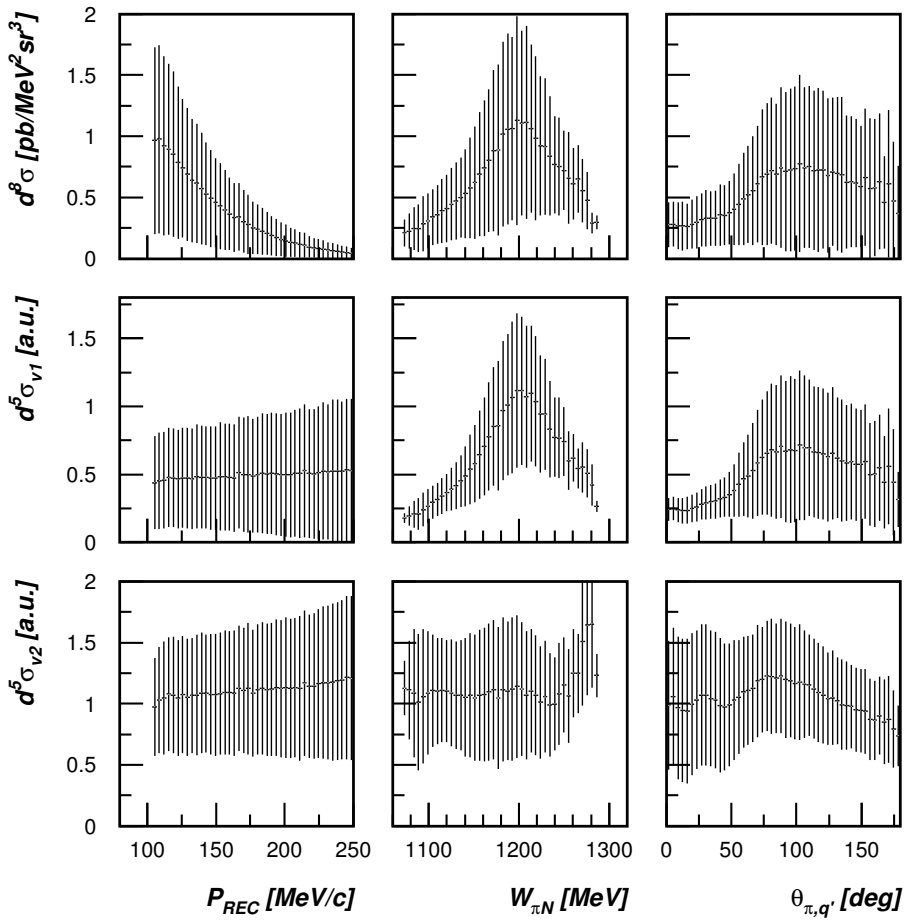

Figure 2.6: *The DWIA cross sections for* $^4\mathrm{He}(e,e'p\,^3\mathrm{He})\pi^-$ *calculated using Lee's model, averaged over the detection volume. From top to bottom the 'total' eight-fold differential cross section* $d^8\sigma$*, the* $(\Gamma_\mathrm{v}\rho(p_\mathrm{rec}))$*-reduced cross section* $d^5\sigma_{v1}$ *and the* $(\Gamma_\mathrm{v}\rho(p_\mathrm{rec})f(W_{\pi\mathrm{N}}))$*-reduced cross section* $d^5\sigma_{v2}$ *are shown as functions of* p_rec*,* $W_{\pi\mathrm{N}}$ *and* $\theta_{\pi,\mathrm{q}'}$ *(left to right). The root mean square of the distribution of the cross sections within the detection volume is indicated by the error bars.*

$d^5\sigma_{v1}$ and $d^5\sigma_{v2}$ for the ^{4}He$(e,e'p\,^3$He$)\pi^-$ reaction channel, calculated using the model of Lee, are presented as functions of $p_{\rm rec}$, $W_{\pi\rm N}$ and $\theta_{\pi,\rm q'}$. For each fixed value of one of these variables the cross section can have various values depending on the wide range of values of the six remaining variables within the detection volume. The average of this distribution of cross sections is shown as a function of $p_{\rm rec}$, $W_{\pi\rm N}$ and $\theta_{\pi,\rm q'}$. The root mean square of this distribution (the 'spread' of the cross section) is indicated by the error bars. It is shown in this figure that the technique of removing the dependence of the cross section on ($\Gamma_{\rm v}$, $p_{\rm rec}$) or ($\Gamma_{\rm v}$, $p_{\rm rec}$, $W_{\pi\rm N}$), clearly reduces the variation of the residual cross section within the detection volume. For example the variations in the DWIA cross section displayed as a function of $\theta_{\pi,\rm q'}$ are reduced from almost 100% ($d^8\sigma$) to less than 40% ($d^5\sigma_{v2}$). For the PWIA calculations (not shown) the reduction is even larger. The method of removing the $W_{\pi\rm N}$ dependence is less successful for ^{4}He$(e,e'p\,^3$H$)\pi^0$ at small values of $W_{\pi\rm N}$. In this region the cross section is almost zero and, therefore, $f(W_{\pi\rm N})$ is very small, giving rise to very high weights for events in this part of the detection volume, which might lead to strange results. Therefore, the second reduction is not applied when comparing the theoretical and experimental cross sections for this reaction channel.

3 Experimental procedure

In this chapter the experimental setup for the quasi-free pion electroproduction experiment on ^{4}He is described. The experiment was carried out at the National Institute for Nuclear Physics and High Energy Physics (NIKHEF) in Amsterdam. Electrons accelerated by the Medium Energy Accelerator (MEA) were stored in the Amsterdam Pulse Stretcher and Storage Ring (AmPS), and scattered off ^{4}He nuclei, as is described in section 3.1. The target consisted of ^{4}He gas flowing through a storage cell in the Internal Target Facility (ITF) experimental hall (section 3.2). The scattered electrons were detected with the BigBite magnetic spectrometer (section 3.3) in coincidence with the protons, detected in the HADRON4 proton detector (section 3.5), and the tritons or the ^{3}He nuclei, detected in the Recoil detector (section 3.4). The data acquisition system is described in section 3.6. The kinematic conditions of the experiment and the performance of the experimental setup are discussed in section 3.7. Unless indicated otherwise all resolutions are expressed in standard deviations σ.

3.1 The Amsterdam Pulse Stretcher and Storage Ring facility

The electron beam for the experiment was provided by the AmPS facility, which consisted of the linear accelerator MEA and the AmPS stretcher/storage ring. With MEA [Vri84] polarized as well as unpolarized electrons could be accelerated up to an energy of 750 MeV, in bursts of 0.7–2.1 μs with a maximum peak current of 30 mA and a repetition rate of up to 150 Hz. The energy spread of the electrons was reduced by means of the Energy Spectrum Compressor to less than 0.1%.
The duty factor of the beam delivered by MEA of less than 0.03% was increased to more than 80% by injecting the electrons into the AmPS ring [Wit93], which is shown in fig. 3.1. This ring had a circumference of 212 m, corresponding to an electron revolution time of 707 ns. The 3-turn injection technique was used to fill the ring with a pulse of a length of three times the circumference of the ring. The AmPS ring had two modes of operation: *storage mode* and *stretcher mode*.

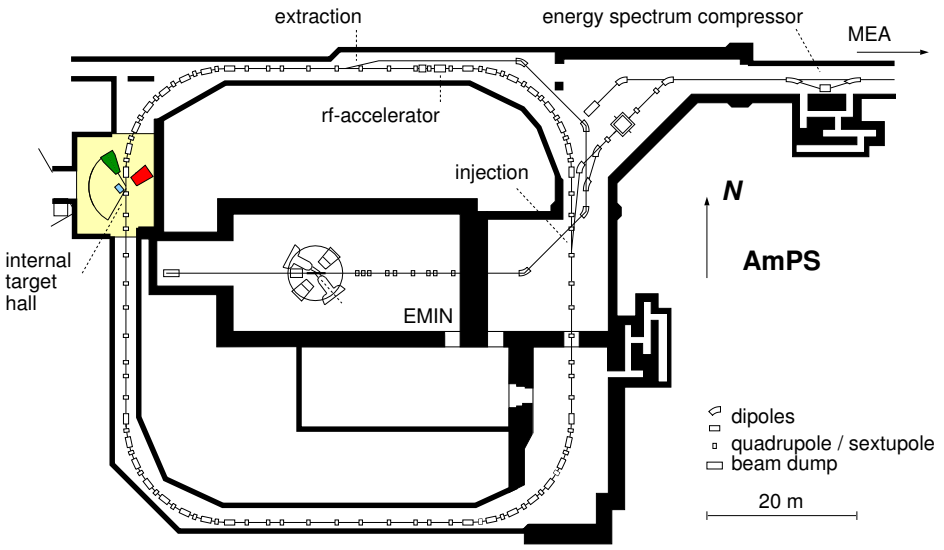

Figure 3.1: *An overview of the AmPS facility. The electrons, accelerated by MEA, which is only partially shown, are stored in the AmPS ring. The experiment was carried out in the Internal Target Hall.*

In the stretcher mode operation the electrons were extracted continuously from the ring and guided to the EMIN experimental hall. In the case of storage mode operation several bunches of electrons were injected and stacked in the AmPS ring, resulting in currents of up to 200 mA. Energy losses due to synchrotron radiation were compensated by a 476 MHz cavity. In this mode the experiments were performed in the Internal Target Hall (ITH) in the west straight of the ring, where a storage cell target was placed in the beam line. In this cell a continuous target-gas flow was maintained. The lifetime of the beam varied typically between 100–1000 s, depending on the phase-space acceptance of the ring (including the storage cell), the ring vacuum, the beam current, the target density and the target-gas species [Bot99]. The background caused by interactions of the beam with the target cell wall as well as the beam lifetime could be optimized by slightly adjusting the beam at the target-cell position, such that it passed through the center of the cell. This so called 'local bump' was obtained with a set of steering coils. Furthermore, the radiation in ITH stemming from the beam halo could be reduced by adjusting two sets of horizontal and vertical slits located in the ring, opposite to the storage cell target. The electron current in the ring was measured

with a Direct-Current-to-Current Transformer (DCCT) with an accuracy of better than 0.1% [Pas96].

3.2 The internal target setup and vacuum system

The ^{4}He gas was contained in a cylindrical storage cell, which is described in detail in ref. [Bot99]. The target cell consists of an open-ended cylinder with a ^{4}He gas inlet in the middle, and is positioned in the vacuum of the scattering chamber.

The aluminum cylinder has a diameter of 15 mm, a length of 40 cm and a wall thickness of 60 μm. In order to minimize the amount of material between the detector and the vertex position, a window of $36\times(0.8\pm0.1)$ cm^2 has been cut out on the side of the Recoil detector (see fig. 3.8). This hole is covered by a 1.0 μm thick mylar foil.

The conductance for the ^{4}He gas flowing from the middle towards the ends of the cell can be considered as the summed conductance of two parallel uniform tubes of half the length of the cell. This conductance, expressed in l/s, is approximated by (see e.g. [Wei79])

$$C_{storage\ cell} = 2 \cdot C_{tube} \approx \frac{\frac{2}{3}\sqrt{\pi}d^3\sqrt{\frac{2kT}{M}}}{L+\frac{8}{3}d} = 15.2 \cdot \frac{d^3}{L+\frac{8}{3}d}\sqrt{\frac{T}{M}}, \qquad (3.1)$$

where d is the diameter in cm, L the cell length in cm, T the gas temperature in K, M the molecular mass in amu, and, where k denotes the Boltzmann constant. The resulting distribution of the gas density in the cell has a triangular shape, giving a total target thickness t in atoms/cm^2 of

$$t = 3.3 \cdot 10^{-5}\frac{NL(L+\frac{8}{3}d)}{d^3}\sqrt{\frac{M}{T}}, \qquad (3.2)$$

where N is the gas flow in atoms/s. The gas flow is controlled by a regulating system, which maintains the ^{4}He pressure in a vessel that is connected to the gas inlet of the target cell through a copper capillary. The gas flow is known with a precision of 5% [Bot99].

Equation (3.2) shows that the target density can be increased without increasing the gas flow (which would consequentially also increase the pressure in the scattering chamber) by cooling the gas. For this reason a cold head was mounted to

the cell wall. The target cell was wrapped with isolating double-sided aluminum coated mylar foils, while a window was left open on the side of the Recoil detector. Gas temperatures as low as 17 K can be obtained in this way [Poo99].

In order to minimize the distortion of the beam, the pressure in the storage ring should be below 10^{-8} mbar. In order to prevent a sizeable fraction of the gas flowing continuously out of the storage cell from entering the storage ring, the following provisions are made in the ITH vacuum system:

1. The scattering chamber is evacuated with a three-stage differential pumping system, consisting of 6 large turbo-molecular pumps with a total pumping speed for ^{4}He of about 10000 l/s.

2. Three conductance limiters are installed both upstream and downstream of the target between the pumping stages to prevent most of the ^{4}He atoms from travelling along the beam line. The diameters of the holes of the conductance limiters increase with the distance from the target and are 20, 25 and 30 mm, respectively.

If the pressure in the scattering chamber exceeds a certain trip level the ITH vacuum is isolated from the ring vacuum by fast switching valves. During the experiment the trip level was set at about 10^{-6} mbar, which allowed a maximum gas flow of about 10^{18} atoms/s. At this flow the ring pressure of 10^{-9} mbar is restored at only a few meters from the internal target.

3.3 The BigBite electron spectrometer

Scattered electrons were detected in the large-acceptance spectrometer BigBite. An extensive description of this spectrometer, which was designed to be used in combination with an extended internal target, can be found in refs. [Lan98a, Lan98b]. BigBite consists of a non-focusing dipole magnet, two multi-wire drift chambers (MWDC), a plastic scintillator and an aerogel Čerenkov detector, as is shown in fig. 3.2.

The H-shaped dipole magnet has a gap of 25 cm and a nominal magnetic field strength of 0.92 T, at which particles with momenta of 500 MeV/c follow the optical axis and are deflected upwards by 25 degrees.

At this field setting the momentum acceptance of the spectrometer is 200–900 MeV/c, which made it possible to study simultaneously elastic electron scat-

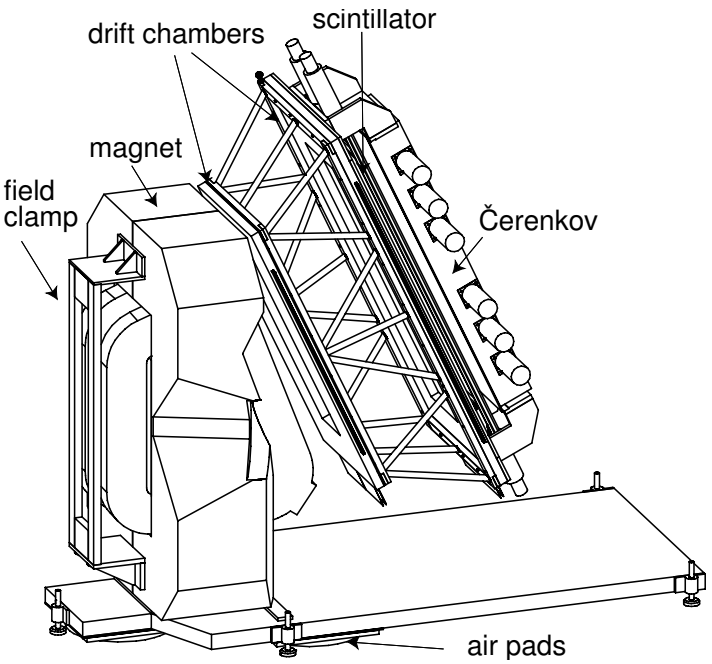

Figure 3.2: *A side view of the BigBite spectrometer. The electrons enter through the magnet from the left and are bent upwards towards the two sets of drift chambers, scintillator and Čerenkov detector.*

tering, quasi-elastic electron scattering and pion electroproduction. The acceptance of BigBite is limited to electrons scattered in the target within a distance of ±10 cm from the symmetry plane of the spectrometer. In this experiment the angle of the spectrometer with respect to the beam line was 30°. Hence, the range z_{target}=±20 cm was covered, where z_{target} is the distance between the scattering vertex and the center of the target along the beam direction. For 500 MeV/c electrons, originating from the center of the target, the detection range is ±80 mrad in the reaction plane and ±300 mrad in the out-of-plane direction, so that the solid angle coverage is 96 msr.

The arrival time of the scattered electrons is determined using signals from the plastic scintillator (dimensions 2000×500×10 mm^3) with an uncertainty of 0.8 ns. The scintillator is read out at each end by two photomultipliers. For a valid hit at least one photomultiplier at each side must have a signal. Discrimination between electrons and pions is achieved using signals from the aerogel Čerenkov

Table 3.1: *BigBite acceptance and resolutions for various quantities.*

BigBite Properties		
	Acceptance	Resolution (σ)
In-plane angle	$\pm$ 80 mrad	3 mrad (600 MeV/c) 8 mrad (200 MeV/c)
Out-of-plane angle	$\pm$ 300 mrad	3 mrad (600 MeV/c) 7 mrad (200 MeV/c)
Momentum	200–900 MeV/c	0.84% ($>$ 400 MeV/c)
Vertex	$\pm$ 10 cm (90°) $\pm$ 20 cm (30°)	3.2 mm (90°) 6.4 mm (30°)
Time		0.8 ns (scintillator)

detector (dimensions 2100×500×240 mm^3, refractive index 1.05). This detector is viewed by 12 photomultiplier tubes, for which the discrimination level was set at 1 photoelectron, while the average number of detected photoelectrons was 4.2. A trigger in BigBite is generated if a coincidence between pulses from the Čerenkov detector and the scintillator is measured.

Both drift chambers consist of two planes with anode wires and two planes with cathode strips, with which the coordinates at two positions in the spectrometer are measured. At least three wire hits and at least two strip hits, one per chamber, are required to determine a track completely.

Matrix elements based on a simple model for the magnetic field, supplemented by corrections based on calibration experiments, are used to reconstruct the momentum vector and vertex position from the determined track. The obtained vertex position resolution is 3.2 mm for a central spectrometer angle of 90° and therefore 6.4 mm at 30°. The acceptance and resolutions for the quantities measured by BigBite are summarized in table 3.1.

As mentioned above the electron trigger is made by a coincidence between the scintillator and the Čerenkov detector. Unless the system is busy processing a previous event, this prompt trigger is transformed into an arm trigger (ATR), which starts the data acquisition modules and is sent to the coincidence detector (see section 3.6). If the coincidence detector returns an event trigger (ETR) the data are read out. The read-out system for the wires has a non-retriggerable dead

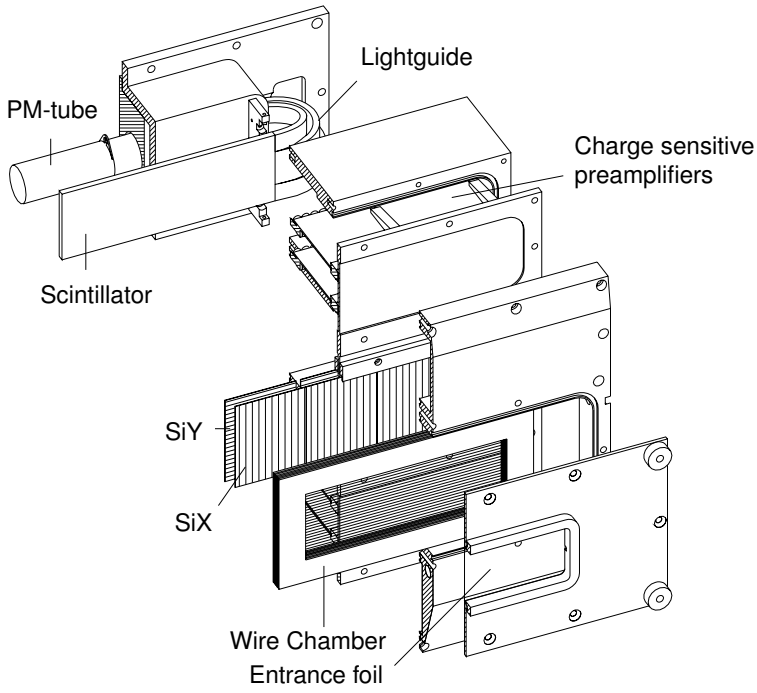

Figure 3.3: *An exploded view of the Recoil detector. Particles enter from the bottom right corner and pass the wire chamber, the two silicon layers (SiX and SiY) and the scintillator.*

time of 1 μs. In order to keep the dead time correction below 8% the counting rate of the wires was held below 80 kHz.

3.4 The Recoil detector

The recoiling nuclei, in our case ^{3}He and ^{3}H, were detected with the Recoil detector, thoroughly described in [Sam99]. This detector, which has been designed for the detection of nuclei with mass numbers $A \leq 4$ and kinetic energies of up to about 50–100 MeV, consists of a low-pressure avalanche chamber, two sets of three segmented Silicon Strip Detectors (SSD), and a plastic scintillator, as is shown in fig. 3.3. The detector box (308×300×150 mm^3) is mounted onto the target chamber. Figure 3.4 shows the specially designed flange on which the Re-

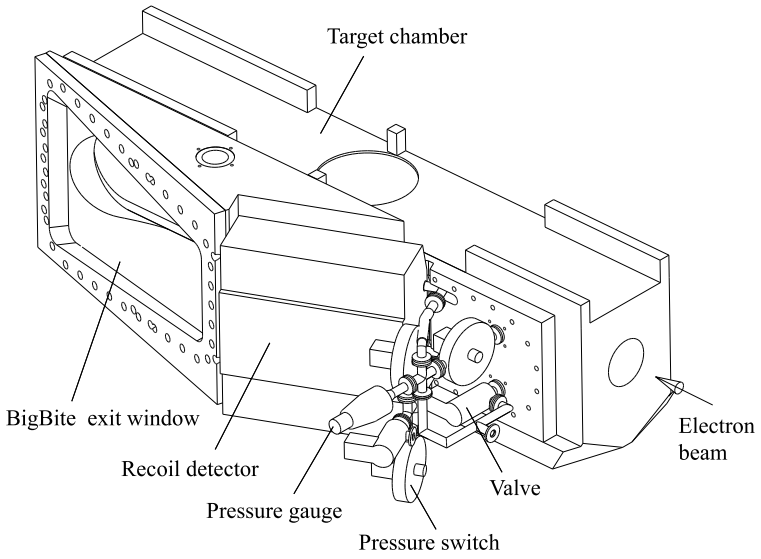

Figure 3.4: *A view of the Recoil detector mounted on the 125° flange. On the left the exit window for the scattered electrons is shown, which is covered by a 55 μm stainless steel exit foil.*

coil detector was mounted in the experiment. The Recoil detector is tilted by 10 degrees in order not to cut into the geometrical acceptance of BigBite. Therefore, the Recoil detector does not face the center of the target; the intersection point of the symmetry plane of the Recoil detector and the target cell is offset by 4.13 cm upstream. The central detector angle is 115° with respect to the direction of the beam and the distance between the intersection point and the first detection layer is 23.28 cm.

In quasi-free pion production the kinetic energy of the recoiling ^{3}H and ^{3}He nuclei is very small. Therefore, the vacuum of the target chamber and the Recoil detector are only separated by a mylar foil with a thickness of 0.9 μm. In this way a detection threshold for ^{3}He nuclei as low as 1 MeV has been achieved. Particles stopping in the second silicon layer (SiY, thickness about 500 μm) or in the scintillator (thickness 5 mm) are identified using the energies deposited in two subsequent detection layers (ΔE-E method). This method is also used to determine the charge of the particles stopped in the first silicon layer (SiX, thickness about 100 μm). The poor energy resolution of the wire chamber (60–

Table 3.2: *Measured physical quantities and the maximum kinetic energies of particles stopping in the Recoil detector elements*

Detector element	Measured quantity	Stopping energy [MeV]				
		^{1}H	^{2}H	^{3}H	^{3}He	^{4}He
Wire chamber	ΔE, t, y	–	–	–	–	–
SiX	ΔE or E, t, x	3.2	4.2	4.9	11	13
SiY	ΔE or E, y	8.8	12	14	31	35
Scintillator	E	24	33	39	83	95

70% FWHM) does not allow the determination of the particle mass. Different isotopes are identified using their time of flight, measured with the avalanche chamber. The x-coordinate (in the reaction plane) of the impact position on the Recoil detector is determined from the strip in the SiX detector that has fired. Depending on the stopping layer, the y-coordinate (out-of-plane coordinate) is determined by either the wire chamber or from the SiY strip that has fired. In table 3.2 the energies at which particles of different types punch through the detector elements, and the quantities measured with each detector element, are listed. For recoiling nuclei originating from the intersection point of the symmetry plane of the Recoil detector and the target cell, the in-plane and out-of-plane angular acceptances are ± 330 mrad and ± 110 mrad, respectively. The total solid angle of the Recoil detector depends on the vertex position, and varies between 38 msr and 133 msr. Taking the triangular distribution of the target density into account the effective solid angle is 97 msr.

In the following subsections some relevant properties of the wire chamber and the silicon detectors are described in more detail. The plastic scintillator was not used in this experiment.

The low-pressure avalanche chamber

The ΔE signals for ^{3}H nuclei up to 4.9 MeV and for ^{3}He nuclei up to 11 MeV kinetic energy are provided by the avalanche chamber. This chamber was operated at a pressure of about 7 mbar of isobutane of 99.95% purity. Before entering the wire chamber the isobutane passes through an oxygen and water filter. The isobutane flow through the entrance foil was $(1.5\pm0.5)\cdot10^{-6}$ mbar l/s at 4.5 mbar.

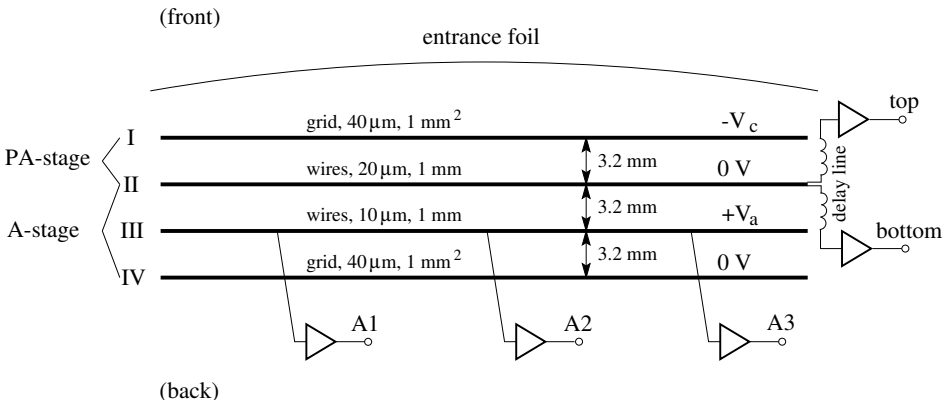

Figure 3.5: *The layout of the two-step avalanche chamber and its readout.*

The ion getter pumps in the ring are not contaminated by this small flux of high Z hydrocarbon molecules. A constant gas flow of 1–5 standard cm^3/min is maintained through the wire chamber by a membrane pump and an Automatic Pressure Controller (APC), which regulates the pressure to within 2% of the set value.

The wire chamber consists of four electrode planes with a total active area of 60×180 mm^2 as is shown in fig. 3.5. Electrodes I and IV are grids of wires with a pitch of 1 mm and 92% transparency. Electrode II consists of wires with 1 mm pitch running in the horizontal direction. The wires of electrode III run in the vertical direction and are grouped in 3 sectors. The amplification in the avalanche chamber comprises two stages, namely a preamplification (PA) stage directly coupled to a amplification (A) stage. The preamplification is realized with electrodes I and II, acting as the cathode and anode, respectively, in a parallel plate avalanche counter. The A-stage operates as a low-pressure multiwire counter, with electrode III as the anode and electrodes II and IV as cathodes.

The electronic signal that is produced by an electronic shower around a wire of plane III is used for timing and energy-loss measurements. The induced signal on the cathode wires of plane II is used for determination of the y-position. The latter wires are connected in pairs to the tabs of a delay-line made of delay-line chips, with delays of 2 ns per tab. From the time difference between both ends of the delay-line the y-position is determined. The signals from the electrodes II and III are digitized in Hadron Digitizer Modules (HDM) [Zwa96].

A permanent magnet with an integrated field of $2.4{\cdot}10^{-3}$ Tm is installed in front of the wire chamber to sweep away most of the Møller electrons. The high impact rates of these electrons cause discharges in this chamber. A reduction of the counting rate by a factor of 50 was measured in an experiment in which the Recoil detector was positioned at an angle of 70° with the beam line [Sam99].

The silicon detectors

Both the SiX and the SiY layer consist of three 50×50 mm^2 SSDs. The distance between the SiX detectors (named SiX1, SiX2 and SiX3) is 10 mm and the SiY detectors (named SiY1, SiY2 and SiY3) are a little further apart. Each SSD has 16 strips at a pitch of 3.14 mm with 50 μm spacing. The strips on the SiX detectors run in the vertical direction, thus giving information on the x-position. The y-position is provided by the SiY detectors, whose strips run in the horizontal direction. The out-of-plane angle resolution is 3–4 mrad and the in-plane angle resolution is 24 mrad. The latter value is completely determined by the resolution of the vertex reconstruction by BigBite of 6.4 mm (section 3.3).

After being shaped and amplified the signals of the individual strips are digitized in Recoil Digitizer Modules [Jan94]. The energy resolutions are 85 keV for SiX and 70 keV for SiY [Sam99].
Furthermore, the output signals of the silicon detectors, summed in groups of eight, are used for timing purposes. The prompt trigger signal is taken from the logic OR of the six timing signals of the SiX detectors, and converted to an ATR signal in the Recoil Trigger Module [Sam99] with a preset dead time of 700 ns. The signals from the SiX detectors were used for the trigger, because all particles of interest at least generate a signal in the SiX layer.

3.5 The HADRON4 detector

The protons were detected with the HADRON4 detector. HADRON4 is one out of a series of HADRON detectors that were designed for proton and pion detection in electron scattering experiments. These detectors have been used in a variety of $(e, e'p)$ and $(e, e'pp)$ experiments performed with a beam extracted from AmPS, see for example refs. [Ond98a, Sta99a, Gro99]. An extensive description of this detector family can be found in [Pel99].

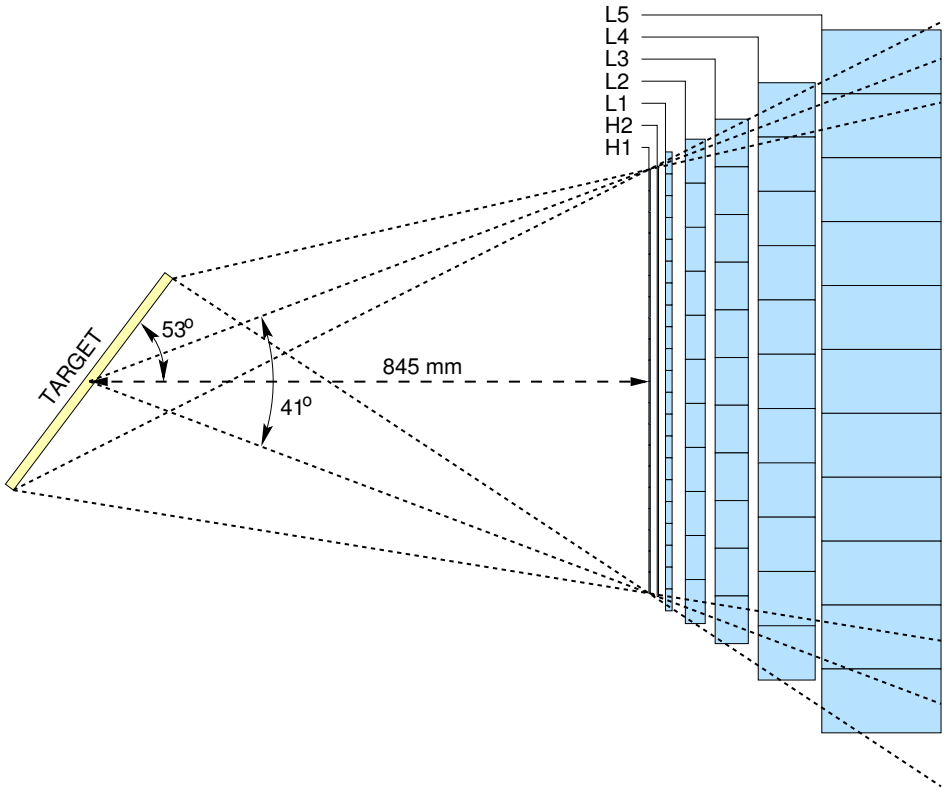

Figure 3.6: *A horizontal cross section of the HADRON4 detector.*

The HADRON4 detector is a segmented plastic scintillator array comprising a hodoscope for the determination of the impact position of the particles and five energy-measuring layers as is shown in fig. 3.6. The high degree of segmentation reduces the counting rate per detector element considerably, which makes the HADRON4 detector well-suited for electron scattering experiments, which are in general plagued by large numbers of low energy electrons. The detector was positioned at an angle of 53° with respect to the beam line; the distance between the front of the hodoscope and the center of the target was about 845 mm.

The geometric specifications of HADRON4 are listed in table 3.3. The hodoscope comprises two layers, H1 and H2, which consist of strips that run in the vertical and horizontal direction, respectively. The five energy determining layers (L1, L2, L3, L4 and L5) are all segmented in the horizontal direction. The

Table 3.3: *Specifications of HADRON4. The in-plane and out-of-plane dimensions are the same for each individual layer.*

Layer	number of elements	number of PMs	width [mm]	thickness [mm]	length [mm]
H1	20	40	32.0	2	640
H2	20	40	32.5	2	650
L1	21	21	33.0	10	698
L2	11	11	66.5	30	737
L3	11	11	72.0	50	797
L4	11	11	82.0	86	905
L5	11	22	96.5	180	1060
total	105	156		360	

thickness of these elements increases with increasing layer number. The elements of L1 are shifted half a pitch with respect to the elements of H1, thus increasing the in-plane angular resolution by about a factor two. For a point-target the out-of plane angular resolution is 11 mrad, while the in-plane resolution is 5.5 mrad. Taking into account the uncertainty in the vertex position, determined by BigBite (section 3.3), the overall in-plane resolution is 8 mrad.

The strips of H1 and H2 are read out by photomultipliers on both sides. This is needed, because the light is strongly attenuated in these thin layers. Each element of the energy determining layers is read out by one photomultiplier except for the elements of L5, which are read out by two 3" photomultipliers, each mounted on the same end. The output signals of these two photomultipliers are summed and fed into one HDM channel. Layer L5 (18 cm thickness) was added to the detector for this experiment to increase the maximum energy for protons stopped in the detector from 165 to 248 MeV.

The scintillator array is housed in a light-tight lead box with an opening in front of the hodoscope. The lead walls on the right and left side have a thickness of 3 cm, whereas the front side is 5 cm thick. Some important HADRON4 parameters are listed in table 3.4.

The counting rates in the hodoscope can be as high as 1 MHz. Since the HDM front-ends have a fixed dead time of 110–140 ns, these counting rates lead to a considerable inefficiency. In order to determine the live time, i.e. the fraction of

Table 3.4: *Summary of the HADRON4 characteristics. The values are specified for a point target.*

solid angle	504 msr
opening angle	41°
in-plane angular resolution (σ)	5.5 mrad
out-of-plane angular resolution (σ)	11 mrad
proton energy range	25–248 MeV
energy resolution (σ) at 100 MeV	1.3%

the time that the front-end electronics is active, electronic test pulses are sent at a fixed frequency to all HDM channels. The live time is obtained by taking the ratio between the number of detected test pulses per front-end channel and the number of generated pulses.

In order to constrain the detector trigger rate, a coincidence between an L1 element and one of the two H1 elements in front of it is required for a trigger. The ATR of HADRON4 is composed of the logic OR between all L1-H1 combinations. The dead time of the trigger system is set at a fixed value of 250 ns. To determine the trigger efficiency the number of arm triggers is compared with the number of prompt triggers, which are provided by the trigger module with a negligible dead time. The trigger efficiency was always above 92%.

3.6 Coincidence detection

The VME-based data acquisition (DAQ) system that was used for the triple coincidence measurements is schematically drawn in fig. 3.7. As soon as a detector arm has received a trigger it stores its data locally and sends an ATR to the Coincidence Detector (CD). For each VME crate of both the HADRON4 arm and the Recoil arm, the readout of the HDMs and RDMs, and the data storage is managed by a Data Acquisition and Readout Transputer (DART) module. This module stores the data in its event fragment memory (EFM) and provides the CD with an ATR label besides the arm trigger signal itself.

The CD measures the arrival times of the arm triggers with a resolution of 48.8 ps and opens a coincidence window of a certain length. The coincidence window for the Recoil arm had a length of 150 ns, while the length was 75 ns

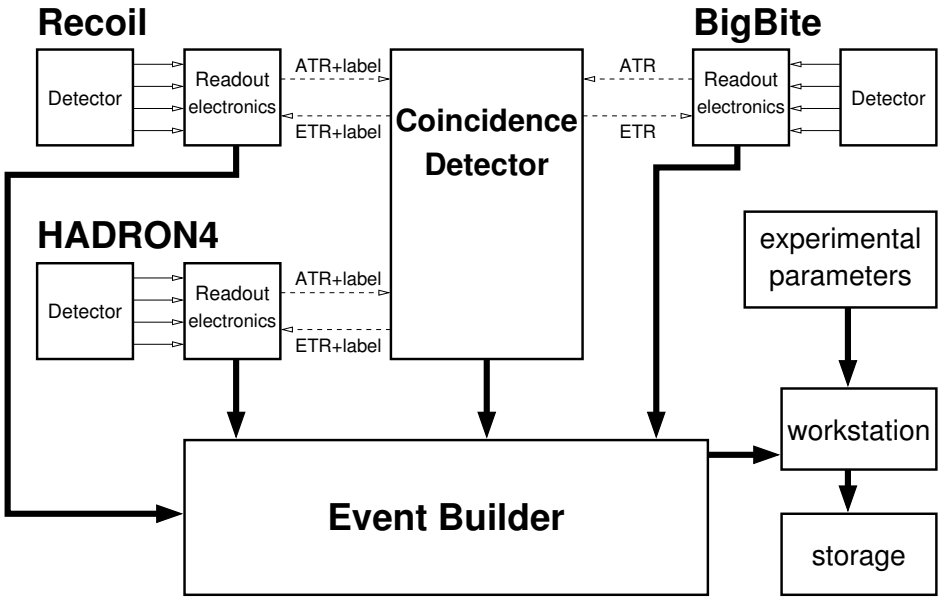

Figure 3.7: *A schematic overview of the data acquisition system. The thick arrows indicate the data flow.*

for HADRON4 and BigBite. Depending on the overlap of the different windows the events are classified as a coincidence type, e.g. single, double or triple coincidence. A prescaler can be set for each coincidence type, so that only a fraction of the events of that type is actually read out, thus reducing the dead time inefficiency in the readout system to about 0.1%. In this experiment the double coincidences were prescaled by a small factor (1–5), while the BigBite, Recoil and HADRON4 singles were most of the time prescaled by factors of 100, 17 and 65535, respectively.

When the CD accepts an event, it sends an ETR to the respective detectors together with the delayed ATR label, and its data consisting of the event fragment identifiers, arrival times and coincidence type information to the event builder (EB). Upon arrival of the ETR (and label) by the detector arm, the temporarily stored data are retrieved from the EFM and sent to the EB. The event fragments are merged into one event descriptor by the EB. The maximum event rate the EB can handle is 5 kHz or 1.4 Mbyte/s. The data communication between the CD, the detector arms and the EB is performed by transputer links.

The data stream from the EB, containing all detector and CD information, is written to disk and tape. Experimental parameters, which are read out on a regular basis during the experiment (e.g. every few minutes), such as the integrated beam current, scaler and prescaler values, are written into parameter blocks, which are merged with the EB output by the DAQ workstation.

3.7 Kinematic conditions and experimental performance

The expected counting rate for quasi-free pion electroproduction is low for experiments performed in ITH. By a proper choice of the experimental conditions the triple coincidence rate was optimized:

- The energy of the incident electrons was chosen as high as possible. The energy limit for stable operation of MEA was approximately 670–700 MeV. A value of 672 MeV was chosen, very close to the one for the coherent pion electroproduction experiment [Bot99], in order to simplify the comparison between the two experiments.

- The experimental yield increases with decreasing scattering angle of the electrons. Therefore, BigBite was positioned at its minimum central angle of 30°. This yields, in combination with the chosen central momentum of 500 MeV/c, a range in ω and q of 250–450 MeV and 350–500 MeV/c, respectively. The value of Q^2 varied between 0.03 and 0.08 GeV^2.

- Since in quasi-free pion electroproduction the emitted proton carries most of the transferred three-momentum, the HADRON4 detector was positioned as close as possible to the direction of the q vector (22° on average). The minimum central angle turned out to be 53°, resulting in a minimum detectable proton angle of 30°.

- The Recoil detector was mounted at an angle of 115° with respect to the beam direction with an upstream offset of 4.13 cm from the target center.

The positions of the detectors are schematically drawn in fig. 3.8.

Performance of the target and the detectors during the experiment

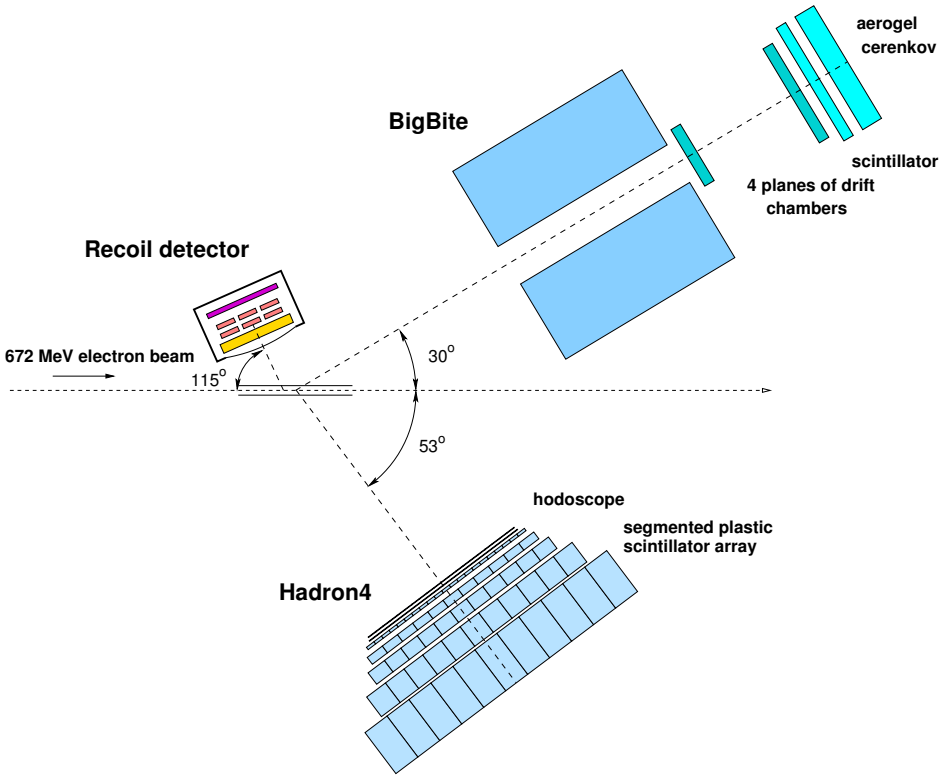

Figure 3.8: *A schematic overview of the setup of the detectors during the experiment.*

Throughout the experiment the target-gas flow was maintained at $2.4{\cdot}10^{17}$ ^{4}He atoms/s. The temperature of the ^{4}He gas was 28 K, as was determined by comparing the sum of the counting rates for elastic and quasi-elastic scattering events in BigBite during the cooling of the cell, while keeping the target flow constant. Figure 3.9 shows that the dependence of the counting rate on the gas temperature, as given by eq. (3.2), is indeed reflected by the data. The gas temperature, deduced from the data, is higher than that reported in ref. [Poo99]. The explanation for this deviation is that the dimensions of the openings in the cell and the insulating mylar foils on the side of the Recoil detector are more than two times larger in the present experiment, which makes the cooling process less efficient. The nominal target thickness, calculated from eq. (3.2), is $1.56{\cdot}10^{15}$ atoms/cm^2. However, the target density, determined independently from elastic scattering measurements

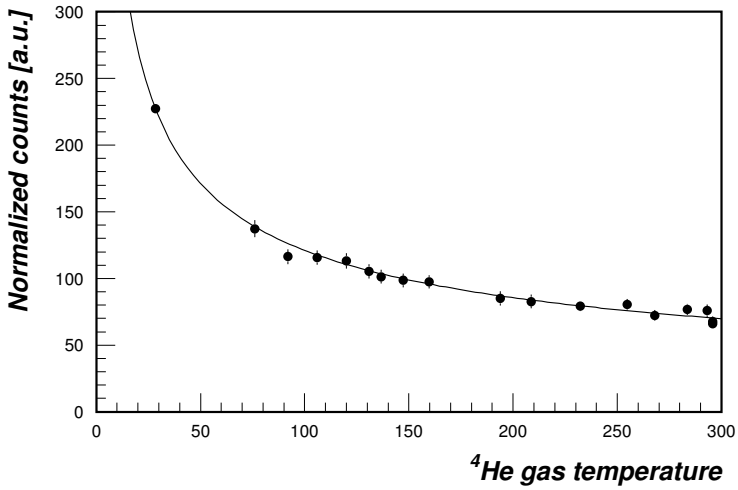

Figure 3.9: *The normalized number of counts from elastic and quasi-elastic scattering versus the measured target-gas temperature, The curve reflects the dependence of the cell conductance on the gas temperature, which is given by eq. (3.1). The gas temperature using the cooled cell was 28 K.*

(see section 4.9), was found to be $5.9{\cdot}10^{14}$ atoms/cm^2 averaged over all measurements and $6.4{\cdot}10^{14}$ atoms/cm^2 for measurements with the cooled target cell. This discrepancy of a factor of 2.4 has already been reported in [Bot99] and was attributed to gas leakage in the lead to the target cell inside the scattering chamber. With the values of the target density and temperature given above, the typical lifetime of the beam was 270 s.

Electrons were stacked in the AmPS ring, resulting in currents of up to 200 mA. The luminosity of a target thickness of $5.9{\cdot}10^{14}$ atoms/cm^2 and an average current of 100 mA was $3.7{\cdot}10^{32}$ cm^{-2}s^{-1}. The integrated beam current during the triple coincidence measurements was 77.3 kC yielding an integrated luminosity of $2.9{\cdot}10^{8}$ μb^{-1}. The reaction ^{4}He$(e,e'p\,^3$H$)$ contributed 99% of the $1.7{\cdot}10^{5}$ triple coincidences. About $0.7{\cdot}10^{3}$ ($1.2{\cdot}10^{3}$) events were collected for the neutral (charged) pion channel.

In addition, measurements were performed with an empty cell and a cell filled with hydrogen. The measurements with the empty cell have been used to estimate the contribution of cell wall events to the recorded number of triple coincidences.

About $2{\cdot}10^5$ coincidences between BigBite and HADRON4 were measured for the ^{1}H$(e,e'p)$ reaction. The reaction ^{1}H$(e,e'p)$ is kinematically complete. Therefore, this reaction provides an excellent tool to check the alignments and energy calibrations of BigBite and HADRON4 as is described in section 4.4.

The detectors of BigBite are only shielded from radiation produced in the target environment by the magnet yoke. During this and previous experiments [Bot99, Lan98, Sam97] it appeared that the drift chambers suffered from high rates of particles, originating from the beam pipe 1–3 meters downstream of the target. Especially the rates in the second drift chamber, which faces this part of the beam pipe directly, exceeded by far the limit of 80 kHz (section 3.3). The background radiation in the detector was largely removed by placing lead sheets on the top and the side of the beam line and by building a lead brick wall between the drift chambers and the beam pipe. Due to this shielding the counting rate in the drift chambers never exceeded 70 kHz.

Despite the efforts to keep the Recoil wire chamber gas as clean as possible and to reduce the Møller electron rates, it was impossible to operate the avalanche chamber at the optimal high voltage. The background radiation in the wire chamber caused discharges and as a consequence the high voltage tripped. After such a discharge the gas volume had to be refreshed completely and we left the high voltage at least 20 minutes off. The high voltages on electrodes I and III were adjusted frequently in the course of the experiment in order to obtain the maximum gain possible. The high voltage for electrode I varied between -385 and -405 Volt, and for electrode III between 390 and 415 Volt, which is on average about 20 Volts below the optimal values. As a result the wire chamber efficiency depended on the energy deposited by the recoiling nuclei in the wire chamber and therefore on the charge, mass and kinetic energy of the particle. This efficiency varied during the experiment and was on average 60% and 90% for ^{3}H and ^{3}He particles, respectively (see section 4.2).

In front of the HADRON4 detector a 1 mm aluminum absorber plate was placed to diminish the flux of low-energy particles stemming from the target. This absorber increased the minimum detection energy by 5 MeV, resulting in a proton kinetic energy (T_p) acceptance of 30–248 MeV. The counting rates in the first hodoscope layer of the HADRON4 detector were as high as 400 kHz/100 mA, resulting in an average live time of 90% for the HDM channels connected to the strips with the highest counting rates. The dependence of the live times on the beam current and how to correct for it is described in section 4.3.

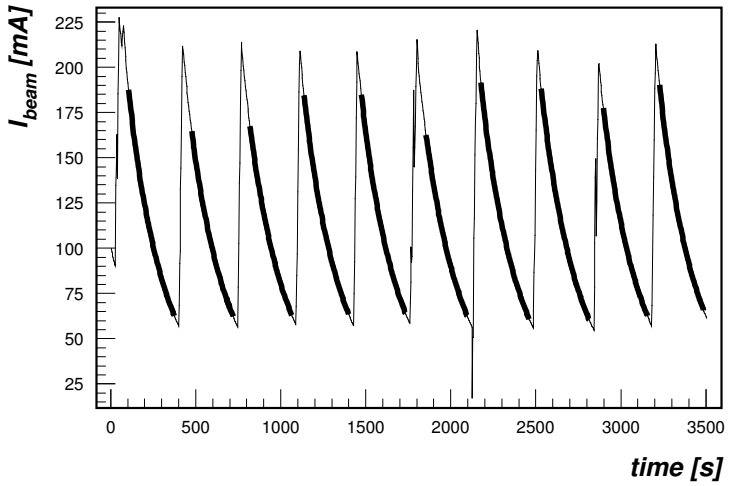

Figure 3.10: *Electron current as a function of time. The thick lines correspond to the period in which the data-taking took place.*

The data-taking procedure

A large part of the data-taking procedure was automated using a set of shell scripts, running on a Sun workstation, that controlled the injection of the beam, the data acquisition system and regulated the ramping of the high voltages.

As an example the time dependence of the beam current is shown in fig. 3.10 in which the data-taking intervals are indicated.

4 Data analysis

This chapter describes the methods that were used in the analysis of the measurements. The analysis of the data taken with the three detectors is described in sections 4.1, 4.2 and 4.3. By combining the momenta measured with the three detector arms, the missing energy and momentum are constructed. These quantities are used to identify the different reaction channels; this is presented in sections 4.4 and 4.5. It is shown in section 4.6 that the contribution of events originating from the target cell wall is negligible. In section 4.7 it is explained how cross sections are extracted from the normalized data, corrected for various inefficiencies, by taking the detection volume into account. The correction to the cross section for radiative processes is described in section 4.8. The determination of the luminosity, which is used for the normalization of the data, is discussed in section 4.9. The chapter concludes with a discussion of the statistical and systematic errors in the determined cross sections (section 4.10).

4.1 Analysis of the BigBite detector data

For the analysis of the BigBite data, the same optical matrix elements were used as in the coherent pion production experiment of Botto [Bot99]. Since the detector package was reinstalled just before the start of the present experiment, the alignment had to be checked. This was done by scattering electrons on two carbon rods of which the position was well known. It appeared that the detector package had shifted by one cm in the direction of the electron beam (see also section 4.4); for this a correction was made in the off-line analysis. Furthermore, elastic scattering data from ^{4}He were used as a check on the energy calibration. The energy of an elastically scattered electron is related to its scattering angle $\theta_{e'}$, the beam energy E_e and the target mass M through

$$E_{e'}^{el} = \frac{E_e}{1 + \frac{2E_e}{M}\sin^2(\theta_{e'}/2)}. \tag{4.1}$$

In fig. 4.1 the difference between $E_{e'}^{BB}$, the energy determined by BigBite, and $E_{e'}^{el}(\theta_{e'}^{BB}, E_e)$ is plotted versus the azimuthal angle $\phi_{e'}^{BB}$. It appears that $E_{e'}^{BB}$ and

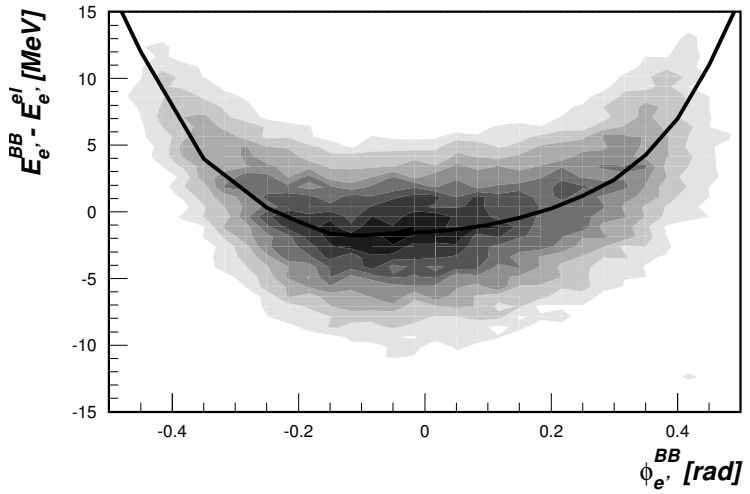

Figure 4.1: *A greyscale plot showing the correlation between* $E^{\mathrm{BB}}_{\mathrm{e}'} - E^{\mathrm{el}}_{\mathrm{e}'}$ *and* $\phi^{\mathrm{BB}}_{\mathrm{e}'}$ *for elastic scattering events. The solid curve represents the correction that is applied to* $E^{\mathrm{BB}}_{\mathrm{e}'}$.

$\phi^{\mathrm{BB}}_{\mathrm{e}'}$ are correlated. This effect is attributed to incorrect BigBite matrix elements for large values of $\phi^{\mathrm{BB}}_{\mathrm{e}'}$, which is accounted for by an ad hoc correction on $E^{\mathrm{BB}}_{\mathrm{e}'}$as indicated in fig. 4.1 by the solid curve. The curve was obtained by taking the mean of a Gaussian distribution fitted to the $E^{\mathrm{BB}}_{\mathrm{e}'} - E^{\mathrm{el}}_{\mathrm{e}'}$ spectra for 20 different values of $\phi^{\mathrm{BB}}_{\mathrm{e}'}$.

In the analysis of BigBite data, the following cuts were applied:

1. The electron comes from the gas in the target cell: $-20 < z_{\mathrm{target}} < 20$ cm.

2. The reconstructed in-plane and out-of-plane angles are within the geometrical acceptance of the detector (see table 3.1).

3. The condition $-0.5 < \phi^{\mathrm{BB}}_{\mathrm{e}'} < 0.5$ rad.

4. The condition $180 < E^{\mathrm{BB}}_{\mathrm{e}'} < 700$ MeV (the upper value is slightly larger than the beam energy).

5. Only events with coordinates $-44 < x < 47$ cm were used, where x is the coordinate in the dispersive direction on the first wire plane. This in order

to avoid trajectories that passed through parts of the fringe field of the magnet, which is largely inhomogeneous.

In the calculation of the detection volume (section 4.7) the same cuts are applied to the scattered electrons. The tracking efficiency ϵ_t is not determined explicitly, since it is contained in the determination of the luminosity (see section 4.9). This tracking efficiency is not expected to vary much as a function of impact position.

In previous analyses of data taken with BigBite [Lan98, Bot99] the (position dependent) efficiency of the Čerenkov detector was an important concern. The number of photoelectrons produced in the Čerenkov detector is distributed according to Poisson statistics and, consequently, there is a finite chance of producing no photoelectron at all. Taking into account the detection threshold of 1 photoelectron, the detection efficiency $\epsilon_{\text{Čerenkov}}$ can be expressed in terms of the average number of detected photoelectrons N_e as [Hig98]

$$\epsilon_{\text{Čerenkov}} = 1 - e^{-N_e}. \tag{4.2}$$

The number of detected photoelectrons was determined as a function of the impact position. In fig. 4.2 the resulting detection efficiency is shown as a function of the dispersive (x) and the non-dispersive (y) coordinate on the Čerenkov detector. It is visible, that the detection efficiency is almost 100% near the 12 photomultipliers, except for the one in the lower right corner, which was broken during the experiment. The efficiency, averaged over the region of the detector that was used ($-105 < x < 75$ cm) in the analysis, was 97%.

4.2 Analysis of the Recoil detector data

The analysis of the Recoil detector data consists of the identification of particles stopping in SiX or SiY, and the determination of their impact position and energy. At the end of this section the detection efficiency is discussed.

Almost all Z=2 (^{3}He) particles of the triple coincidence events were stopped in the first silicon detector, i.e. SiX. Of the Z=1 (^{3}H) particles a fraction of 30%, having the highest energy, was stopped in the second silicon detector, SiY, while the rest was stopped in SiX.

Particle identification of SiX stoppers

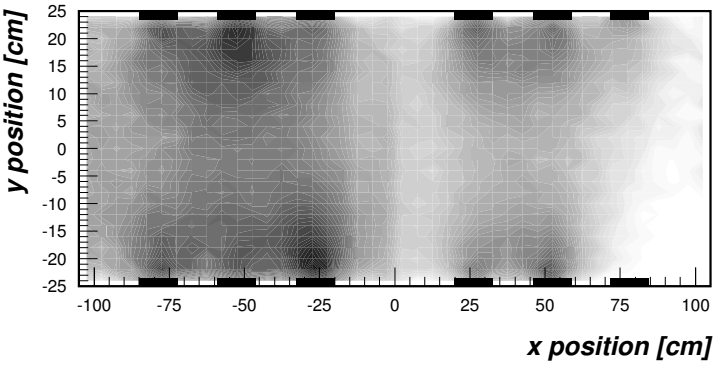

Figure 4.2: *A greyscale plot of the detection efficiency of the Čerenkov detector as a function of the x- and y-position of the impact point. The darkest areas correspond to an efficiency of 100% and the white area to an efficiency of about 89%. The positions of the 12 photomultipliers are indicated by the black rectangles.*

Particles that stop in SiX can be identified in two steps. The charge of the particle is determined with the ΔE-E method by using the wire chamber anode and SiX signals, whereas the different isotopes are resolved by using the time-of-flight method. The charge identification method is illustrated in fig. 4.3. On the left hand side the ADC value of the anode signal, which is proportional to the energy deposited in the wire chamber, is plotted versus the energy deposited in the SiX stopping layer (E_{SiX}). The plot contains ^{1}H, ^{2}H, ^{3}H, ^{3}He and ^{4}He particles. The two bands that can be observed correspond to particles with Z=1 (lower band) and Z=2 (upper band). The energy resolution is not good enough to discriminate between the isotopes of fixed Z. The inset shows the ADC spectrum for particles with $1.0 < E_{\mathrm{SiX}} < 1.5$ MeV, fitted with two Poisson distribution curves. For these particles the charge separation is rather good: the contamination in the Z=1 and Z=2 peaks by the tails of the different charge states is only 3%.

The gain and the collection time of the electrons on the anode depend on the reduced field E/p [Sam99], where E and p are the electric field and the gas pressure in the wire chamber, respectively. Therefore, the frequent adjustments to the operating voltage of the wire chamber that had to be made during the experiment (see section 3.7), gave rise to gain variations as a function of time. The gain was also influenced by fluctuations in the isobutane pressure, caused by

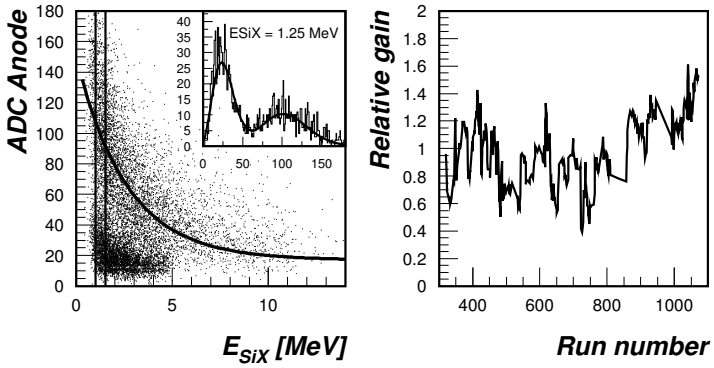

Figure 4.3: *ADC value for the wire chamber anode versus* E_{SiX} *(left). In the inset the separation of particles with different charge is shown for particles with* $1.0 < E_{\mathrm{SiX}} < 1.5$ *MeV. In the plot on the right the variation in the gain is shown as a function of run number (time).*

the APC, which regulated the pressure at the limit of its operating regime. To compensate for these effects, for each run the gain was determined in the off-line analysis by fitting a curve to the Z=2 band (with the gain of the wire chamber as a parameter), as is shown in the left hand panel of fig. 4.3. The fluctuation of the gain as a function of the run number is depicted on the right hand side. The ratio between the maximum and the minimum value of the gain is more than three.

From the ΔE signals the charge of the detected particle was determined by taking out the E_{SiX} dependence for each run. The result is shown in the left panel of fig. 4.4 for all triple coincidence events. The cut used to separate Z=1 and Z=2 particles is indicated by the solid line. Since the dominant reaction channel is $^4\mathrm{He}(e, e'p\,^3\mathrm{H})$, the Z=2 particles (^{3}He) are overwhelmed by the tail of the Z=1 particles. The loss of Z=1 events by setting the 'charge-id' cut is taken into account in the wire chamber efficiency, which is discussed later in this section.

The separation between Z=1 and Z=2 particles for pion production events is pictured on the right in fig. 4.4. The 'charge-id' spectrum is fitted with two Poisson functions, taking into account that the left part of the distribution of the Z=1 particles (about 14%) is cut off by detection thresholds. The separation between the two charge states is set at 'charge-id'=1.35, for which the contribution of Z=2 (Z=1) particles to the Z=1 (Z=2) peak is $10 \pm 5\%$ ($2.6 \pm 0.6\%$).

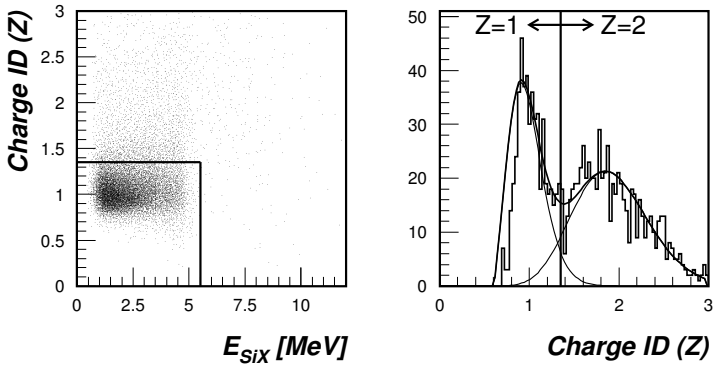

Figure 4.4: *The determined charge versus E_{SiX}, for all triple coincidence events (left). The charge separation for pion production events (right).*

The different isotopes were separated using the time-of-flight method. The time of flight ($T.O.F.$) of the particle in the Recoil detector is defined with respect to the corrected HADRON4 time t_{H4}, rather than with respect to the BigBite time, because of the higher resolution with which the former is known, namely 0.3–0.5 ns (see section 4.3). Thus

$$T.O.F. = t_{\mathrm{WC}} - t_{\mathrm{H4}}. \tag{4.3}$$

The wire chamber time t_{WC} varied during the experiment due to the isobutane pressure fluctuations and different high voltage settings described above. These variations could be characterized, using the abundant singles, by studying the time difference between the SiX hit and the wire chamber anode hit, which should be constant in time. This time difference may be expressed as

$$t_{SiX} - t_{\mathrm{WC}} = TDC_{WC} - \Delta t_{pd}(E_{\mathrm{SiX}}) - \Delta t_{electronics}, \tag{4.4}$$

where $\Delta t_{electronics}$ is the offset in the SiX time that depends on the readout and trigger electronics and Δt_{pd} a correction for the penetration depth of the particle into SiX. The timing of the SiX signal depends on this penetration depth and, therefore, on E_{SiX}. This dependence is shown for Z=2 particles on the left hand side in fig. 4.5. In the same plot a second band can be observed, which originates from events in which the anode signal had a precursor. This effect has not been observed in previous experiments [Sam97, Bot99] and it is not clear where it comes from, although it is most probably caused by the electronics. For about

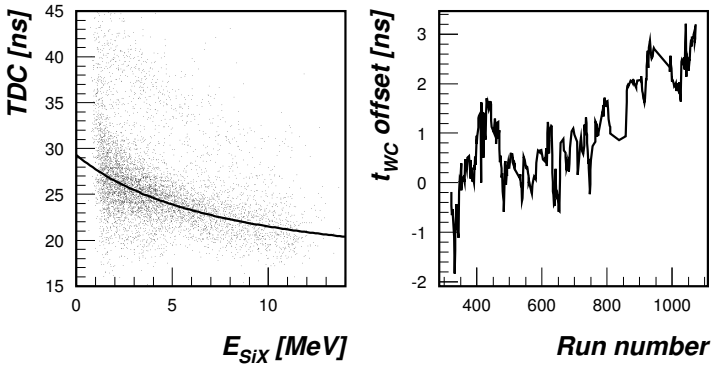

Figure 4.5: *Difference between the trigger time of the SiX detector and that of the avalanche chamber for Z=2 particles, which is related to the penetration depth of the particle (left figure). The fluctuations in* t_{WC} *as a function of run number (right figure).*

5% of the Z=1 events the timing is affected in this way. Having corrected for the penetration depth effect and $\Delta t_{electronics}$ (determined separately for each strip), the fluctuations in t_{WC} could be determined for intervals of 30 seconds. The overall trend as a function of run number is illustrated in fig. 4.5 on the right, each run having a duration of about 1 hour. Note the similarity with the right hand part of fig. 4.3.

The measured time of flight over the approximately 23 cm distance from the vertex to the Recoil detector can be compared with the time of flight that is calculated from the path length and the particle energy. The resulting mass identification is illustrated in fig. 4.6 for particles passing the Z=1 cut. In the left panel the difference between the measured and calculated time of flight is plotted versus the particle energy, assuming the particle has mass number three. The bands for mass one and two are indicated by the curves. From the obtained time-of-flight resolution for tritons of 1.4 ns and the uncertainty in t_{H4}, the intrinsic t_{WC} resolution of 1.3 ns was deduced. Figure 4.6 (right hand panel) shows the mass of the particle, extracted from the time of flight and the kinetic energy. The mass resolution is sufficient to separate the different mass states. In the analysis of ^{4}He$(e,e'p\,^3$H) events, the mass cut, which is indicated in the figure, could be set rather wide, because the yield of deuterons is low. In the analysis of ^{4}He$(e,e'p\,A)\pi$ events the mass cut had to be set to 2300 MeV/c^2, to keep the

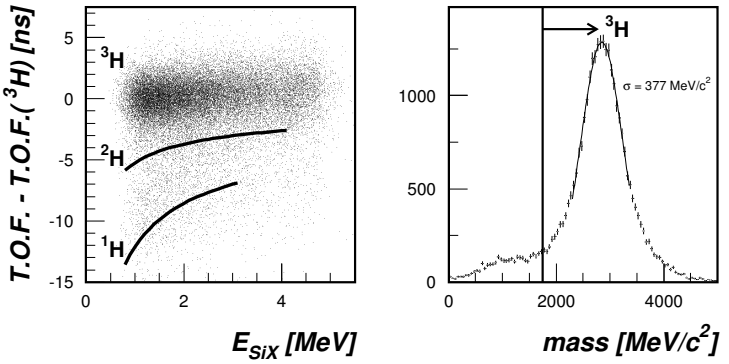

Figure 4.6: *Left panel: the time of flight, relative to the time of flight for tritons versus the energy deposited in SiX for Z=1 particles. Right panel: the resulting mass spectrum for Z=1 particles.*

contribution of deuterons to the triton peak below 5%. The mass three events for which the anode signal had a precursor (fig. 4.5) are largely within the proton peak, and therefore, these events cannot be used in the analysis. This inefficiency is accounted for in the total wire chamber detection efficiency, described later in this section. The analysis of ^{3}He particles could be performed without a cut on the mass, since the number of ^{4}He cell wall events was negligible (see section 4.6).

Particle identification of SiY stoppers

The higher-energy particles that stop in SiY are clearly identified with the ΔE-E method, using SiX and SiY signals, as illustrated on the left hand side in fig. 4.7 for Z=1 particles. The three bands correspond to protons, deuterons and tritons. The difference between the energy deposited in SiX and the energy that can be calculated with the Bethe-Bloch equation from the deposited energy in SiY, assuming a triton, is shown in the right panel. The particle identification cut is set in such a way that no tritons are excluded.

Position determination

The x-position of all particles detected by the Recoil detector is given by the SiX strip number, and the y-position of those reaching SiY by the SiY strip number. For particles stopped in SiX the y-position is (in principle) determined by the time

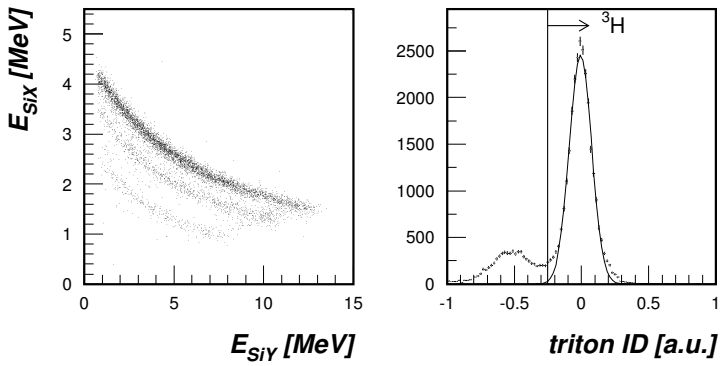

Figure 4.7: *Energy loss in SiX versus energy loss in SiY for Z=1 particles stopping in SiY (left). Triton identification spectrum (right).*

difference between the signals from both ends of the delay-line connected to the cathode. Because of the relatively poor gain (and thus small signal-to-noise ratio) the obtained position resolution was only 1.8 mm for clean events. Furthermore, because of the precursors on both the anode and cathode signals that occurred in more than 20% of the cases, it appeared very hard to determine the correct y-position information in these cases. For these events the y-position was set to zero with an uncertainty of 1.4 cm.

Energy determination

The energy calibration employed in the analysis of [Bot99] was used for the SiX and SiY detectors. This calibration takes energy losses in the non-active layers in the silicon into account.

Efficiency

The detection efficiency of the Recoil detector is mainly determined by the efficiency of the wire chamber. The wire chamber efficiency (ϵ_{WC}) for tritons stopping in SiX could be determined by comparing ^{4}He$(e,e'p\,^3$H) events with and without the wire chamber information. A clean sample of triton events was obtained without using the wire chamber information in the following way:

1. The E_{m} distribution for real ^{4}He$(e,e'p\,^3$H) events peaks around E_{m}=0, whereas for the competing ^{4}He$(e,e'p\,^2$H$)n$ and ^{4}He$(e,e'pp)nn$ reaction chan-

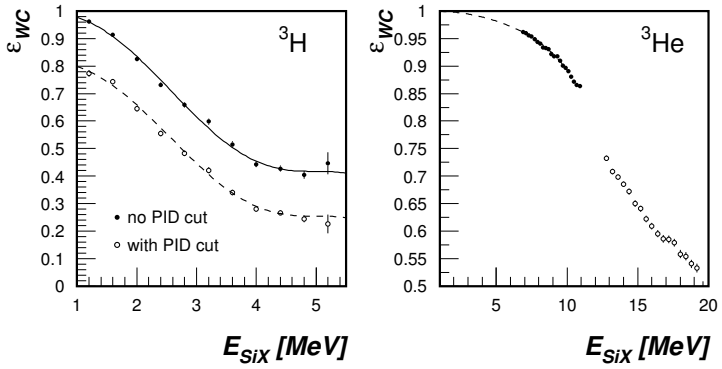

Figure 4.8: *The efficiency of the avalanche chamber for tritons (left) and* ^{3}He *particles (right).*

nels, the $E_{\rm m}$ thresholds are 6.25 MeV and 8.5 MeV, respectively, while their strengths are distributed over a wide $E_{\rm m}$-range. Hence, only events with $-5 < E_{\rm m} < 5$ MeV were used.

2. Assuming a ^{4}He$(e,e'p\,^3$H) event, one can calculate the x-position of the impact point on the SiX detector and compare it with the measured position. For these events the distribution of the difference between the two should be a delta peak. In practice it is a Gaussian distribution with $\sigma = 3$ cm due to resolution effects. For ^{4}He$(e,e'p\,^2$H$)n$ events the distribution still peaks at zero (because the directions of the proton and deuteron are still loosely correlated), but it is much wider, with $\sigma = 8$ cm. For ^{4}He$(e,e'pp)nn$ the distribution is flat. The events used for the determination of $\epsilon_{\rm WC}$ had to be within 3 cm from the calculated x-position.

3. The third reduction of the proton/deuteron contamination in the sample was achieved in a similar way by requiring that the calculated y-position of the impact point is on the SiX detector, which for other than ^{4}He$(e,e'p\,^3$H) events need not be the case.

The contamination with other particles in the final sample is estimated to be smaller than 1%.

The dependence of $\epsilon_{\rm WC}$ on the energy is shown for tritons stopping in SiX in the left panel of fig. 4.8. The fraction of the events that has valid wire chamber

information is given by the filled circles, whereas the open circles represent the fraction of the events that also pass the 'charge-id' and time-of-flight cuts. The reduction of the efficiency is for a large part due to the suppression of precursor signals in the time-of-flight cut. The curves are polynomials of order 5, fitted to the data. The efficiency is correlated with the gain of the wire chamber. It varied in time between 42% and 83%, averaged over all energies. Particles entering the Recoil detector at a non-zero impact angle α traverse a larger part of the wire chamber and are, therefore, detected with a higher efficiency. The measured dependence of ϵ_{WC} on the impact angle was parametrized in the following way:

$$\epsilon_{\mathrm{WC}}(\alpha) = \epsilon_{\mathrm{WC}}(0) \times [1 + \{1 - \epsilon_{\mathrm{WC}}(0)\} \times f(\frac{1}{\cos\alpha} - 1)]. \tag{4.5}$$

Here, f is a polynomial of order five that has a value of zero for $\alpha = 0°$ and 1.3 for $\alpha = 34°$, which is about the maximum detected impact angle. This effect is especially important for low efficiencies (higher energies).

The wire chamber detection efficiency for ^{3}He nuclei was determined using single events. Particles with Z=2 can be selected in two ways without the wire chamber information:

1. By requiring SiX stoppers for which the deposited energy in SiX is higher than the maximum energy for Z=1 particles (about 6 MeV).

2. By selecting ^{3}He particles that stopped in SiY, using the ΔE-E method.

The result is shown in the right panel of fig. 4.8. The open and the filled circles give the efficiencies for SiY and SiX stoppers, respectively. The dashed curve shows the extrapolation that is made towards lower energies, which is where the majority of the interesting triple coincidence events is located. The plotted efficiency is actually the efficiency for a mixture of ^{3}He and ^{4}He particles, but the efficiencies for these particles are almost equal. Of the detected Z=2 particles 88% pass the 'charge-id' cut as is shown in the right panel of fig. 4.4. The impact angle correction is not applied to ϵ_{WC} for ^{3}He particles, since it is very small for these high efficiencies and the impact angle is not known for singles.

Influence of wire chamber grids

The total transparency of the four electrodes of the wire chamber is 82.4% at normal incidence. This means that at least 17.6% of the particles interact with the iron and tungsten wires of the avalanche chamber. Depending on its kinetic

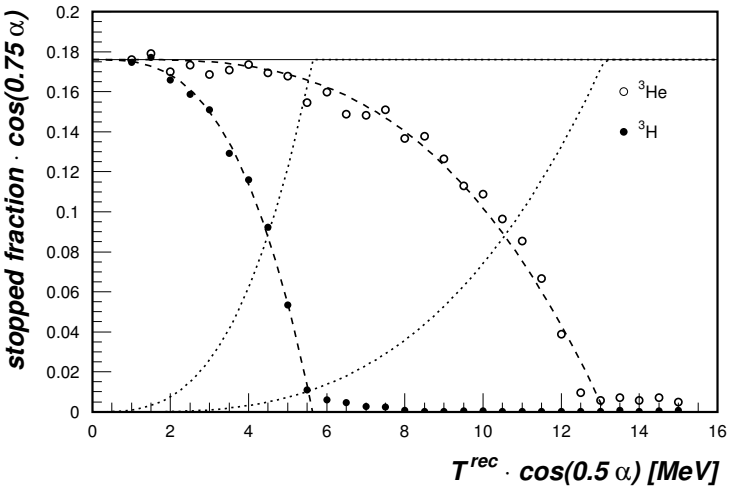

Figure 4.9: *The result of the* `GEANT` *simulation of the effect of the wires of the Recoil avalanche chamber for* ^{3}H *and* ^{3}He *particles. The fraction of the events that is stopped is plotted versus the incident energy. The dotted curves give the fraction of the events that loses energy in the wires without being stopped.*

energy, angle of incidence, charge and mass, a particle either is stopped or loses part of its energy. This effect was simulated using the detector description and simulation tool `GEANT` [Gea93] and is visualized in fig. 4.9. In this figure the fraction of events that is stopped in the wires, is plotted as a function of the kinetic energy of the incident particles. The dependence of the 'stopped fraction' on the impact angle α is eliminated by multiplying the 'stopped fraction' and the kinetic energy of the recoiling particle with the cosine functions as indicated along the axes. In practice α ranges from 0° to 34°. The dashed curves are polynomials of the third degree, fitted to the simulated data. The dotted curves give the fraction of the events that loses energy in the wires without being stopped.

The particles that are stopped in the wires are lost. In the analysis an energy- and α-dependent correction factor accounts for this effect.

For events in which the recoiling nucleus loses energy in the wires, $p_{\rm rec}$ is reduced and as a consequence $\mathbf{p}_{\rm m}$ changes in a direction opposite to the momentum of the recoiling nucleus. For ^{4}He$(e,e'p\,^3$H$)\pi^0$ events this effect broadens the miss-

ing momentum and missing mass distribution; nevertheless 90% of these events still pass the pion identification cuts discussed in section 4.5. The effect is of less importance for the ^{4}He$(e,e'p\,^3$He$)\pi^-$ analysis, since 95% of the ^{3}He particles have an energy lower than 8 MeV and fig. 4.9 shows that even for $\alpha = 0°$ those ^{3}He particles that hit a wire are almost always stopped, and hence are corrected for by the factor mentioned above. In the analysis of the ^{4}He$(e,e'p\,^3$H$)$ events, 2% is lost because $\mathbf{p}_\mathrm{m}$ shifts to the region beyond the boundaries of the ^{4}He$(e,e'p\,^3$H$)$ selection region (as e.g. indicated in fig. 4.15A).

The effect of the particles that lose energy, but are not stopped, is accounted for by a p_rec-dependent correction factor, obtained in the following way: the measured p_rec spectrum (corrected for all other efficiencies) is folded with the detector response. The shape of this detector response depends on the energy of the particle before it interacts with the wires. By taking the ratio between the measured and the folded p_rec distribution the correction factor is obtained.

4.3 Analysis of the HADRON4 detector data

Momentum determination and particle identification

The proton momenta were determined following the same procedure as described in ref. [Pel99]. In the first step the response of each scintillator channel is determined by comparing the ADC values of two subsequent layers that the proton traversed with the amount of light calculated with the Bethe-Bloch equation, using the parametrization by Wright [Wri53] for the conversion of energy to light. These calculations are performed with the program `PLOP`. The light attenuation in the scintillators is accounted for by fitting the 'gain'-dependence on the distance between the intersection point and the photocathode. For each of the L1 elements, all combinations of scintillators that can be part of a track of a particle originating from the target and passing through that L1 element, are stored in a 'candidate array'. In the analysis only tracks within this candidate array are used. The candidate array was extended to incorporate possible tracks originating from interaction points along the beam direction in the range z_target=±20 cm. Furthermore, an extra energy-measuring layer L5 was added to the candidate array. In the left part of fig. 4.10 the light produced in the layers L1 and L2, normalized to the light produced by protons with an impact angle of zero, is plotted. The bands correspond to protons and deuterons. The window, within

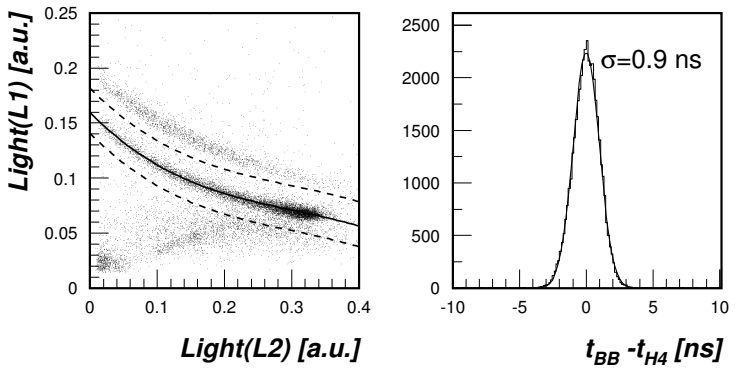

Figure 4.10: *Left panel: plot of the produced light in L1 versus the produced light in L2, revealing the proton and deuteron band. The particle identification window is indicated by the dashed lines. Right panel: the corrected relative timing between HADRON4 and BigBite.*

which the particles are assumed to be protons, is indicated by the dashed lines. Once all scintillator elements are calibrated, one can determine the kinetic energy of the detected protons by comparing the total amount of energy deposited in the detector with the value predicted by `PLOP`. It has turned out, however, that the kinetic energy can be deduced equally well from the amount of light produced in the layer in which the proton is stopped [Pel99]. The latter method has been applied.

Timing

The departure time of the protons from the target is calculated from the clock time of the ATR signal of HADRON4 according to the following expression:

$$t_{\mathrm{H4}} = t_{\mathrm{ATR}} - t_{T.O.F.}(T_{\mathrm{p}}, z_{\mathrm{target}}) - t_{\mathrm{walk}}(\mathrm{ADC}) - t_{\mathrm{prop}}(i_{\mathrm{H2}}) - t_{\mathrm{off}}(i_{\mathrm{L1}}). \quad (4.6)$$

This value is corrected for the phase differences between the L1 subtriggers (t_{off}). Furthermore, corrections are made for the time of flight of the proton ($t_{T.O.F.}$), for the differences in the distance between the photomultiplier and the impact position, determined by the H2 element i_{H2} that is hit (t_{prop}), and the electronic walk (t_{walk}). These corrections were determined iteratively with respect to the 'corrected BigBite time'. The total correction varies between 4 and 18 ns, mainly

determined by the time-of-flight correction (4–15 ns). The final result is shown in the right panel of fig. 4.10. The timing resolution of 0.9 ns is dominated by the resolution of BigBite of 0.8 ns, leaving an intrinsic timing resolution of 0.3 – 0.5 ns for HADRON4, which is comparable to the resolution reported in ref. [Pel99] of 0.3 ns. The spreading in the timing signals due to the BigBite spectrometer with respect to the HADRON4 detector was as large as 5 ns.

Front-end efficiency

The digitizer modules of the HADRON4 detector have a fixed dead time Δt in the range 110–140 ns. This dead time causes an inefficiency in the data handling, which depends on particle rates in the scintillator channels. The resulting 'live time' ϵ_{fe} of the front-end electronics of a scintillator can be expressed as [Leo94]

$$\epsilon_{\mathrm{fe}}(t) = \frac{m(t)}{n(t)} = 1 - m(t)\Delta t = \frac{1}{1 + n(t)\Delta t}, \tag{4.7}$$

where $n(t)$ is the 'hit rate', which is defined as the rate of incident particles in a scintillator that generate a signal large enough to pass the discriminator threshold in the digitizer module, and $m(t)$ is the rate that is accepted by the front-end electronics. As mentioned in section 3.5, the live time of the front-end electronics was determined during the run using test pulses. If the rate of incident particles does not vary strongly, one can write

$$\int_0^T m(t)\,dt \approx \overline{\epsilon_{\mathrm{fe}}} \int_0^T n(t)\,dt, \tag{4.8}$$

with

$$\overline{\epsilon_{\mathrm{fe}}} = \frac{1}{T}\int_0^T \epsilon_{\mathrm{fe}}(t)\,dt = \frac{M_{tp}}{N_{tp}}, \tag{4.9}$$

where N_{tp} is the number of test pulses fed into a digitizer module, M_{tp} the number of accepted test pulses, and T the duration of a measurement.

In this experiment the stored beam of AmPS was used, implying large and strongly varying rates of incident particles. Therefore, one cannot apply eq. (4.8) and the time dependence of $n(t)$ and $m(t)$ has to be taken into account. If $m(t)$ could be extracted from the recorded data, $\epsilon_{\mathrm{fe}}(t)$ could be calculated from eq. (4.7). However, it appeared impossible to extract $m(t)$ from the data and

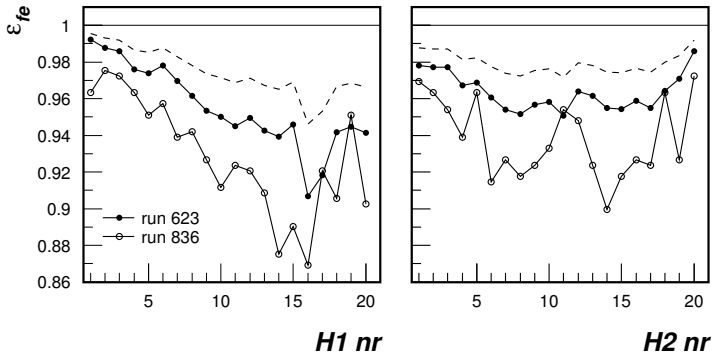

Figure 4.11: *The corrected front-end efficiencies $\widetilde{\epsilon_{\mathrm{fe}}}$ for H1 (left) and H2 (right) for two runs with different beam conditions (solid lines). At least one hit per element is required. For run 623 $\overline{\epsilon_{\mathrm{fe}}}$ is shown by the dashed line.*

therefore the assumption was made that $n(t)$ scales linearly with the beam current which decays exponentially with lifetime τ:

$$n(t) = n(0)e^{-t/\tau} \text{ and thus } m(t) = \frac{n(0)e^{-t/\tau}}{1 + n(0)e^{-t/\tau}\Delta t} \tag{4.10}$$

and

$$\epsilon_{\mathrm{fe}}(t) = \frac{1}{1 + n(0)\Delta t e^{-t/\tau}}. \tag{4.11}$$

The corrected live time $\widetilde{\epsilon_{\mathrm{fe}}} = \frac{\int m(t)}{\int n(t)}$ can be expressed in terms of T, τ, Δt and $\overline{\epsilon_{\mathrm{fe}}}$ by integrating eqs. (4.10) and (4.11) and using eq. (4.9). The quantities T, τ and $\overline{\epsilon_{\mathrm{fe}}}$ were determined for each injection.

Figure 4.11 shows $\widetilde{\epsilon_{\mathrm{fe}}}$ as a function of the hodoscope strip number for two runs with different beam conditions (solid lines). The difference between the distributions can be considered as an indication for the fluctuations in ϵ_{fe} during the measurements. The dashed line gives $\overline{\epsilon_{\mathrm{fe}}}$ for run number 623. For this run the correction is about two percent per strip. The efficiencies of the front-ends of the energy-determining layers are almost 100%. Since the strips of H1 and H2 are oriented perpendicular to each other, their front-end efficiencies are hardly correlated; therefore, the total track efficiency is obtained to good approximation by multiplying the front-end efficiencies of all involved strips. Averaged over all

runs the measured live time for a track is $89.7 \pm 0.7\%$. After correction for the time dependence of the beam current this value is $88.7 \pm 0.7\%$. This indicates that the time-structure of the beam current in the various runs didn't have a large effect on the track live time.

Reconstruction efficiency

In order to simplify the HADRON4 analysis, events in which more than one H1 or L1 element were hit were discarded. The resulting 'single-hit' efficiency was 97.5%. In the analysis of the data the energy loss and absorption of protons in the shielding and scintillator material due to hadronic interactions have to be taken into account. The energy loss may cause an underestimation of the kinetic energy of the protons, which might lead to a misidentification of the particle. Furthermore, the proton may be deflected due to multiple scattering processes in such a way that it leaves the detector before being stopped. As a consequence the particle is not identified as a proton.

The effect of these processes was simulated using the `GEANT` package [Gea93]. The detector geometry, including the new layer L5, the detector shielding and the target cell geometry, were implemented. Protons were generated with a uniform energy and angular distribution covering slightly more than the geometrical and energy acceptance. The light output in all scintillators was simulated and converted to ADC values, using the parameters of the gain calibration for the data. The simulated data were analysed with the same program as the real HADRON4 data. The reconstruction efficiency ϵ_{rec} is defined as the ratio between the number of reconstructed protons and the number of generated protons. This efficiency depends on z_{target}, T_{p}, i_{H2} and H1-L1 combination. For $z_{\mathrm{target}} = -20$, 0, and 20 cm, ϵ_{rec} was calculated as a function of T_{p} and H1-L1 combination and stored in a look-up table. For other values of z_{target} an interpolation was made. In fig. 4.12 ϵ_{rec} is plotted as a function of T_{p} and the H1-L1 combination for $z_{\mathrm{target}} = 0$ cm. It appeared that hardly any proton is lost in the target cell and shielding material. The efficiency gradually decreases with increasing T_{p} and is almost independent of the H1-L1 combination. At the edges of the geometrical acceptance the efficiency distribution reveals large gaps, because these particles leave the detector or the candidate array before they are stopped and, therefore, are not identified as protons. The dependence on i_{H2} was implemented in the following way:

$$\epsilon_{rec}(i_{\mathrm{H2}}) = \epsilon_{\mathrm{rec}}(i_{\mathrm{H2}} = 10.5) - (1 - \epsilon_{\mathrm{rec}}(i_{\mathrm{H2}} = 10.5)) \cdot f(i_{\mathrm{H2}}), \tag{4.12}$$

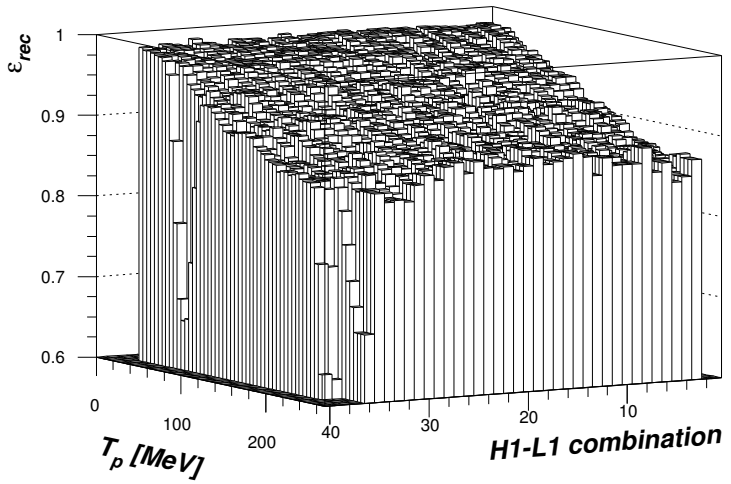

Figure 4.12: *The reconstruction efficiency as a function of H1-L1 combination and* $T_{\rm p}$ *for* $z_{\rm target}$*=0 cm. An interpolation is made for* $z_{\rm target}$ *and the* $i_{\rm H2}$ *dependence is parametrized.*

where f is a second-order polynomial. The correction varies between 0 and 5%.

4.4 Alignment and energy-calibration checks

By exploiting the kinematically completeness of the measured reaction channels ^{4}He$(e,e'\,^4$He$)$, ^{1}H$(e,e'p)$ and ^{4}He$(e,e'p\,^3$H$)$, the alignment and energy calibration of the different detectors could be checked. For these reaction channels $E_{\rm m}$ and the three components of $\mathbf{p}_{\rm m}$ should be zero, where $E_{\rm m}$ and $\mathbf{p}_{\rm m}$ are defined as

$$E_{\rm m} = m_{\rm A} + \omega - \sum_i (m_i + T_i) \tag{4.13}$$

and

$$\mathbf{p}_{\rm m} = \mathbf{q} - \sum_i \mathbf{P}_i,\ p_{\rm m} = |\mathbf{p}_{\rm m}|. \tag{4.14}$$

In these equations T_i, $\mathbf{P}_i$ and m_i are the kinetic energy, three-momentum vector and mass, respectively, of detected particle i and $m_{\rm A}$ is the mass of the nucleus.

Furthermore, in the case of elastic scattering, the angle θ_A of the recoiling nucleus can be expressed in terms of its kinetic energy T_A as follows:

$$\tan\theta_A = \frac{1}{1+E_e/m_A} \times \sqrt{\frac{2E_e}{m_A T_A}(E_e - T_A) - 1}. \tag{4.15}$$

Using the impact position on the detector of the detected nucleus and the value for θ_A from eq. (4.15) one can determine z_{calc}, the vertex position along the target cell. The thus calculated value can be compared to the value of z_{target} as determined from BigBite. Furthermore, the relationship

$$\theta_{e'}^{el} = \arcsin\sqrt{\frac{m_A T_A}{2E_e(E_e - T_A)}} \tag{4.16}$$

is used to check $\theta_{e'}^{BB}$, as an alternative for eq. (4.1), which relates the angle ($\theta_{e'}$) and energy ($E_{e'}$) of the scattered electron to the beam energy E_e.

Elastic scattering: ^{4}He$(e,e'\,^4$He) and ^{1}H$(e,e'p)$

The ^{4}He$(e,e'\,^4$He) coincidences between BigBite and Recoil were measured before the start of the pion production experiment. For this purpose the Recoil detector was mounted on another flange at a central angle of 70° with the beam line. The beam energy for these measurements was 600 MeV.

To perform the ^{1}H$(e,e'p)$ measurements the pion production experiment was interrupted about halfway the data-taking period. The beam energy and the tuning of the storage ring as well as the positions of BigBite and HADRON4 were kept the same as for the pion production experiment. The electrons were measured with BigBite and the protons with HADRON4.

In figures 4.13A and 4.13B the difference between z_{target} and z_{calc} is plotted for ^{4}He$(e,e'\,^4$He) and ^{1}H$(e,e'p)$, respectively. Both figures show that the vertex position deduced from the analysis of the scattered electron with BigBite is off by -1 cm. This is in good agreement with the result of the measurements with the carbon rods, already mentioned in section 4.1. The offset is interpreted as a shift

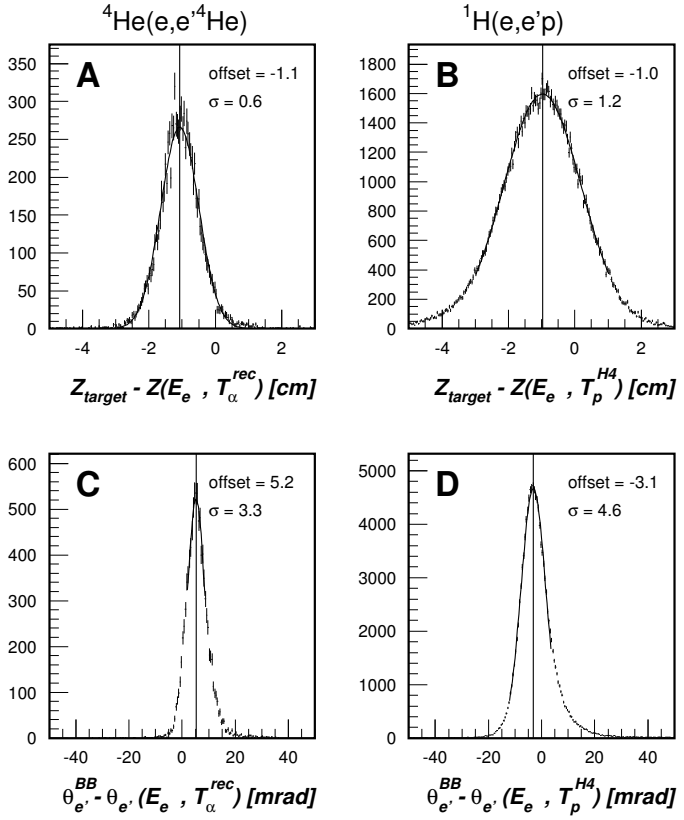

Figure 4.13: *Check on the vertex position provided by BigBite for* $^4\mathrm{He}(e,e'\,^4\mathrm{He})$ *(A) and* $^1\mathrm{H}(e,e'p)$ *(B). Check on* $\theta_{e'}^{\mathrm{BB}}$ *for* $^4\mathrm{He}(e,e'\,^4\mathrm{He})$ *(C) and* $^1\mathrm{H}(e,e'p)$ *(D).*

of the BigBite detector package in the direction of the electron beam, for which a correction is made in the analysis.

The width of the distribution shown in fig. 4.13A is mainly determined by BigBite and its value of 0.6 cm is consistent with the specified value of table 3.1. The energy and position resolution of HADRON4 are the largest contributors to the width of the distribution shown in fig. 4.13B.

In refs. [Bot99, Sam97, Lan98] an offset in $\theta_{e'}^{\mathrm{BB}}$ was observed when comparing $\theta_{e'}^{\mathrm{BB}}$ to the result of eq. (4.16) for $^4\mathrm{He}(e,e'\,^4\mathrm{He})$ coincidences between BigBite and the Recoil detector. The offsets varied between 3 and 7 mrad and were attributed

Table 4.1: *The observed offsets in the variables that are checked with the* $^4\mathrm{He}(e,e'\,^4\mathrm{He})$ *and the* $^1\mathrm{H}(e,e'p)$ *reactions are listed in the top half of the table. Possible corrections to the variables* $\theta_{e'}^{BB}$, $E_{e'}^{BB}$, E_e, T_A *(*T_α^{rec} *or* T_p^{H4}*), which are related by Eqs. (4.1) and (4.16), are given in the lower half of the table. The values are specified in the units cm, MeV and mrad.*

Observed offset in	Reaction channel	
	$^4\mathrm{He}(e,e'\,^4\mathrm{He})$	$^1\mathrm{H}(e,e'p)$
$z_{target} - z_{calc}$	-1.1	-1.0
$\theta_{e'}^{BB} - \theta_{e'}^{el}$	$+5.2$	-3.1
$E_{e'}^{BB} - E_{e'}^{el}$	-0.2	$+2.1$

Unchanged variables		Possible corrections to variables			
		$^4\mathrm{He}(e,e'\,^4\mathrm{He})$		$^1\mathrm{H}(e,e'p)$	
1	$\theta_{e'}^{BB}$, T_A	E_e: -5.3	$E_{e'}^{BB}$: -4.8	E_e: $+4.2$	$E_{e'}^{BB}$: $+1.4$
2	$E_{e'}^{BB}$, $\theta_{e'}^{BB}$	T_α^{rec}: $+0.23$	E_e: -0.5	T_p^{H4}: -0.25	E_e: $+2.5$
3	$E_{e'}^{BB}$, T_A	$\theta_{e'}^{BB}$: -4.8	E_e: -0.5	$\theta_{e'}^{BB}$: $+1.2$	E_e: $+2.4$
4	$E_{e'}^{BB}$			$\theta_{e'}^{BB}$: -4.8	T_p^{H4}: -1.4
				E_e: $+1.2$	

to a downward shift in the beam energy and/or a misalignment. A similar offset of 5.2 mrad is observed in fig. 4.13C. Furthermore, an offset of -0.2 MeV was found in $E_{e'}^{BB} - E_{e'}^{el}$, using eq. (4.1). A summary of the observed offsets is given in the upper half of table 4.1. Both offsets can be corrected for by shifting two or more of the variables involved in eqs. (4.1) and (4.16), namely E_e, $\theta_{e'}^{BB}$, $E_{e'}^{BB}$ and T_A (in this case T_α^{rec}). The following corrections were considered:

1. A correction of -5.3 MeV to E_e and -4.8 MeV to $E_{e'}^{BB}$. An overestimation of E_e by 5.3 MeV is just within the specifications of AmPS of 0.8%, but is unlikely.

2. A correction of $+0.23$ MeV to T_α^{rec} and -0.5 MeV to E_e. The correction to E_e is well within the specifications of AmPS. On the other hand, an underestimation of the kinetic energy of the ^{4}He nucleus in the Recoil detector by 0.23 MeV is unlikely, since the precision to which this energy is known is assumed to be better than 100 keV.

3. A correction of -4.8 mrad to $\theta_{e'}^{BB}$ and -0.5 MeV to E_e, which seems reasonable.

The possible corrections are listed in the lower half of table 4.1.

In fig. 4.13D the same comparison is made for the $^1\mathrm{H}(e,e'p)$ coincidences using the proton energy, T_p^{H4}, measured with HADRON4. In this case an offset of -3.1 mrad is observed. The observed offset in $E_{e'}^{BB} - E_{e'}^{el}$, using eq. (4.1), is $+2.1$ MeV. The same type of corrections as for the $^4\mathrm{He}(e,e'\,^4\mathrm{He})$ coincidences are evaluated:

1. A correction of $+4.2$ MeV to E_e and $+1.4$ MeV to $E_{e'}^{BB}$. An underestimation of E_e by 4.2 MeV seems unlikely. Moreover, this correction has a sign opposite to that deduced from the $^4\mathrm{He}(e,e'\,^4\mathrm{He})$ measurements.

2. A correction of -0.25 MeV to T_p^{H4} and $+2.5$ MeV to E_e. An overestimation of T_p^{H4} by 0.25 MeV is well possible, since the uncertainty on the proton energy in this energy range (60–80 MeV) is 0.8 MeV. An underestimation of the beam energy by 2.5 MeV is not unlikely.

3. A correction of $+1.2$ mrad to $\theta_{e'}^{BB}$ and $+2.4$ MeV to E_e. These corrections should be compared to those obtained with the $^4\mathrm{He}(e,e'\,^4\mathrm{He})$ coincidences, namely -4.8 mrad and -0.5 MeV for $\theta_{e'}^{BB}$ and E_e, respectively. Since the beam energy and the tuning of the storage ring were different for the $^4\mathrm{He}(e,e'\,^4\mathrm{He})$ and the $^1\mathrm{H}(e,e'p)$ measurements, the corrections to E_e may be different. On the other hand, the discrepancy between the two obtained corrections to $\theta_{e'}^{BB}$ (-4.8 and $+1.2$ mrad) is striking.

4. A correction of -4.8 mrad to $\theta_{e'}^{BB}$, $+1.2$ MeV to E_e and -1.4 MeV to T_p^{H4}. In this case we adopt the correction to $\theta_{e'}^{BB}$ of the $^4\mathrm{He}(e,e'\,^4\mathrm{He})$ measurements. However, an overestimation of T_p^{H4} of this size cannot be explained by uncertainties in the amount of material traversed by the proton.

In view of the inconsistencies in the $\theta_{e'}^{BB}$ offsets described above, it was decided not to correct $\theta_{e'}^{BB}$, $E_{e'}^{BB}$, T_p^{H4} and T_α^{rec} at all, thus introducing a systematic error of 4 mrad on $\theta_{e'}^{BB}$, which has implications for the determination of the target density (see section 4.9). The beam energy for the pion production measurements was corrected with $+2.4$ MeV, in order to compensate for the offset found in $E_{e'}^{BB} - E_{e'}^{el}$.

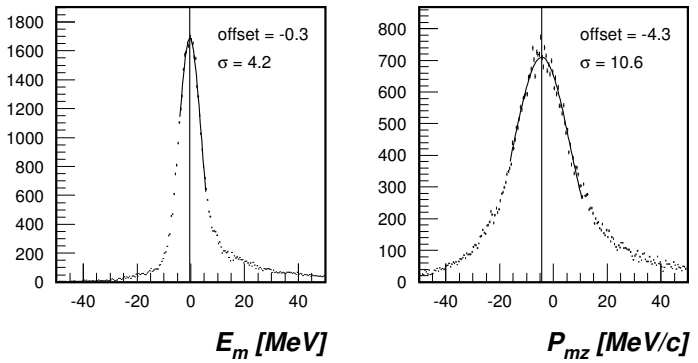

Figure 4.14: E_{m} *(left) and* p_{mz} *(right) for* $^4\mathrm{He}(e,e'p\,^3\mathrm{H})$ *coincidences. The tails on the right hand side of the distributions are due to radiative processes.*

Table 4.2: *The offsets and resolutions for the* E_{m}, p_{mx}, p_{my} *and* p_{mz} *distributions of* $^4\mathrm{He}(e,e'p\,^3\mathrm{H})$ *events.*

	E_{m}	p_{mx}	p_{my}	p_{mz}
offset	-0.3 MeV	-3.3 MeV/c	1.1 MeV/c	-4.3 MeV/c
σ	4.2 MeV	6.7 MeV/c	7.7 MeV/c	10.6 MeV/c

Quasi-elastic scattering: $^4\mathrm{He}(e,e'p\,^3\mathrm{H})$

Figure 4.14 shows the E_{m} and p_{mz} distributions for the triple coincidence data using the beam energy offset of 2.4 MeV. The offsets and resolutions of the distributions of E_{m}, p_{mx}, p_{my} and p_{mz} are shown in table 4.2. The uncertainties in the $\mathbf{p}_{\mathrm{m}}$ components are dominated by the uncertainty of the direction of the momentum of the recoiling nucleus $\mathbf{p}_{\mathrm{rec}}$, which is determined by the in-plane angular resolution of 24 mrad and the size of p_{rec}. The offsets are consistent with zero within the resolutions. Since they hardly influence the identification of the pions in the missing mass distributions (see section 4.5) and since the $^4\mathrm{He}(e,e'p\,^3\mathrm{H})$ and the $^4\mathrm{He}(e,e'p\,A)\pi$ events are located in totally different regions in the (E_{m}, p_{m}) space (which means that ad hoc corrections to E_{m} and $\mathbf{p}_{\mathrm{m}}$ based on the distributions for $^4\mathrm{He}(e,e'p\,^3\mathrm{H})$ events are not necessarily correct for pion production events), no corrections to E_{m} and $\mathbf{p}_{\mathrm{m}}$ are made.

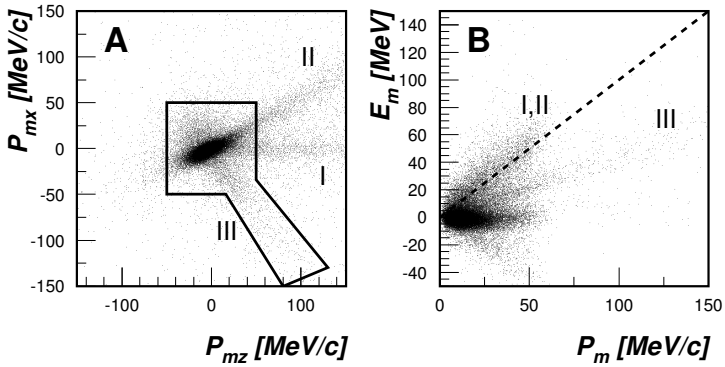

Figure 4.15: *The* ^{4}He$(e, e'p\,^3$H$)$ *events are selected by cutting on* p_{mx} *and* p_{mz} *(4.15A), resulting in the* $(E_{\mathrm{m}}, p_{\mathrm{m}})$ *spectrum of 4.15B. The meaning of the three bands is described in the text.*

4.5 Selection of the reaction channels

Selection of ^{4}He$(e, e'p\,^3$H$)$ events

As described in section 4.4 the quasi-elastic scattering events are identified by requiring $E_{\mathrm{m}} = 0$ and $\mathbf{p}_{\mathrm{m}} = \mathbf{0}$, since all particles involved in the reaction are detected. The detector resolutions cause a broadening of the E_{m} spectrum and of the spectra of the components of $\mathbf{p}_{\mathrm{m}}$. The best identification of the events is obtained by setting cuts on the values of the three components of $\mathbf{p}_{\mathrm{m}}$, as is shown for the x- and z-components in fig. 4.15A. The cuts set on p_{mx}, p_{my} and p_{mz} are 50, 40 and 50 MeV/c, respectively.

Band I and II contain the events in which a photon was emitted by the incident and by the scattered electron, respectively. Band III contains events for which the measured proton is not reconstructed properly. As discussed in section 4.3, the proton may lose a significant amount of energy in the HADRON4 detector due to hadronic interactions. The majority of these events is not identified as a proton and is rejected, which results in the reconstruction efficiency discussed in section 4.3. The remaining events are contained in band III, which is included in the cuts on $\mathbf{p}_{\mathrm{m}}$. Figure 4.15B shows $(E_{\mathrm{m}}, p_{\mathrm{m}})$ for the selected ^{4}He$(e, e'p\,^3$H$)$ events.

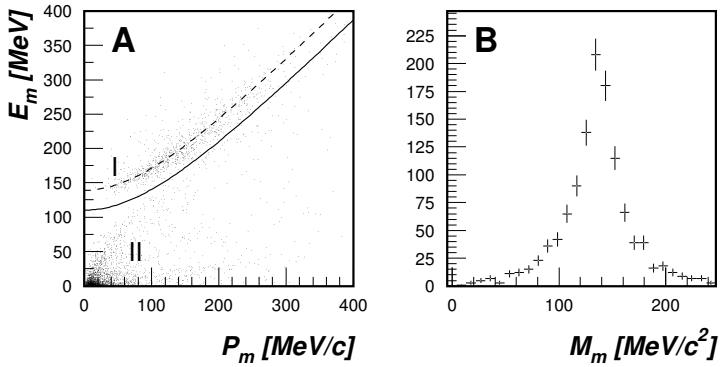

Figure 4.16: *The identification of the* ^{4}He$(e,e'p\,^3$He$)\pi^-$ *events is shown in the scatterplot of* E_m *versus* p_m *(A). The pion events are contained in band I. The resulting* M_m *spectrum is shown in (B).*

Selection of ^{4}He$(e,e'p\,A)\pi$ events

Events originating from pion production are characterized in the (E_m, p_m) spectrum by the relation $E_\mathrm{m} = \sqrt{m_\pi^2 + p_\mathrm{m}^2}$.

This is illustrated in fig. 4.16A for the ^{4}He$(e,e'p\,^3$He$)\pi^-$ events, which are located around the dashed curve given by $E_\mathrm{m} = \sqrt{m_\pi^2 + p_\mathrm{m}^2}$. Events above the solid line are marked as ^{4}He$(e,e'p\,^3$He$)\pi^-$ events. In fig. 4.16B these events are displayed as a function of the missing mass M_m defined as $M_\mathrm{m} = \sqrt{E_\mathrm{m}^2 - p_\mathrm{m}^2}$. The total number of identified ^{4}He$(e,e'p\,^3$He$)\pi^-$ events is about 1180. Tritons in the Recoil detector originating from the ^{4}He$(e,e'p\,^3$H) and ^{4}He$(e,e'p\,^3$H$)\gamma$ reactions that are misidentified as a Z=2 (^{3}He) particles, end up in band II in fig. 4.16A. However, these events, which constitute about 10% of the tritons, do not interfere with the pion band.

Figure 4.17A shows the (E_m, p_m) plot for ^{4}He$(e,e'p\,^3$H$)X$ events. Due to the limited resolution the band containing events from pion production, indicated by the dashed line, largely overlaps with the band containing events from the radiative tail of the ^{4}He$(e,e'p\,^3$H) reaction (band II), for which E_m and p_m are the energy and momentum of the emitted photon and hence $E_\mathrm{m} = p_\mathrm{m}$. The photon can be emitted either *before* or *after* the electron scatters off the nucleus. Because the electron usually emits the photon at a very small angle (peaking approximation), in the first case the photon is approximately collinear with the

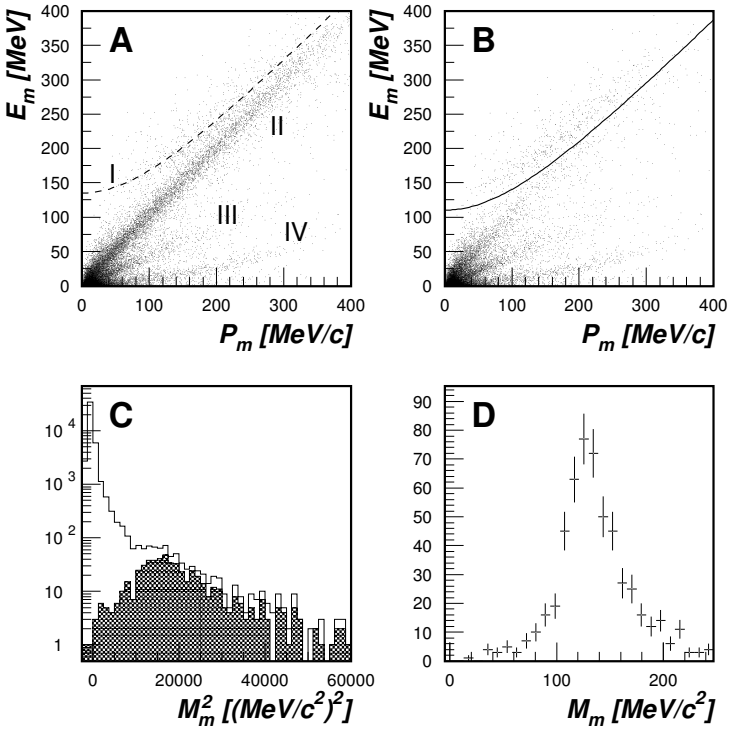

Figure 4.17: *A: E_m versus p_m for ^{4}He$(e,e'p\,^3$H$)X$ events. B: E_m versus p_m after collinearity cuts. C: M_m^2 spectrum with and without collinearity cuts. D: the M_m distribution after the cuts.*

incoming and in the second case with the scattered electron. By requiring that the angles between $\mathbf{p}_\mathrm{m}$ and both the incoming and outgoing electron exceed the values 0.3 and 0.2 rad, respectively, the largest fraction of the events due to radiative effects was eliminated. This is shown in fig. 4.17B. The events above the solid line are treated as pion events. In fig. 4.17C the M_m^2 spectrum is shown on a logarithmic scale with (shaded distribution) and without the collinearity cuts. Figure 4.17D shows the M_m distribution for the pion events only. About 25% of the ^{4}He$(e,e'p\,^3$H$)\pi^0$ events are lost by setting the collinearity cuts, leaving about 500 events.

The effect of the collinearity cuts on the available detection volume is shown in fig. 4.18. Panel A and B show the detection volume, calculated with the

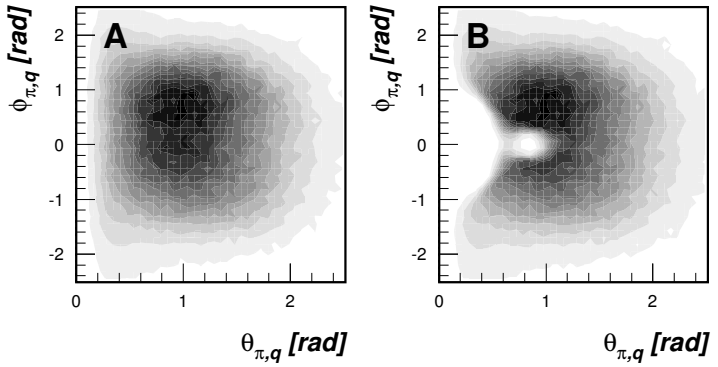

Figure 4.18: *The effect of the collinearity cuts. A: a greyscale plot of the covered detection volume in terms of $\theta_{\pi,\mathrm{q}}$ and $\phi_{\pi,\mathrm{q}}$ without the collinearity cuts. B: idem with the cuts.*

PHASPA9108 program (see section 4.7), in terms of $\theta_{\pi,\mathrm{q}}$ and $\phi_{\pi,\mathrm{q}}$ without and with the collinearity cuts. The detection volume has been weighted with the cross section for the ^{4}He$(e,e'p\,^3$H$)\pi^0$ reaction resulting from PWIA calculations with the model of ref. [Lee97].

4.6 Cell wall contribution

It has been shown in previous (double-) coincidence experiments performed at ITH [Sam97, Bot99], that there can be a sizeable yield of events in which the electron scattered off the nuclei in the wall of the storage cell instead of the target nuclei. In order to be able to estimate the contribution of such events measurements have been carried out with an empty storage cell. Unfortunately, it is not possible to subtract the number of triple coincidences measured with an empty cell from that measured with the filled cell, taking into account the 'collected charges' in both measurements. This is because the dimensions of the beam increase due to the interaction of the electrons with the target gas, thus increasing the number of interactions with the cell wall. This problem can be circumvented by selecting a reaction channel that is only accessible through scattering on the cell wall. The scaling factor is then given by the ratio between the yields for this reaction channel from the empty target and the ^{4}He target measurements, independently of the collected charge. For this purpose we used $(e,e'\,^4$He) double coincidences between the BigBite Recoil detectors. These coincidences cannot originate from the ^{4}He

target, since $\mathbf{q}$ always points towards the inner side of the storage ring and the Recoil detector is positioned on the outside. Even the coherent pion production reaction ^{4}He$(e,e'\,^4$He$)\pi^0$ cannot contribute to the $(e,e'\,^4$He) coincidences in the detector setup for triple coincidence measurements, since also in this case the largest fraction of $\mathbf{q}$ is transferred to the ^{4}He particle and the recoiling ^{4}He nucleus is always boosted towards the inner side of the ring. The number of $(e,e'\,^4$He) events recorded in the measurements with the filled and empty target was 517 and 68, respectively, resulting in a scaling factor of 7.6.

Next, the data measured with the empty target were analyzed in the same way as the data recorded with the filled target. After setting the pion identification cuts described in 4.5, the number of ^{4}He$(e,e'p\,^3$H) and ^{4}He$(e,e'p\,^3$He) coincidences were 0 and 1, respectively. After scaling these numbers with 7.6, the possible contribution of triple coincidences is less than 1%, so no corrections are made to the pion production data. For the ^{4}He$(e,e'p\,^3$H) reaction the same procedure was followed. In this case no event measured with the empty target passed the cuts, so again a correction is not needed.

4.7 Extraction of cross sections and detection volume

The n-fold differential cross sections for the reactions ^{4}He$(e,e'p\,^3$H) (n=5) and ^{4}He$(e,e'p\,A)\pi$ (n=8) are obtained from the expression

$$\frac{d^n\sigma}{d\mathcal{V}}(\mathbf{X}) = \frac{1}{\epsilon_t \int \mathcal{L}dt}\frac{N(\Delta\mathbf{X})}{V(\Delta\mathbf{X})}\eta_{\rm rad}, \tag{4.17}$$

where the volume element $d\mathcal{V}$ is equal to $(dE_{e'}d\Omega_{e'}d\Omega_p)$ for the ^{4}He$(e,e'p\,^3$H) reaction and to $(dE_{e'}d\Omega_{e'}dE_\pi d\Omega_\pi d\Omega_p)$ for the ^{4}He$(e,e'p\,A)\pi$ reaction. The vector $\Delta\mathbf{X}$ refers to bin widths for the kinematical variables $\mathbf{X}$ in which the cross section is expressed. In section 2.5, $\mathbf{X} = (W_{\pi N}, p_{\rm rec}, \theta_{\pi,q'}, T_\pi, \Delta\Phi$ and $\Phi)$ was chosen for the pion production reactions. For the quasi-elastic scattering process $\mathbf{X} = \mathbf{p}_{\rm rec}$. In the same formula, $N(\Delta\mathbf{X})$ is the experimental yield for the specific reaction channels and $V(\Delta\mathbf{X})$ is the detection volume. The normalization factor $\epsilon_t\int\mathcal{L}dt$ is equal to the integrated luminosity $\int\mathcal{L}dt$ times the tracking efficiency of BigBite, ϵ_t, which was not determined explicitly. The determination of $\epsilon_t\int\mathcal{L}dt$ is described in section 4.9. The correction factor $\eta_{\rm rad}$ accounts for radiative effects and is briefly described in section 4.8.

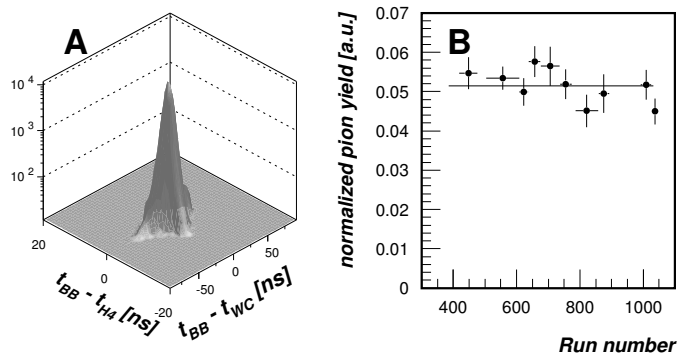

Figure 4.19: *A: the triple coincidence timing peak on a logarithmic scale. The time difference between BigBite and HADRON4 is shown versus the time difference between BigBite and the Recoil wire chamber. On the vertical axis the number of counts is shown. B: the normalized yield for the reaction* ^{4}He$(e, e'p\,A)\pi$ *plotted as a function of run number. Only statistical errors are shown.*

The experimental yield $N(\Delta\mathbf{X})$ is the number of pion events or quasi-elastic scattering events within the range $\Delta\mathbf{X}$, corrected for all determined inefficiencies:

$$N(\Delta\mathbf{X}) = \sum_i \frac{1}{g_i\,\epsilon_i} D(\mathbf{X}_i; \Delta\mathbf{X}), \tag{4.18}$$

where ϵ_i is the total efficiency for event i, which is the product of the detection and trigger efficiencies of all three detectors. The function $D(\mathbf{x}; \mathbf{R})$ is equal to unity if $\mathbf{x}$ is inside the region $\mathbf{R}$, and otherwise zero. The normalization function g_i is used to reduce the (known) dependence of the cross section on certain variables. The forms this function may take are described in section 2.5.

Because of the low luminosity in ITH (as compared to EMIN), the contribution of random triple coincidences to the experimental yield is negligible, as is shown in fig. 4.19A. In fig. 4.19B the experimental yield for the ^{4}He$(e, e'p\,A)\pi$ processes, including all efficiencies (except for ϵ_t, as is explained in section 4.9) and normalized to the collected charge per run, is shown as a function of run number. Only statistical errors are shown. The fluctuations of about 10% are probably due to both fluctuations in the target density and the inaccuracy (10%) with which the efficiency of the Recoil wire chamber was determined. For this plot the wire

chamber efficiency was determined as a function of selected runs, resulting in a lower accuracy than for the sum of all runs because of poorer statistics.

The probability that an event occurs in the domain $\Delta\mathbf{X}$, depends on the geometrical and energy acceptance of the detector setup. This is accounted for by the detection volume

$$V(\Delta\mathbf{X}) = \int D(\mathbf{X}(\mathbf{v}); \Delta\mathbf{X}) D(\mathbf{w}(\mathbf{v}), z; \mathbf{A}) f(z)\, d\mathbf{v} dz, \tag{4.19}$$

where $\mathbf{X}(\mathbf{v})$ is the set of observables, expressed as a function of the integration variable $\mathbf{v}$, which spans the volume $\mathcal{V}$. For the ^{4}He$(e, e'p\,A)\pi$ reaction $\mathbf{v}$ represents (E_π, Ω_π, $E_{e'}$, $\Omega_{e'}$, Ω_p) and for the ^{4}He$(e, e'p\,^3$H) reaction ($E_{e'}$, $\Omega_{e'}$, Ω_p). Furthermore, $\mathbf{A}$ is the acceptance of the detector setup, which depends on z, the vertex position along the beam direction, and on $\mathbf{w}(\mathbf{v})$, which stands for the momentum vectors of the detected particles, $\mathbf{p}_{e'}$, $\mathbf{p}_p$ and $\mathbf{p}_{rec}$, that can be calculated from $\mathbf{v}$ taking into account energy and momentum conservation. The function $f(z)$ takes the triangular density distribution of the ^{4}He nuclei in the storage cell into account.

Because of its complexity the integration had to be carried out numerically by Monte Carlo integration. The code `PHASPA9108` was used for this, which is based on the already existing code `Q2HPHASPA` [Gro00]. The detection volume is calculated as

$$V(\Delta\mathbf{X}) = \frac{N^{MC}(\Delta\mathbf{X}) V^{MC}}{N^{MC}_{gen}}, \tag{4.20}$$

where N^{MC}_{gen} is the total number of samples that is generated in the volume V^{MC} ($= \int d\mathbf{v}$), which can be calculated analytically. $N^{MC}(\Delta\mathbf{X})$ is the number of samples for which $\mathbf{X}$ is within the range $\Delta\mathbf{X}$.

In `PHASPA9108` the vector $\mathbf{v}$ is drawn homogeneously. Energy and momentum conservation is used to calculate the momenta of the remaining particles ($\mathbf{p}_{rec}$ and p_p in case of ^{4}He$(e, e'p\,A)\pi$). To account for the extended target the events are generated along the beam line according to the triangular distribution $f(z)$, as described in section 3.2. When $\mathbf{p}_{e'}$, $\mathbf{p}_p$ and $\mathbf{p}_{rec}$ are within the detector acceptance, the observables $\mathbf{X}$ are calculated and sorted in the same way as the experimental data.

In order to minimize the time needed for the calculation of one event, the detection efficiencies, energy losses and resolutions were not included in the detector response, but instead the data were corrected for these effects. In the Monte

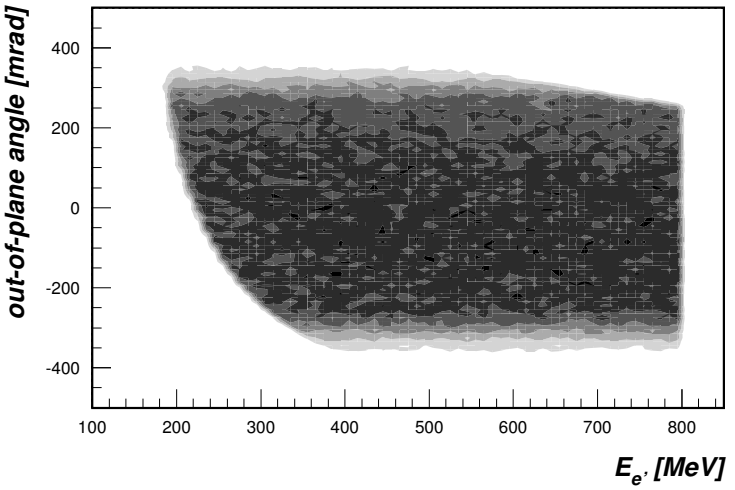

Figure 4.20: *Detection volume of BigBite as a function of the out-of-plane angle and* $E_{e'}$.

Carlo calculation the detectors are simply represented as geometrical objects with a specific energy acceptance, which can be hit or missed

The magnetic field of the BigBite dipole is approximated by a constant field, through which the electrons are tracked. The yoke of the magnet and the exit flange of fig. 3.4 are implemented as bounds on the geometrical acceptance of the spectrometer. In fig. 4.20 the calculated detection volume of BigBite for electrons is shown as a function of the out-of-plane angle and $E_{e'}$. The dependence of the acceptance on the energy and out-of-plane angle of the scattered electron is reproduced well (not shown).

The dependence of the detection volume for the ^{4}He$(e, e'p\,A)\pi$ reaction on the important kinematical variables $W_{\pi\mathrm{N}}$ and $\theta_{\pi,\mathrm{q}}$ is shown in fig. 4.21A. From this plot it can be clearly seen that the detection volume is largest at pion angles of about 0.5 rad and invariant energies near the pion production threshold. The detection volume is relatively small in the Δ-region (around 1232 MeV). This is also illustrated in fig. 4.21B, where a comparison is made between the measured $W_{\pi\mathrm{N}}$ distribution for ^{4}He$(e, e'p\,^3$He$)\pi^-$ events and the detection volume as a function of $W_{\pi\mathrm{N}}$, indicated by the dashed line.

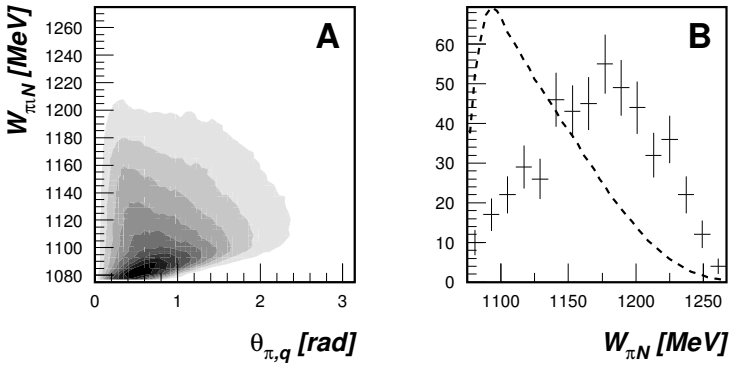

Figure 4.21: *A: detection volume for* ^{4}He$(e,e'p\,A)\pi$ *as a function of* $W_{\pi\mathrm{N}}$ *and* $\theta_{\pi,\mathrm{q}}$. *The steps in the greyscales are 10% of the maximum of the detection volume. B: the* $W_{\pi\mathrm{N}}$ *distribution of the* ^{4}He$(e,e'p\,^3$He$)\pi^-$ *data. The dashed line indicates the shape of the detection volume as a function of* $W_{\pi\mathrm{N}}$.

The result of the detection volume calculations for the ^{4}He$(e,e'p\,^3$H$)$ reaction is shown in the left panel of fig. 4.22 as a function of q and $T_{\mathrm{pt}}^{\mathrm{com}}$, which is the total kinetic energy of the proton and the triton in their center-of-momentum frame. The detection volume is larger for larger values of $T_{\mathrm{pt}}^{\mathrm{com}}$. Nevertheless, the experimental yields are largest at lower $T_{\mathrm{pt}}^{\mathrm{com}}$ values, because $T_{\mathrm{pt}}^{\mathrm{com}}$ is proportional to the momentum of the proton inside the nucleus, whose distribution is highest for the lowest momenta.

4.8 Radiative corrections

For events in which the electron emits a photon in the electromagnetic field of the target nucleus, the calculated value of E_{m} is larger than the real one. Depending on the cut set on E_{m} these events are possibly not accepted. To compensate for the loss of events due to these radiative processes, correction factors were calculated with the code `RADCOR` [Qui88], which takes the electron kinematics and the cutoff in E_{m} (corrected for the p_{m} dependence) as input parameters.

As described in section 4.5, the ^{4}He$(e,e'p\,^3$H$)$ events are selected by setting windows on the p_{m} components. These cuts result in an effective cut in E_{m}, as is illustrated in fig. 4.23. In this figure the E_{m} spectrum is shown (on a logarithmic

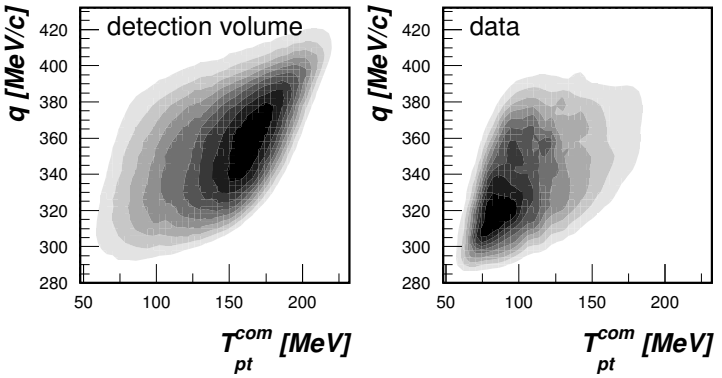

Figure 4.22: *The dependence of the detection volume on q and* $T_{\rm pt}^{\rm com}$ *(left), and the distribution of the measured* ^{4}He$(e,e'p\,^3$H$)$ *events in the (q,* $T_{\rm pt}^{\rm com}$*) phase space (right).*

scale) for all ^{4}He$(e,e'p\,^3$H$)$ events including the radiative tail events. The shaded part of the spectrum contains the events that pass the $p_{\rm m}$ cuts, which result in an effective cut in $E_{\rm m}$ of 55 MeV. The corresponding correction factor, is 1.08±0.01. The solid curve is the prediction by `RADCOR` for the $E_{\rm m}$ profile, normalized to the data and corrected for the $E_{\rm m}$ resolution of 4.2 MeV. The overshoot of the data between 10 and 60 MeV originates from events for which the proton energy was underestimated (see band III in fig. 4.15A).

For the pion production events the pion energy determined from $p_{\rm m}$ is subtracted from $E_{\rm m}$: $E'_{\rm m} = E_{\rm m} - \sqrt{p_{\rm m}^2 + m_\pi^2}$. The cutoff on $E'_{\rm m}$ was set at 50 MeV, resulting in a correction factor of 1.07±0.01.

4.9 Luminosity determination

Because the cross section for elastic scattering on ^{4}He is well known, the events from the reaction ^{4}He$(e,e')^4$He, which were measured simultaneously, could be used to determine a normalization factor for the quasi-elastic and pion production events. The program `MEFCAL` [Dre74] was employed to calculate the cross section

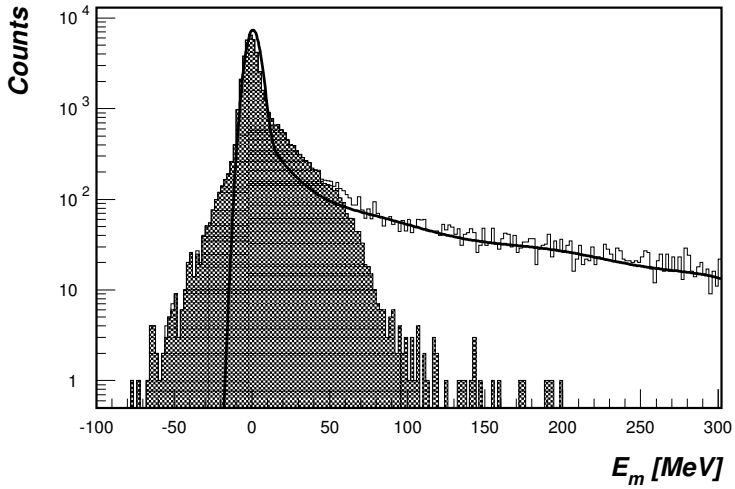

Figure 4.23: *The $E_{\rm m}$ spectrum for ^{4}He$(e,e'p\,^3$H$)$ events including the radiative tail. The shaded area contains the events used in the analysis.*

$\frac{d\sigma_{el}}{d\Omega_{e'}}$, using the ^{4}He ground state charge distribution [MCa77]. The normalization factor $\epsilon_{\rm t}\int\mathcal{L}dt$ is obtained using the relation

$$\epsilon_{\rm t}\int\mathcal{L}dt = \frac{N(\Delta Q^2)}{V(\Delta Q^2)}\eta_{\rm rad}\,/\,\frac{d\sigma_{el}}{d\Omega_{e'}}(\Delta Q^2), \tag{4.21}$$

where $\epsilon_{\rm t}$ is the tracking efficiency of BigBite, $\int\mathcal{L}dt$ is the integrated luminosity, and $\eta_{\rm rad}$ is a radiative correction factor. $N(\Delta Q^2)$ is the yield of the ^{4}He$(e,e')^4$He reaction as a function of Q^2, corrected for the trigger and Čerenkov efficiencies. $V(\Delta Q^2)$ is the detection volume as a function of Q^2, which is calculated with `PHASPA9108` (section 4.7) for the elastic scattering process. The tracking efficiency of BigBite, $\epsilon_{\rm t}$, is included in the normalization factor. This correction factor is the same for the ^{4}He$(e,e'\,^4$He$)$ and the triple coincidences, since they were measured simultaneously. Hence, $\epsilon_{\rm t}$ cancels in the expression for the cross section for the triple coincidence measurements. The identification of the elastic scattering events is illustrated on the left hand side in fig. 4.24, which shows the difference between $E_{\rm e'}^{\rm BB}$ (corrected for the dependence on $\phi_{\rm e'}^{\rm BB}$) and $E_{\rm e'}^{\rm el}$ (see eq. (4.1)). As shown, the energy cutoff is set at 10 MeV, resulting in a sample of more than 99% purity. The radiative correction factor was calculated with `RADCOR` (section 4.8) for this cutoff energy and it varied from 1.19 to 1.20 over the detection volume.

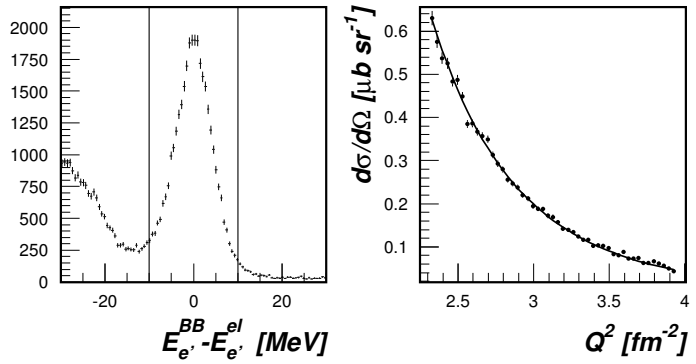

Figure 4.24: *Selection of elastic scattering events (left). Comparison of the calculated cross section with the data (right).*

The fitted value for $\epsilon_t \int \mathcal{L} dt$ is $2.6{\cdot}10^8$ μb^{-1}. On the right hand side of fig. 4.24 the comparison is made between the data and the model cross section, using this normalization factor. Using the integrated beam current of 77.3 kC and an assumed value of ϵ_t of 90% the calculated target density is $5.9{\pm}0.3{\cdot}10^{14}$ atoms/cm^2 averaged over the whole experimental period. The uncertainty in the offset in $\theta^{BB}_{e'}$ (see section 4.4) of 4 mrad causes an uncertainty of 5% on the determined value for $\epsilon_t \int \mathcal{L} dt$.

4.10 Error estimation

The statistical error on the cross section is determined by the uncertainty in the number of measured events and the uncertainty in the Monte Carlo integration of the detection volume. The number of events generated with `PHASPA9108` is chosen such that the latter contribution is smaller than 1%. The statistical error on the experimental yield is calculated according to (cf. eq. (4.18))

$$\sigma_{N(\Delta \mathbf{X})} = \sqrt{\sum_i \frac{1}{g_i^2 \epsilon_i^2} D(\mathbf{X}_i; \Delta \mathbf{X})}. \tag{4.22}$$

Various sources contribute to the systematic error associated with the cross sections. The systematic error in the normalization factor of 5% is determined by the assumed 2% uncertainty of the `MEFCAL` calculation and the uncertainties in the beam energy and, especially, $\theta_{e'}$. The inconsistency between the elastic scattering

measurements using the HADRON4 and the Recoil detector, respectively, showed that the error on $\theta_{e'}$ is 4 mrad. The Mott cross section is very sensitive to changes in $\theta_{e'}$ and E_e, and the systematic error in the normalization factor due to the uncertainty in $\theta_{e'}$ is 5%. On the other hand the ^{4}He$(e, e'p\,^3$H) cross section also contains the Mott cross section and the ^{4}He$(e, e'p\,A)\pi$ cross section contains Γ_v, which is proportional to it. Hence, this uncertainty partially cancels in the determination of $\rho_D(p_{rec})$ and the Γ_v reduced pion production cross section.

The error in the determination of the Čerenkov efficiency is estimated to be 2%.

The `GEANT` simulation that was performed to determine the reconstruction efficiency of HADRON4, has a limited reliability in the energy regime below 1 GeV. The uncertainty due to inaccuracies in the simulation is estimated to be 3%.

The product of the live times of the elements in a track in HADRON4 gives the value for the track live time. This value may be an underestimation if the live times in the energy-determining layers are correlated.
In the correction for the strongly varying rates of incident particles in ITH, the assumption was made that this rate is linearly dependent on the beam current. Especially for very high currents (higher than about 180 mA) this might not be true, and the live time might be overestimated.
The error associated with these effects is estimated to be 1%.

The energy-dependent efficiency of the wire chamber of the Recoil detector, including the particle identification cuts, is determined with an inaccuracy of 2%. The correction on the efficiency due to the impact angle, may be as large as 30–40% for the higher energy tritons, for which the detection efficiency is the lowest. The error on the correction for these particles is in the range 0–10%. However, averaged over all triton energies the contribution of this inefficiency to the systematic error is less than 2%.

As fig. 4.4 shows, a fraction of the Z=2 particles is identified as Z=1 particles and vice versa. This means that events from the π^0 (π^-) production channel are mistaken for events from the π^- (π^0) production channel. In principle the 'charge-id' spectrum has to be unfolded for each bin for which the cross section will be presented. This process is prone to errors because of the small statistical precision in the measurements, the varying gains of the Recoil wire chamber, and the large error on the overall mixing percentage between Z=1 and Z=2 particles. For this reason, no correction has been made in the analysis. The resulting systematic error is 2% for the ^{4}He$(e, e'p\,^3$He$)\pi^-$ reaction channel. The estimated error on

Table 4.3: *Sources contributing to the systematic error on the cross sections.*

Source	Effect on the cross section
Normalization determination	5%
Čerenkov efficiency	2%
HADRON4 track live time	1%
HADRON4 detector simulation	3%
Recoil WC efficiency	2%
Recoil 'charge-id'	2% (π^-), 5%–20% (π^0)
Detection volume calculation	3% +5%
Radiative corrections	1–2%
Total	**9%** (π^-), **10%–22%** (π^0)

the ^{4}He$(e, e'p\,^3$H$)\pi^0$ cross section depends on the ratio between the π^0 and π^- events for each bin and is, therefore, much larger in the Born region (up to 20%) than in the Delta region (up to 5%).

Misalignments of the three detectors and the storage cell cause errors in the estimation of their opening angles in the detection-volume integral. The error in the determined detection volume of BigBite cancels in the cross sections, because it enters in the determination of the detection volume for both the ^{4}He$(e, e'p\,A)\pi$ reaction and the ^{4}He$(e, e'\,^4$He) reaction, which is used for the normalization. The systematic error on the cross section introduced by the misalignments of the Recoil detector and HADRON4 is estimated to be 3%.

As shown in section 4.7 for both the ^{4}He$(e, e'p\,A)\pi$ and the ^{4}He$(e, e'p\,^3$H) reaction, the gradients in the detection volume are large as a function of the variables $W_{\pi\mathrm{N}}$, $\theta_{\pi,\mathrm{q}}$ and p_{rec}, which are selected for the presentations of the cross sections. This makes the integration of the detection volume very sensitive to errors in the kinematical variable. For the ^{4}He$(e, e'p\,^3$H) reaction the uncertainty on $\rho(p_{\mathrm{rec}})$ (section 5.1) associated with this effect is 5%. For the ^{4}He$(e, e'p\,A)\pi$ reaction channels, the introduced error in e.g. the $W_{\pi\mathrm{N}}$ dependence is 5% as well.

The error associated with the radiative corrections is 1–2%.

The systematic uncertainties discussed above are listed in table 4.3. The total systematic errors are obtained by adding the uncertainties quadratically, under the assumption that they are uncorrelated.

5 Results and discussion

In this chapter the results of the experiment are presented and discussed. The results for the ^{4}He$(e,e'p\,^3$H) reaction channel are shown in section 5.1, followed by the cross sections for the reactions ^{4}He$(e,e'p\,^3$H$)\pi^0$ and ^{4}He$(e,e'p\,^3$He$)\pi^-$, that are presented in section 5.2 as functions of various variables.

5.1 The ^{4}He$(e,e'p\,^3$H$)$ reaction

As mentioned in the sections 3.7 and 4.5, the majority of the triple coincidence events measured stem from the ^{4}He$(e,e'p\,^3$H$)$ reaction. These events and those from pion production were both analyzed with the method described in chapter 4. The cross section for quasi-elastic scattering is well known from other experiments [Bra88, Lee96] and can be effectively extrapolated to the kinematical regime of this study. This fact, in combination with the high yield ($4.1{\cdot}10^4$ events), makes the comparison between the cross sections determined in this study and the DWIA calculations an excellent check on the present analysis.

The five-fold differential cross section is commonly factorized as

$$\frac{d^5\sigma}{dE_{e'}d\Omega_{e'}d\Omega_p} = \frac{p_\mathrm{p}E_\mathrm{p}\sigma_{ep}}{R}\rho_D(\mathbf{p}_\mathrm{rec}), \tag{5.1}$$

where the recoil factor

$$R = 1 - \frac{E_\mathrm{p}}{E_\mathrm{rec}}\frac{\mathbf{p}_\mathrm{rec}\cdot\mathbf{p}_\mathrm{p}}{p_\mathrm{p}^2}, \tag{5.2}$$

and p_p, E_p, p_rec and E_rec are the momentum and total energy of the emitted proton and the recoiling nucleus, respectively; for the off-shell electron-proton cross section σ_{ep} commonly the σ_{cc1} prescription of ref. [For83] is used. In the plane-wave impulse approximation (PWIA) the distorted momentum-distribution $\rho_D(\mathbf{p}_\mathrm{rec})$ is interpreted as the momentum distribution $\rho(\mathbf{p}_\mathrm{rec})$ of the struck proton inside the nucleus. It is independent of the energy and momentum transfer, the dependence on which is contained in σ_{ep}. For this reason the comparison between theoretical predictions and experimental data is usually made on the

momentum-density level. The deviation from PWIA is largely attributed to final state interactions (FSI) and is treated in the distorted-wave impulse approximation (DWIA). These FSI effects depend on p_{rec}, and the total kinetic energy of the proton and the triton in their center-of-momentum frame, $T_{\mathrm{pt}}^{\mathrm{com}}$, which is defined as

$$T_{\mathrm{pt}}^{\mathrm{com}} = \sqrt{(M_{^4\mathrm{He}} + \omega)^2 - q^2} - (M_p + M_{^3\mathrm{H}}). \tag{5.3}$$

5.1.1 Comparison with DWIA calculations

In the DWIA calculations for the ^{4}He$(e, e'p\,^3$H) reaction a Woods-Saxon potential is used to describe the bound-state wave function of the proton and a Woods-Saxon type optical model potential to describe the wave function of the outgoing proton. The forms of these potentials are described in refs. [Sch82, Bra88]. In the present study the parameters of the potentials were adjusted in order to obtain a good description of the data acquired by Van den Brand [Bra88] (kinematics I and II) and Van Leeuwe [Lee96] (kinematics R and A) for triton momenta up to 300 MeV/c.

The distorted momentum-density for protons in ^{4}He determined in this experiment is presented in fig. 5.1. The value of $T_{\mathrm{pt}}^{\mathrm{com}}$ varies between 60 and 220 MeV for the data set. The measured momentum density is averaged over the acceptance in ω (100–250 MeV), q (300–420 MeV/c) and $\theta_{\mathrm{p,q}}$ (0°–20°). The excess of strength in the data in the region 145–160 MeV/c and the deficiency in the region 160–180 MeV/c is caused by the dead layer of the SiY silicon detector (see section 4.2). Particles that are stopped in this dead layer, do not produce a signal in the SiY detector. Hence, their energy is underestimated. This effect is not taken into account in the Monte Carlo simulation and, therefore, shows up in the momentum density spectrum as a shift of strength from the higher to the lower momenta. The integral over p_{rec}, however, is not affected.

On average the results of the DWIA calculations are 5% larger than the data. This can be due to:

- the systematic uncertainties in the momentum densities measured by Van den Brand (5.7–6.1%) and Van Leeuwe (5%).
- The uncertainty in the DWIA calculations, which is 5–10% because of the differences in the accepted range in $T_{\mathrm{pt}}^{\mathrm{com}}$ for the various experiments.

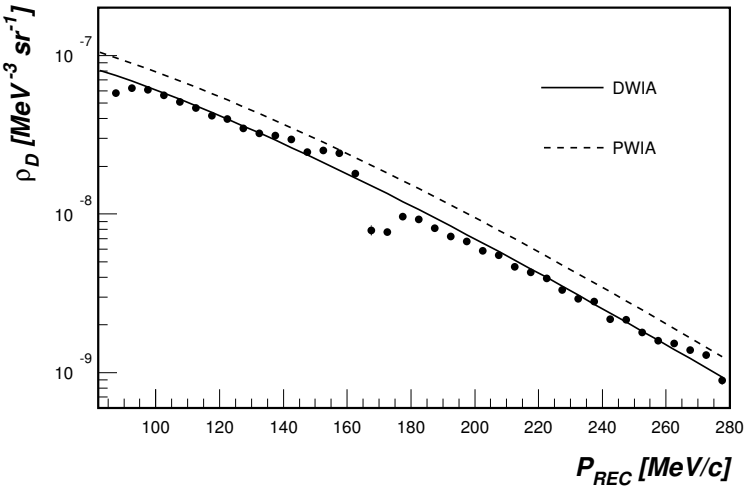

Figure 5.1: *The (distorted) momentum density for the reaction* ^{4}He$(e,e'p\,^3$H$)$. *The DWIA calculation is given by the solid curve, the PWIA calculation by the dashed curve.*

- The systematic error in the determined target thickness, which is highly sensitive to how accurately $\theta_{e'}^{\mathrm{BB}}$ is known and amounts to 5%.
- The uncertainty in the detection volume as a function of p_{rec} (large gradient), estimated to be 5%.

Taking the systematic errors into account, one can conclude that the data and the DWIA calculations are in good agreement; therefore no renormalization was done.

5.2 Pion production

In chapter 4 the extraction of the cross sections for the ^{4}He$(e,e'p\,^3$He$)\pi^-$ and ^{4}He$(e,e'p\,^3$H$)\pi^0$ reactions has been discussed. As argued in chapter 2, these cross sections depend on seven independent observables, for which p_{rec}, $W_{\pi\mathrm{N}}$, $\theta_{\pi,\mathrm{q}'}$, T_π, q (or Q^2), $\phi_{\pi,\mathrm{q}'}$ (or $\Delta\Phi$) and Φ have been chosen. Since the dependence on the momentum transfer q is weak (especially for $d^5\sigma_v$), this dependence will not be discussed. The small number of triple coincidences in both reaction channels

Table 5.1: *The ranges spanned by the most relevant variables in quasi-free pion production.*

Observable	Range	Observable	Range
p_{rec}	100–250 MeV/c	$W_{\pi\mathrm{N}}$	threshold–1250 MeV/c^2
T_π	0–200 MeV	$\theta_{\pi,\mathrm{q}'}$	0°–180°
Φ	20°–220°	$\Delta\Phi$	0°–360°
$\phi_{\pi,\mathrm{q}'}$	−90°–90°	Q^2	0.03–0.08 GeV^2
ω	250–450 MeV	q	350–500 MeV/c
T_p	35–200 MeV	ϵ	0.5–0.8

only allows a presentation of the cross section as a function of one variable, while averaging over the other ones within the detection volume. For convenience we use in the remainder of this chapter the term 'cross section' instead of the 'differential cross section as a function of a variable, while averaging over the other variables within the detection volume'.

The detection volumes for the pion production reaction channels span a wide range for most of the observables. In Table 5.1 the ranges for some of these quantities are listed. Since, the observables ω, ϵ and T_p cannot be chosen independently from the set described above, their influence on the cross section is not discussed.

The data are compared to the results of PWIA and DWIA calculations performed with the model of Lee *et al.* [Lee97]. In the optical potentials for the bound nucleon and the outgoing proton the same sets of parameters were used as for the $^4\mathrm{He}(e,e'p\,^3\mathrm{H})$ reaction, described in the previous section. The parameters in the potential that accounts for the pion-nucleus interaction in the final state have been taken from Lee [Lee97].

5.2.1 Dependence on p_{rec}

Just as the cross section for quasi-free proton knock-out, the quasi-free pion production cross section strongly depends on the initial momentum of the struck nucleon, which is equal to $-\mathbf{p}_{\mathrm{rec}}$ $(= -\mathbf{p}_{\mathrm{A}-1})$ in the PWIA approximation. The dependence of the cross section on this variable is shown in the upper half of fig. 5.2 for the neutral (left) and the charged (right) pion production channel. For both reaction channels the data agree well with the DWIA calculations. The dependence

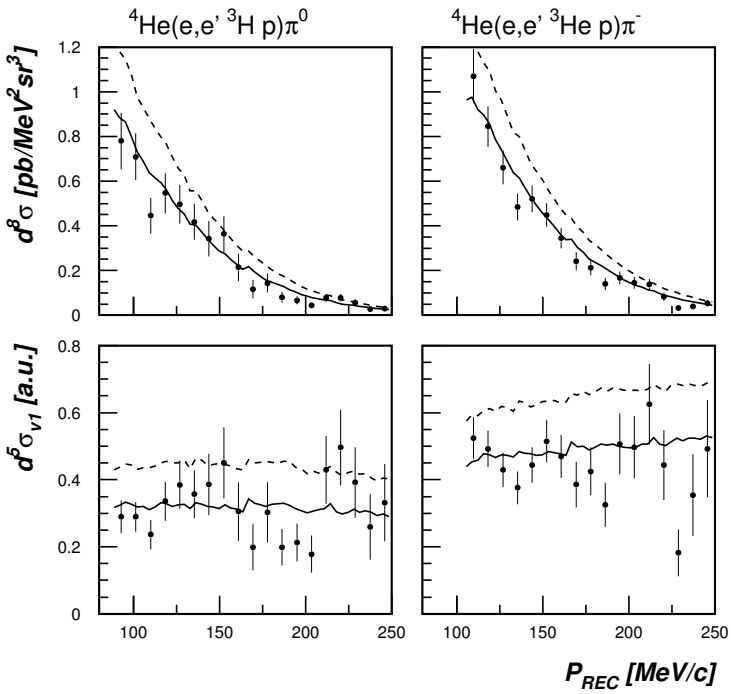

Figure 5.2: *Upper part: the cross sections* $d^8\sigma$ *for* $^4\mathrm{He}(e,e'p\,^3\mathrm{H})\pi^0$ *and* $^4\mathrm{He}(e,e'p\,^3\mathrm{He})\pi^-$ *as a function of* p_{rec}*. Lower part: the reduced cross sections* $d^5\sigma_{v1}$ *for* $^4\mathrm{He}(e,e'p\,^3\mathrm{H})\pi^0$ *and* $^4\mathrm{He}(e,e'p\,^3\mathrm{He})\pi^-$ *as a function of* p_{rec}*. The results of the DWIA calculations are given by the solid curves and those of the PWIA calculations by the dashed curves.*

of the pion production cross sections on p_{rec} is identical to that of the momentum density determined from the $^4\mathrm{He}(e,e'p\,^3\mathrm{H})$ reaction, shown in fig. 5.1. This indicates that pion production can overall be described as a quasi-free process. The irregularity due to the dead layer of the SiY silicon detector, which was described in the section 5.1, is also present in the data for the $^4\mathrm{He}(e,e'p\,^3\mathrm{H})\pi^0$ reaction, although less visible due to the larger statistical errors. The $^4\mathrm{He}(e,e'p\,^3\mathrm{He})\pi^-$ data do not show this behaviour; this is due to the fact that the ^{3}He particles do not reach the dead layer of the SiY detector.

In the lower half of fig. 5.2 the reduced cross sections $d^5\sigma_{v1}$ are plotted for both reactions. In this case the p_{rec} dependence of the square of the nucleon bound-

state wave function, as calculated using the Woods-Saxon potential mentioned in section 5.1.1, has been removed from the data as well as from the calculations (cf. section 2.5). The resulting cross sections are nearly constant, in accordance with the conclusion drawn from the $d^8\sigma$ distributions. The irregularities in the theoretical cross sections are caused by the limited statistical precision in the Monte Carlo data.

5.2.2 Dependence on $W_{\pi\mathrm{N}}$

The effect of intermediate Delta excitation is reflected most clearly in the dependence of the cross section on $W_{\pi\mathrm{N}}$. The expected signature of the Δ-resonance is clearly visible in fig. 5.3, which shows the cross section as a function of $W_{\pi\mathrm{N}}$ for the two pion production channels (upper half) and the reduced cross section $d^5\sigma_{v1}$ (lower half). The strong reduction of the contribution of the Born terms to the cross section for neutral pion production below 1150 MeV is evident in the data as well as in the calculated cross sections. Generally, the DWIA calculations describe the data very well, but in the 'Born region' the experimental strength for *neutral* pion production is larger than calculated. This discrepancy is most likely due to the presence of Z=2 (^{3}He) particles in the Z=1 (^{3}H) band in the 'charge-id' spectrum of the particles measured in the Recoil detector (see fig. 4.4), in combination with the very low yield of tritons in this $W_{\pi\mathrm{N}}$ region.

In section 2.3 it has been argued that for momenta of the recoiling nucleus larger than approximately 250 MeV/c, nucleon knockout and pion production no longer can be considered as quasi-free reactions. However, fig. 5.4 shows that already for $p_{\mathrm{rec}} > 180$ MeV/c deviations from a quasi-free reaction mechanism in the $^4\mathrm{He}(e,e'p\,^3\mathrm{H})\pi^0$ reaction occur. In this figure the cross section $d^8\sigma$ and the reduced cross section $d^5\sigma_{v1}$ are displayed as a function of $W_{\pi\mathrm{N}}$ for three slices in p_{rec}. Both the non-reduced and the reduced cross section are systematically smaller for $p_{\mathrm{rec}} > 180$ MeV/c *and* $W_{\pi\mathrm{N}} > 1180$ MeV than the calculated cross section. The trend in the non-reduced and the reduced cross sections is similar for the reaction $^4\mathrm{He}(e,e'p\,^3\mathrm{He})\pi^-$, though less pronounced (not shown). The effect may be due to more complicated rescattering mechanisms in the final state that are not taken into account by the optical models. For example πp rescattering removes strength in the Delta region towards smaller values of p_{rec}. The discrepancies may also be a hint that a Δ-hole description is required. To ensure that the

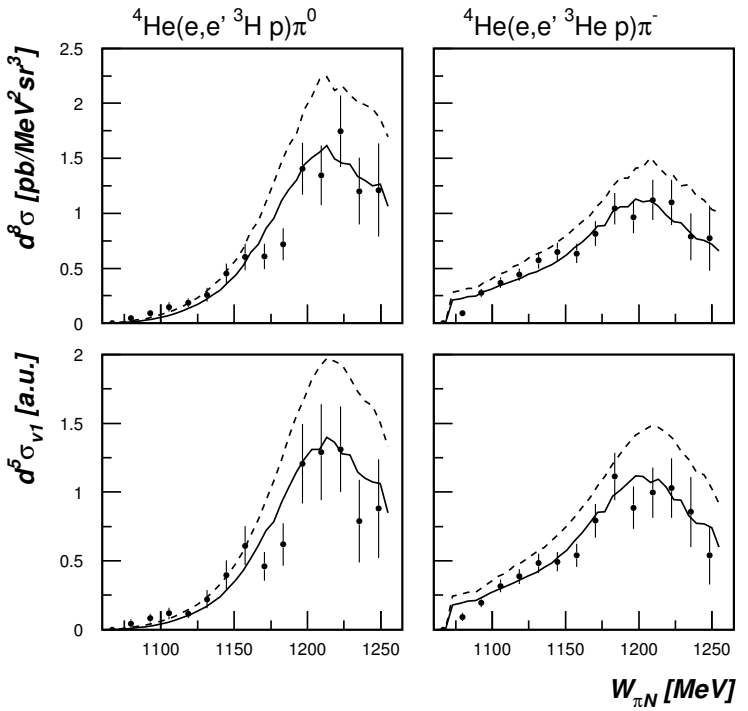

Figure 5.3: *Upper half: the cross sections for neutral and charged pion production as a function of $W_{\pi\mathrm{N}}$. Lower half: the reduced cross sections $d^5\sigma_{v1}$ as a function of $W_{\pi\mathrm{N}}$. The results of the DWIA calculations are given by the solid curves and those of the PWIA calculations by the dashed curves. Only events with $p_{\mathrm{rec}} \leq 180$ MeV/c are used.*

data correspond to quasi-free pion production, only events with $p_{\mathrm{rec}} \leq 180$ MeV/c will be considered in the following.

In the region of the Δ-resonance ($1175 < W_{\pi\mathrm{N}} < 1290$ MeV) the isospin dependence of the cross section is also reflected in the ratio between the cross sections $^4\mathrm{He}(e,e'p\,^3\mathrm{H})\pi^0$ and $^4\mathrm{He}(e,e'p\,^3\mathrm{He})\pi^-$. The isospin dependent parts of the transition amplitudes for pion photoproduction via intermediate Delta excitation read as

$$\langle \gamma p\,|\Delta^+|\pi^0 p\rangle \propto \langle \gamma p\,|T=\tfrac{3}{2}, T_z=\tfrac{1}{2}\rangle\langle T=\tfrac{3}{2}, T_z=\tfrac{1}{2}|\pi^0 p\rangle \qquad (5.4)$$

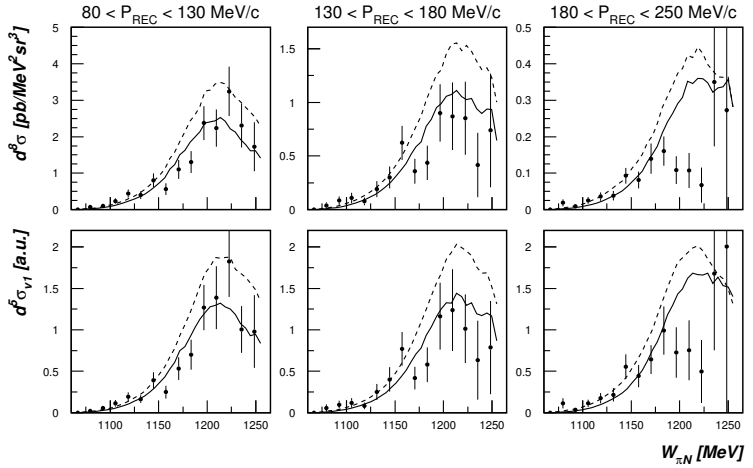

Figure 5.4: *The non-reduced (upper half) and reduced (lower half) cross sections for* ^{4}He$(e,e'p\,^3$H$)\pi^0$ *as a function of* $W_{\pi\mathrm{N}}$ *for three ranges in* p_{rec} *(from left to right): 80–130* MeV/c*, 130–180* MeV/c *and 180–250* MeV/c.

and

$$\langle \gamma n\,|\Delta^0|\pi^- p\rangle \propto \langle \gamma n\,|T=\tfrac{3}{2},T_z=-\tfrac{1}{2}\rangle\langle T=\tfrac{3}{2},T_z=-\tfrac{1}{2}|\pi^- p\rangle, \tag{5.5}$$

where T and T_z are the isospin and the z-component of the isospin of the hadronic system, respectively. The amplitudes for excitation of the Δ-resonance in the interaction of a real or virtual photon with a proton and a neutron are equal because of the $T_z \leftrightarrow -T_z$ symmetry. Therefore, making use of Clebsch-Gordan coefficients, one obtains for the ratio of the transition amplitudes

$$\frac{\langle \gamma p\,|\Delta^+|\pi^0 p\rangle}{\langle \gamma n\,|\Delta^0|\pi^- p\rangle} = \frac{\langle T=\frac{3}{2},T_z=\frac{1}{2}|\pi^0 p\rangle}{\langle T=\frac{3}{2},T_z=-\frac{1}{2}|\pi^- p\rangle} = \frac{\sqrt{\frac{2}{3}}}{\sqrt{\frac{1}{3}}} = \sqrt{2} \tag{5.6}$$

and hence for the ratio of the cross sections

$$\frac{\sigma(^4\mathrm{He}(e,e'p\,^3\mathrm{H})\pi^0)}{\sigma(^4\mathrm{He}(e,e'p\,^3\mathrm{He})\pi^-)} = 2. \tag{5.7}$$

In fig. 5.5 this ratio is shown for the data as well as the results of the calculations as a function of $W_{\pi\mathrm{N}}$. On the left side the ratio is shown for the non-reduced cross

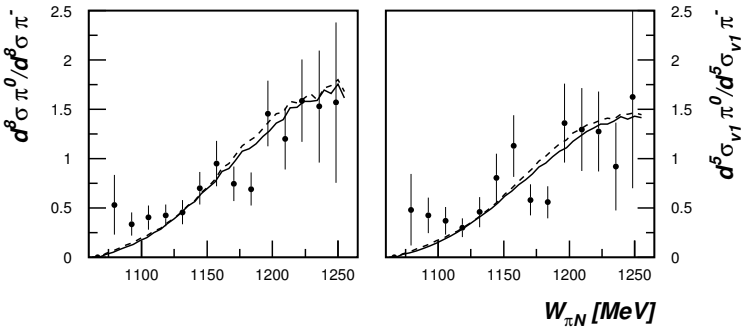

Figure 5.5: *Ratio between the cross sections for π^0 and π^- production as a function of $W_{\pi\mathrm{N}}$. On the left the ratio between the non-reduced cross sections is shown and on the right the ratio between the reduced cross sections $d^5\sigma_{v1}$. Only events with $p_{\mathrm{rec}} \leq 180$ MeV/c are used.*

section $d^8\sigma$ and on the right for the reduced cross section $d^5\sigma_{v1}$. The agreement between the data and the calculated results is good in both cases. The ratio between the non-reduced cross sections reaches its maximum of 1.7 at $W_{\pi\mathrm{N}} = 1250$ MeV, for the PWIA as well as the DWIA calculations (so the effect of distorted waves cancels). The deviation from the expected ratio of 2 can be explained by the neglect of the Born terms in the derivation above, which are especially important for the reaction $^4\mathrm{He}(e,e'p\,^3\mathrm{He})\pi^-$, even for the larger values of $W_{\pi\mathrm{N}}$. The ratio between the *reduced* cross sections is, with a maximum of 1.4, smaller than in the *non-reduced* case. Apparently, the method of reducing the cross section affects the relative importance of events in the Born and Delta region. For $W_{\pi\mathrm{N}} < 1120$ MeV the ratios of the measured cross sections are systematically larger than the ratios of the calculated ones. This is probably caused by a misidentification of the ^{3}H and the ^{3}He recoiling nuclei, already mentioned before.

5.2.3 Dependence on $\theta_{\pi,\mathrm{q}'}$

Another signature of intermediate Delta excitation is observed in the dependence of the differential cross section on $\theta_{\pi,\mathrm{q}'}$. This dependence is shown in fig. 5.6 for the $^4\mathrm{He}(e,e'p\,^3\mathrm{H})\pi^0$ and $^4\mathrm{He}(e,e'p\,^3\mathrm{He})\pi^-$ reaction channels in the left and right column, respectively, together with the calculated cross sections. In the upper half the cross sections $d^8\sigma$ are presented and in the lower half the reduced cross

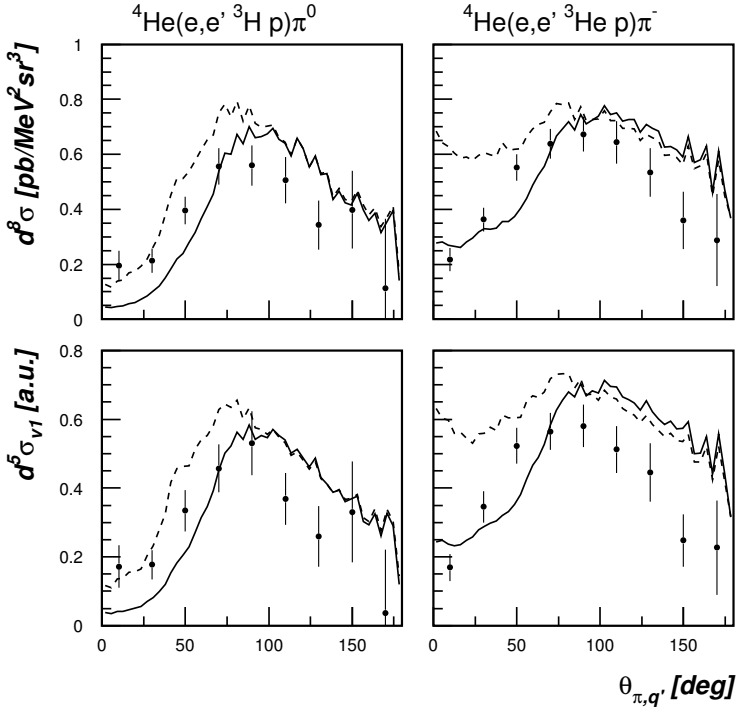

Figure 5.6: *Dependence of $d^8\sigma$ (top) and $d^5\sigma_{v1}$ (bottom) on $\theta_{\pi,\mathrm{q}'}$ for the reactions $^4\mathrm{He}(e,e'p\,^3\mathrm{H})\pi^0$ (left) and $^4\mathrm{He}(e,e'p\,^3\mathrm{He})\pi^-$ (right). The results of the DWIA calculations are given by the solid curves and those of the PWIA calculations by the dashed curves. Only events with $p_{\mathrm{rec}} \leq 180$ MeV/c are used.*

sections $d^5\sigma_{v1}$. The effect of Delta excitation is most clearly visible in the PWIA calculations for the π^0 channel, as they peak around 77° (equivalent to 120° in the γ^*N center-of-momentum frame). This value corresponds to the maximum of the angular dependence of the cross section for pion production by intermediate Delta excitation on a nucleon. For this process the angular distributions of the partial cross sections $\frac{d^2\sigma_{\mathrm{T}}}{d\Omega_\pi}$, $\frac{d^2\sigma_{\mathrm{L}}}{d\Omega_\pi}$ and $\frac{d^2\sigma_{\mathrm{TT}}}{d\Omega_\pi}$ all reach their maximum at $\theta^{cm}_{\pi,\mathrm{q}'} = 90°$, but the angular distribution for $\frac{d^2\sigma_{\mathrm{LT}}}{d\Omega_\pi}$ is responsible for the shift from $\theta^{cm}_{\pi,\mathrm{q}'} = 90°$ to $\theta^{cm}_{\pi,\mathrm{q}'} = 120°$ in the angular distribution of $\frac{d^2\sigma}{d\Omega_\pi}$. The effect of the Born terms is most apparent in the shape of the PWIA cross section for the π^- channel; they generate additional strength for small and large values of $\theta_{\pi,\mathrm{q}'}$. The use of the

distorted pion and proton waves in the DWIA calculations reduces the calculated cross sections for $\theta_{\pi,q'} < 90°$.

The cross sections for both reaction channels are overestimated by the PWIA calculations. On the other side, they are underestimated by the DWIA calculations for $\theta_{\pi,q'} < 75°$ and overestimated for larger values of $\theta_{\pi,q'}$. An explanation for this discrepancy at small angles might be that the way the distortions are calculated is not adequate; they are too strong for small values of $\theta_{\pi,q'}$, and not strong enough for larger values. This is supported by the observed dependence of the cross sections on T_π, shown in fig. 5.8 in section 5.2.4, knowing that within the detection volume of this experiment there exists a correlation between $\theta_{\pi,q'}$ and T_π: large values of T_π correspond to small values of $\theta_{\pi,q'}$ and vice versa. The dependence of the cross sections on T_π is, therefore, reversed with respect to the dependence on $\theta_{\pi,q'}$: an overestimation of the cross sections by the DWIA calculations for smaller values of T_π and an underestimation for larger values. In an experiment studying the reaction $^{16}\mathrm{O}(\gamma,\pi^- p)$ [Ude97, Ude98] similar deviations were found for small values of $\theta_{\pi,q'}$. No consistent explanation in terms of medium effects or E2/M1 ratios could be given there for the differences.

The discrepancies between the data and the calculations show up more clearly in fig. 5.7. In this figure $d^8\sigma$ is shown as a function of $\theta_{\pi,q'}$ for two different $W_{\pi N}$ slices: $W_{\pi N} < 1160$ MeV, the Born region, and $1160 < W_{\pi N} < 1260$ MeV, the Δ-resonance region. For the smaller value of $W_{\pi N}$ the results of the DWIA calculations describe the $^4\mathrm{He}(e,e'p\,^3\mathrm{He})\pi^-$ data fairly well, whereas there is a difference between the DWIA calculations and the data for the reaction $^4\mathrm{He}(e,e'p\,^3\mathrm{H})\pi^0$ at small values of $\theta_{\pi,q'}$. Again, this is probably the result of the misidentification of the charge of part of the recoiling nuclei in the Recoil detector, which is especially important in regions of the phase space where the $^4\mathrm{He}(e,e'p\,^3\mathrm{He})\pi^-$ cross section is much larger than that for $^4\mathrm{He}(e,e'p\,^3\mathrm{H})\pi^0$, e.g. the kinematic domain in which the Born terms in the πN interaction are dominant: small values of $W_{\pi N}$ and small (and large) values of $\theta_{\pi,q'}$. For the larger value of $W_{\pi N}$ the discrepancies are similar for both reaction channels: underestimation of the data by the DWIA calculations at small values of $\theta_{\pi,q'}$ and overestimation at larger values of $\theta_{\pi,q'}$. In summary, the data are described well in the Born region (small $W_{\pi N}$, small and large $\theta_{\pi,q'}$) and there are clear deviations in the Delta region. The fact that the DWIA calculations do not describe the data very well in the Delta region, might be an indication that a Δ-hole description or medium modifications to the Delta propagator are needed for a correct description of the pion production pro-

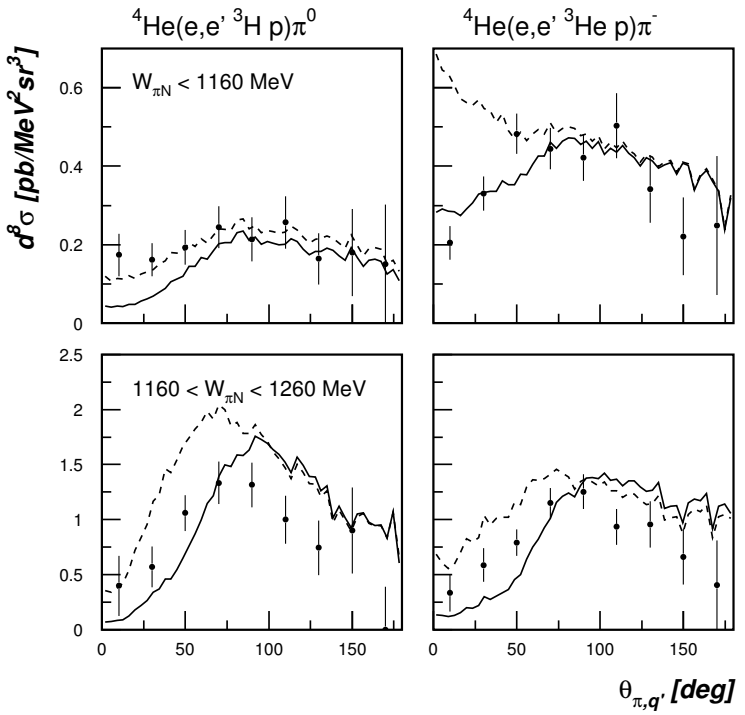

Figure 5.7: *Dependence of* $d^8\sigma$ *on* $\theta_{\pi,\mathrm{q}'}$ *for the reactions* $^4\mathrm{He}(e,e'p\,^3\mathrm{H})\pi^0$ *(left column) and* $^4\mathrm{He}(e,e'p\,^3\mathrm{He})\pi^-$ *(right column) for two different* $W_{\pi\mathrm{N}}$ *slices:* $W_{\pi\mathrm{N}}$ *threshold–1160 MeV (top) and 1160–1260 MeV (bottom). Only events with* $p_{\mathrm{rec}} \leq 180$ MeV/c *are used.*

cess. In recent studies of the σ_{T}, σ_{L} and σ_{LT} cross sections for $^3\mathrm{He}(e,e'\pi^+)$ it was shown that medium modifications to the self-energy of the Delta in its propagator are needed in order to describe the data [Blo97, Koh02]. It is noteworthy that especially the σ_{LT} term, which is responsible for the asymmetry in the $\theta_{\pi,\mathrm{q}'}$ distributions, is sensitive to the medium modifications [Koh02]. This may explain why also in the present experiment the discrepancies are especially large in the $\theta_{\pi,\mathrm{q}'}$ distributions.

5.2.4 Dependence on T_π

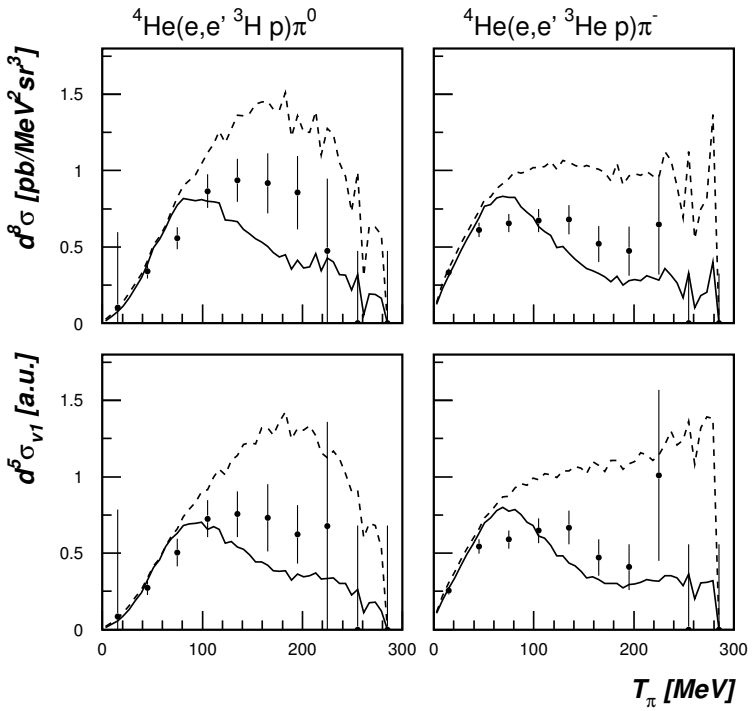

Figure 5.8: *Cross sections $d^8\sigma$ (top) and $d^5\sigma_{v1}$ (bottom) as a function of T_π for the neutral (left) and charged (right) pion production reaction channel. The results of the DWIA calculations are given by the solid curves and those of the PWIA calculations by the dashed curves. Only events with $p_{\rm rec} \leq 180$ MeV/c are used.*

In the previous section it has been argued that possibly the distortions in the DWIA calculations are too strong in the Delta region at small values of $\theta_{\pi,q'}$. One should realize that the uncertainties in the optical potentials for ^{3}H and ^{3}He are much larger for pion waves than for proton waves. As a matter of fact, the pion-nucleus optical potential used in the calculations, has only been verified for pion kinetic energies T_π up to 50 MeV. For energies above 50 MeV an extrapolation is made [Car82, Str79]. In this respect it is interesting to investigate the dependence of the cross section on T_π. The dependence of $d^8\sigma$ and $d^5\sigma_{v1}$ on T_π for both reaction channels is displayed in fig. 5.8. The shape of the distributions is for a large part determined by the (positive) correlation between T_π and $W_{\pi\rm N}$

in the detection volume, which explains the differences between the data for the ^{4}He$(e,e'p\,^3$H$)\pi^0$ and ^{4}He$(e,e'p\,^3$He$)\pi^-$ reactions: for $T_\pi < 80$ MeV (lower $W_{\pi\mathrm{N}}$) the cross sections $d^8\sigma$ and $d^5\sigma_{v1}$ are relatively large for the charged pion channel, while this is opposite for $T_\pi > 80$ MeV (higher $W_{\pi\mathrm{N}}$). For both reaction channels, the data are well described by both the DWIA and PWIA calculations in the region where the distortions are small: $T_\pi < 50$ MeV (consistent with the range covered for which the pion-nucleus optical potential has been verified). The data are overestimated by both calculations between 50 and 100 MeV, while from 100 MeV upwards the DWIA calculations underestimate and the PWIA calculations overestimate the data. As mentioned in the previous section, this is consistent with the deviations between the measured and calculated cross sections as a function of $\theta_{\pi,\mathrm{q}'}$. The conclusion is that for $T_\pi > 100$ MeV the (pion) distortions seem to be too strong. On the other hand, the distortions seem not strong enough for $50 < T_\pi < 100$ MeV, suggesting that besides a more adequate optical model for the pion, a Δ-hole model description or medium modifications to the Delta propagator may be required.

5.2.5 Dependence on $\phi_{\pi,\mathrm{q}'}$, Φ and $\Delta\Phi$

In this section the dependence of the cross section on the variables $\phi_{\pi,\mathrm{q}'}$, Φ and $\Delta\Phi$ is discussed. Within the detection volume each of these variables is strongly correlated with $W_{\pi\mathrm{N}}$, which to a large extent determines the cross section. For this reason it is desirable to 'remove' the dependence on $W_{\pi\mathrm{N}}$ in the presentation of the cross section as a function of one of the ϕ variables. As described in section 2.5, this is done by dividing the weight of each measured and calculated event by a function that globally describes the overall $W_{\pi\mathrm{N}}$ dependence of the cross section, which results in the doubly-reduced cross section $d^5\sigma_{v2}$. This method is successful for the ^{4}He$(e,e'p\,^3$He$)\pi^-$ cross section, but it is less satisfactory for the ^{4}He$(e,e'p\,^3$H$)\pi^0$ reaction. In the latter case the cross section becomes almost zero as $W_{\pi\mathrm{N}}$ approaches the pion production threshold of 1073 MeV (cf. fig. 5.3), implying (infinitely) large weights for events in this region, which causes strange results. For this reason $d^5\sigma_{v2}$ is presented in fig. 5.9 only for charged pion production (right column) and the single reduced cross section $d^5\sigma_{v1}$ for both reaction channels (left and middle column). The cross sections are shown for the variables $\phi_{\pi,\mathrm{q}'}$ (top), Φ (middle) and $\Delta\Phi$ (bottom).

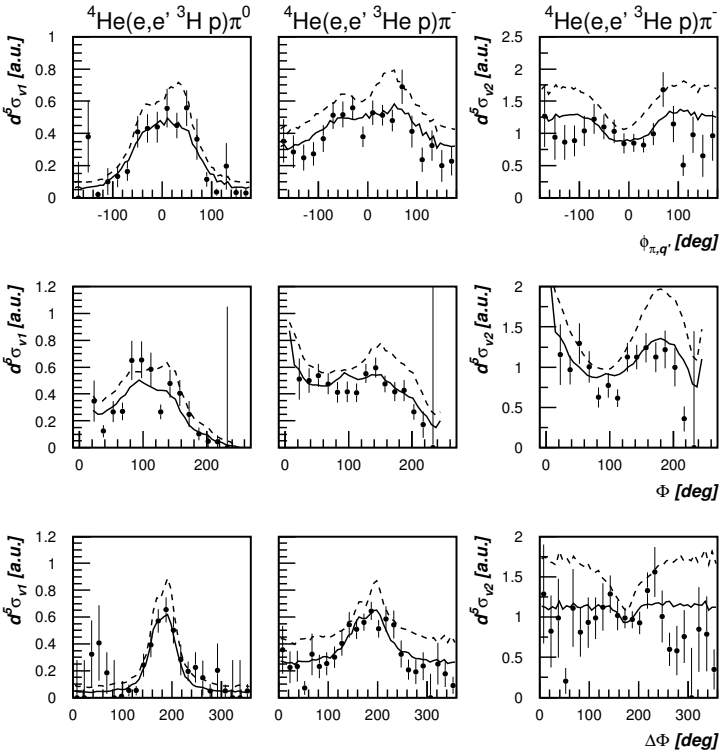

Figure 5.9: *The cross sections* $d^5\sigma_{v1}$ *for* $^4\mathrm{He}(e,e'p\,^3\mathrm{H})\pi^0$ *and* $^4\mathrm{He}(e,e'p\,^3\mathrm{He})\pi^-$ *(left and middle column) and* $d^5\sigma_{v2}$ *for* $^4\mathrm{He}(e,e'p\,^3\mathrm{He})\pi^-$ *(right column) as a function of* $\phi_{\pi,\mathrm{q}'}$ *(top),* Φ *(middle) and* $\Delta\Phi$ *(bottom). Only events with* $p_{\mathrm{rec}} \leq 180$ MeV/c *are used.*

Taking into account the statistical precision of the data and the approximation made for the p_{rec} and $W_{\pi\mathrm{N}}$ dependences, the agreement between the data and the calculated cross sections is in general satisfactory.

Dependence of $d^5\sigma_{v1}$ on $\phi_{\pi,\mathrm{q}'}$ for $^4\mathrm{He}(e,e'p\,^3\mathrm{H})\pi^0$ and $^4\mathrm{He}(e,e'p\,^3\mathrm{He})\pi^-$

The dependence of the measured cross section $d^5\sigma_{v1}$ on $\phi_{\pi,\mathrm{q}'}$ is well described by the DWIA calculations. As pointed out above, the dependence is dominated by the correlation between $\phi_{\pi,\mathrm{q}'}$ and $W_{\pi\mathrm{N}}$ in the detection volume; at $\phi_{\pi,\mathrm{q}'} = 0°$ the full $W_{\pi\mathrm{N}}$ range (threshold–1250 MeV) is covered, whereas at $\phi_{\pi,\mathrm{q}'} = \pm 100°$,

the maximum value of $W_{\pi\mathrm{N}}$ is 1100 MeV. This explains the difference between the shape of the $d^5\sigma_{v1}$ dependence for neutral and charged pion production: at $\phi_{\pi,\mathrm{q}'} = \pm 100^\circ$ the cross section is dominated by the Born terms, whose contribution is sizeable for charged pion production and almost zero for neutral pion production.

Dependence of $d^5\sigma_{v2}$ on $\phi_{\pi,\mathrm{q}'}$ for $^4\mathrm{He}(e,e'p\,^3\mathrm{He})\pi^-$

For the reaction $^4\mathrm{He}(e,e'p\,^3\mathrm{He})\pi^-$ the measured dependence of $d^5\sigma_{v2}$ on $\phi_{\pi,\mathrm{q}'}$ is fairly well described by the DWIA calculations. The structure in the data is well reproduced by the calculations in the range $-80^\circ < \phi_{\pi,\mathrm{q}'} < 80^\circ$. Outside this region there are deviations. This is due to the rapid decrease of the detection volume, giving rise to larger systematic errors, and to the uncertainties that were introduced by removing both the p_{rec} and $W_{\pi\mathrm{N}}$ dependence. The dependence of the data and calculations on $\phi_{\pi,\mathrm{q}'}$ is similar to that of the cross section for electroproduction of a pion on a nucleon as a function of $\phi_{\pi,\mathrm{q}}$ (in this case equal to $\phi_{\pi,\mathrm{q}'}$), which is determined (while keeping the other kinematic variables fixed) by the last two terms of eq. (2.10): a linear combination of $\cos(\phi_{\pi,\mathrm{q}})$ and $\cos(2\phi_{\pi,\mathrm{q}})$, for which, according to Lee's model, the coefficients $\frac{d^2\sigma_{\mathrm{LT}}}{d\Omega_\pi}$ and $\frac{d^2\sigma_{\mathrm{TT}}}{d\Omega_\pi}$ are predominantly negative within the detection volume. The behaviour of a function $A - B\cos(\phi_{\pi,\mathrm{q}}) - C\cos(2\phi_{\pi,\mathrm{q}})$ (with $A, B, C > 0$) is indeed similar to that of the shown PWIA and DWIA curves (upper right corner of fig. 5.9).

Dependence of $d^5\sigma_{v1}$ on Φ for $^4\mathrm{He}(e,e'p\,^3\mathrm{H})\pi^0$ and $^4\mathrm{He}(e,e'p\,^3\mathrm{He})\pi^-$

The cross section $d^5\sigma_{v1}$ measured as a function of Φ, is satisfactorily described by the DWIA calculations for both reaction channels. Within the detection volume there also exists a correlation between $W_{\pi\mathrm{N}}$ and Φ, albeit not as strong as the correlation between $W_{\pi\mathrm{N}}$ and the variables $\phi_{\pi,\mathrm{q}'}$ and $\Delta\Phi$: the larger values of $W_{\pi\mathrm{N}}$ correspond to $\Phi = 100^\circ$ and $W_{\pi\mathrm{N}}$ decreases with increasing values of $|\Phi - 100^\circ|$. The difference in the contribution of the Born terms to the cross section for the two reaction channels explains part of the differences between the respective $d^5\sigma_{v1}$ distributions, but not all.

Dependence of $d^5\sigma_{v2}$ on Φ for $^4\mathrm{He}(e,e'p\,^3\mathrm{He})\pi^-$

The eight-fold differential cross section can be expressed explicitly in terms of Φ, as is shown in eqs. (2.12)–(2.17). The linear combination of $\cos(\Phi)$, $\cos(2\Phi)$, $\sin(\Phi)$

and $\sin(2\Phi)$ terms in these expressions is mainly responsible for the oscillatory behaviour of the measured and calculated $d^5\sigma_{v2}$ distributions for charged pion electroproduction. The DWIA calculations describe the data well.

Dependence of $d^5\sigma_{v1}$ on $\Delta\Phi$ for ^{4}He$(e,e'p\,^3$H$)\pi^0$ and ^{4}He$(e,e'p\,^3$He$)\pi^-$

Again the DWIA calculations describe the measured cross section $d^5\sigma_{v1}$ as a function of $\Delta\Phi$ well for both reaction channels. As for the $\phi_{\pi,\mathrm{q}'}$ dependence, the $d^5\sigma_{v1}$ dependence on $\Delta\Phi$ is dominated by the correlation between $\Delta\Phi$ and $W_{\pi\mathrm{N}}$ in the detection volume; at $\Delta\Phi = 180°$ the full $W_{\pi\mathrm{N}}$ range is covered, whereas at $\Delta\Phi = 0°$ and $360°$, $W_{\pi\mathrm{N}}$ is smaller than 1100 MeV. Similarly to the $\phi_{\pi,\mathrm{q}'}$ dependence, this explains why the $d^5\sigma_{v1}$ dependence on $\Delta\Phi$ is different for the ^{4}He$(e,e'p\,^3$H$)\pi^0$ and ^{4}He$(e,e'p\,^3$He$)\pi^-$ reactions.

Dependence of $d^5\sigma_{v2}$ on $\Delta\Phi$ for ^{4}He$(e,e'p\,^3$He$)\pi^-$

Both the measured and calculated $d^5\sigma_{v2}$ distributions as a function of $\Delta\Phi$ show a dip at $\Delta\Phi = 180°$. The data are reasonably well described by the DWIA calculations, except for the region $\Delta\Phi > 270°$, where they are overestimated by the DWIA calculations. One should, however, keep in mind that this region is at the edge of the detection volume, where the statistical precision is small and the method of reducing the cross section twice introduces additional systematic errors. The difference between the results of the PWIA and DWIA calculations is notable and the data clearly give preference to the flat DWIA curves.

5.3 Summary

In this chapter the results have been presented for the three measured reaction channels, namely ^{4}He$(e,e'p\,^3$H$)$, ^{4}He$(e,e'p\,^3$H$)\pi^0$, and ^{4}He$(e,e'p\,^3$He$)\pi^-$. The momentum density for ^{4}He, obtained from the analysis of the *proton knock-out channel*, has been compared to the results of DWIA calculations. The observed difference of 5% between the data and the DWIA results is well within the systematic uncertainties in the data and the DWIA calculations. The parameters of the optical model that is used in these DWIA calculations, have been adjusted in such a way that they give a good description of ^{4}He momentum densities measured in independent experiments in various kinematic regimes [Bra88, Lee96].

The same potentials for the bound nucleon and the outgoing proton have been used in the DWIA calculations for the *pion production reaction channels*. The overall agreement between the pion electroproduction measurements and the DWIA calculations is good. In particular, this is true for the dependence of the cross section on $p_{\rm rec}$; the similarity between the shapes of the measured momentum density and the pion production cross sections as a function of $p_{\rm rec}$, shows that in first instance pion production can be considered as a quasi-free process.

The overall dependence of the cross section on $W_{\pi \rm N}$ is reproduced well by the DWIA calculations, exposing the difference in the relative contributions of the Born and Δ-resonance mechanisms to the neutral (mainly Delta) and charged (Born + Delta) pion production processes. On closer inspection, however, (large) deviations from the quasi-free description occur in the Delta region for $p_{\rm rec} > 180$ MeV/c.

The cross sections for neutral and charged pion production as a function of $\theta_{\pi,{\rm q}'}$ are fairly well described in the Born region ($W_{\pi \rm N} < 1160$ MeV), but, again, in the Delta region ($1160 < W_{\pi \rm N} < 1260$ MeV) the deviations are sizeable. These discrepancies also show up in the dependence of the cross section on T_π, which points in the direction of a non-adequate description of the pion waves. This can be interpreted as a hint that a Δ-hole model or a 'medium-modified' Delta propagator is needed in order to describe the experimental cross sections. In a recent study of the ^{3}He$(e,e'\pi^+)$ reaction [Koh02] it was found that the $\sigma_{\rm LT}$ term is very sensitive to medium modifications. This term is responsible for the asymmetric $\theta_{\pi,{\rm q}'}$ distributions, which are also observed in the present study, and thus supports the need for medium-dependent model parameters.

The good DWIA description of the dependence of the reduced cross sections on $\phi_{\pi,{\rm q}'}$, Φ, and $\Delta\Phi$ confirms that in general a quasi-free approximation is valid.

6 Summary

The Δ-resonance, the first excited state of the nucleon, plays a prominent role in reactions of nucleons with various probes, such as photons, electrons, pions and protons. In free space, this resonance decays almost exclusively into a pion and a nucleon. The properties of the Δ-resonance excited on a free nucleon have been measured to great detail in various studies of γN and πN reactions. However, much less is known about the excitation and decay of the Delta in a nucleus.

The experiment described in the present thesis was initiated in order to investigate the pion production mechanism inside a nucleus and the role of the Delta in this process. For this the reactions ^{4}He$(e,e'p\,^3$H$)\pi^0$ and ^{4}He$(e,e'p\,^3$He$)\pi^-$ were chosen. The ^{4}He nucleus provides a nuclear medium to the intermediate Delta with a density that is comparable to that of heavier nuclei. The reaction channels were measured simultaneously at the same experimental conditions. This enabled us to make a direct comparison between the production of neutral pions (predominantly via intermediate Deltas) and charged pions (with a sizeable contribution of non-resonant processes) and to address the question if the process can be described as a quasi-free mechanism. This is the first study in which the $(\gamma^*, p\pi^0)$ channel was investigated and the first time the $(\gamma^*, p\pi^-)$ channel was studied on ^{4}He.

The triple coincidence measurements were carried out at the Internal Target Facility at NIKHEF with 670 MeV electrons and cooled ^{4}He gas contained in an open-ended storage cell with a length of 40 cm. The scattered electrons were detected in the BigBite magnetic spectrometer and the knocked out protons in the HADRON4 detector. Simultaneous measurements of both reaction channels were achieved by detecting the recoiling ^{3}H and ^{3}He nuclei in the Recoil detector, which was positioned on the opposite side of the beam line with respect to the the three-momentum transfer vector $\mathbf{q}$. In this way the detection of neutral pions was avoided.

The BigBite electron spectrometer was positioned at an angle of 30° with respect to the beam line. The momentum acceptance of the spectrometer was set to 200–900 MeV/c, which made it possible to study simultaneously elastic

electron scattering, quasi-elastic electron scattering and pion electroproduction. At these settings the solid angle spanned by the detector was 96 msr and electrons scattered in the target within the range $-20 < z_{\mathrm{target}} < 20$ cm were accepted.

The recoiling nuclei, ^{3}H and ^{3}He, were detected with the Recoil detector. The central angle of this detector was 115° with respect to the direction of the beam. The average opening angle was 97 msr. The detector, which has been designed for the detection of nuclei with mass numbers $A \leq 4$ and kinetic energies of up to 40 (Z=1) or 80 (Z=2) MeV, consists of a low-pressure avalanche chamber, two sets of three segmented silicon strip detectors (SiX and SiY), and a plastic scintillator. Almost all Z=2 (^{3}He) particles of the triple coincidence events were stopped in the first silicon detector, i.e. SiX. Of the Z=1 (^{3}H) particles a fraction of 30%, having the highest energy, was stopped in the second silicon detector, SiY, while the rest was stopped in SiX. Due to high background radiation it was impossible to operate the avalanche chamber at the optimal high voltage, resulting in a lower and varying efficiency for the identification of particles stopping in SiX, especially the Z=1 particles. This efficiency was determined as a function of Z, kinetic energy, impact angle and time, using single arm events as well as events from the reaction $^4\mathrm{He}(e,e'p\,^3\mathrm{H})$. The average efficiency was 60% for Z=1 and 90% for Z=2 particles.

The emitted protons were detected with the HADRON4 detector. This detector is a segmented plastic scintillator array comprising a hodoscope for the determination of the impact position of the particles and five energy-measuring layers. Protons with energies in the range 25–248 MeV stop in either of these five layers. The detector was positioned at an angle of 53° with respect to the beam line on the side of $\mathbf{q}$ and covered a solid angle of 504 msr. The protons were identified using the ΔE-E method and their energies were determined using the signal in the layer in which they were stopped. The dead time of the HADRON4 front-ends was determined for each data file and a correction was made for variations in the beam current.

By exploiting the kinematic completeness of the measured reaction channels $^4\mathrm{He}(e,e'\,^4\mathrm{He})$, $^1\mathrm{H}(e,e'p)$ and $^4\mathrm{He}(e,e'p\,^3\mathrm{H})$, the alignment and energy calibration of the various detectors were checked. An offset in the determined vertex location was found, which was attributed to a misalignment of the detector package in the BigBite detector. A correction was made for this in the analysis. Besides this it was found that the beam energy had to be adjusted.

The pion production events were identified using the missing mass spectrum. The sizeable contribution to this spectrum of events from the radiative tail of the ^{4}He$(e,e'p\,^3$H) reaction could be largely removed by cutting away the events for which the missing momentum was collinear with the incoming and outgoing electron. The background in the pion missing mass peak due to events from the cell wall was negligible. After all cuts and corrections had been applied, about 500 neutral and 1200 charged pion production events were identified.

In order to extract cross sections the detection and trigger efficiencies of the three detectors were taken into account for each data file. The target density of $5.9 \cdot 10^{14}$ atoms/cm^2 was deduced from the counting rate for the ^{4}He$(e,e'\,^4$He) reaction, for which the cross section is well known. The resulting value for the integrated luminosity was $2.9 \cdot 10^8$ μb^{-1}. The detection volume was calculated by means of a Monte Carlo simulation for the three-detector setup.

The accuracy of the analysis was checked by analyzing the ^{4}He$(e,e'p\,^3$H) coincidence events, for which the cross section is well known in the kinematic regime covered by the experiment. The observed difference of 5% between the measured momentum density and the results from DWIA calculations is well within the various systematic uncertainties. The parameters of the bound state wave function of ^{4}He and of the optical model that is used in the DWIA calculations, were adjusted such that a good description was obtained for the ^{4}He momentum densities measured independently in various kinematic regimes by Van Leeuwe and Van den Brand.

The cross section for the reaction $A(e,e'p\pi)A-1$ depends on seven independent observables. The small number of triple coincidences in both reaction channels only allowed a presentation of the cross section as a function of one variable, while averaging over the other ones within the detection volume. The cross sections were presented as functions of the momentum of the recoiling nucleus $p_{\rm rec}$, the invariant mass of the πN system $W_{\pi \rm N}$, the angle $\theta_{\pi,{\rm q}'}$ between the transferred three-momentum to the πN system $\mathbf{q'}$ $(= \mathbf{q} - \mathbf{p}_{\rm rec})$ and the pion momentum, and the kinetic energy of the pion T_π. In addition the dependence of the cross sections on the azimuthal angles $\phi_{\pi,{\rm q}'}$, Φ, and $\Delta\Phi$ was studied. The data are compared with the results of DWIA calculations performed with the program of Lee *et al.* In these calculations the same potentials for the nucleons in the initial state and for the outgoing proton were used as for the ^{4}He$(e,e'p\,^3$H) study. The parameters for the pion optical potential were deduced from the analysis of πA scattering

data. Medium effects of the intermediate Delta are implicitly, but not explicitly, accounted for in these calculations.

The overall agreement between the pion electroproduction measurements and the DWIA calculations is good. In particular, this is true for the dependence of the cross section on $p_{\rm rec}$; the similarity between the shapes of the measured momentum density and the pion production cross sections as a function of $p_{\rm rec}$, shows that in first instance pion production can be considered as a quasi-free process.

The overall dependence of the cross section on $W_{\pi \rm N}$ is reproduced well by the DWIA calculations, exposing the difference in the relative contributions of the Born and Δ-resonance mechanisms to the neutral (mainly Delta) and charged (Born + Delta) pion production processes. In a more detailed analysis, however, deviations from a quasi-free reaction were observed in the Delta region for $p_{\rm rec} > 180$ MeV/c.

The cross sections for neutral and charged pion production as a function of $\theta_{\pi,{\rm q}'}$ are fairly well described in the Born region ($W_{\pi \rm N} < 1160$ MeV), but, again, in the Delta region ($1160 < W_{\pi \rm N} < 1260$ MeV) the deviations are sizeable. These discrepancies also show up in the dependence of the cross section on T_π, which points in the direction of a non-adequate description of the pion waves. This observation can be reconciled well with the results of a recent study of the ^{3}He$(e,e'\pi^+)$ reaction by Kohl *et al.*, in which it was found that the $\sigma_{\rm LT}$ term is very sensitive to medium modifications. This term is responsible for the asymmetric $\theta_{\pi,{\rm q}'}$ distributions, also observed in the present study. Hence, the discrepancy between the measured and calculated dependence of the cross sections on $\theta_{\pi,{\rm q}'}$ can be interpreted as a hint that a Δ-hole model or a 'medium-modified' Δ-propagator is needed in order to describe the experimental cross sections.

The good description of the dependence of the reduced cross sections on $\phi_{\pi,{\rm q}'}$, Φ, and $\Delta\Phi$ by the DWIA calculations is a further indication that a quasi-free reaction mechanism is appropriate to describe both reactions.

References

[Ahr00] J. Ahrens *et al.*, *Phys. Rev. Lett.* **84** (2000) 5950.

[Arn02] R.A. Arndt, W.J. Briscoe, I.I. Strakovsky, R.L. Workman, *Phys. Rev. C* **66** (2002) 055213.

[Ama79] E. Amaldi, S. Fubini, G Furlan, *Pion Electroproduction*, Springer-Verlag, Berlin 1979.

[Blo77] I. Blomqvist and J.M. Laget, *Nucl. Phys.* **A280** (1977) 405.

[Blo96] K.I. Blomqvist *et al.*, *Phys. Rev. Lett.* **77** (1996) 2396.

[Blo97] K.I. Blomqvist *et al.*, *Nucl. Phys.* **A626** (1997) 871.

[Bra88] J.F.J. van den Brand, *The Two-Body Electrodisintegration of* ^{4}He *Studied through the* $(e, e'\,\mathrm{X})$ *Reaction*, Ph.D. thesis, Universiteit van Amsterdam (1988).

[Bra99] D. Branford *et al.*, *Phys. Rev. C* **61** (1999) 014603.

[Bra02] D. Branford *et al.*, *Phys. Rev. C* **66** (2002) 015208.

[Bot99] T. Botto, *Coherent* π^0 *electroproduction on* ^{4}He *in the Delta region*, Ph.D. thesis, Vrije Universiteit Amsterdam (1999).

[Car82] J.A. Carr, H. McManus and K. Stricker-Bauer, *Phys. Rev. C* **25** (1982) 952.

[Car94] R.C. Carrasco *et al.*, *Nucl. Phys.* **A570** (1994) 701.

[Che57] G.F. Chew *et al.*, *Phys. Rev.* **106** (1957) 1345.

[Dav91] R.M. Davidson *et al.*, *Phys. Rev. D* **43** (1991) 71.

[Don84] T.W. Donnelly, Proceedings Newport News (Report CEBAF, 254–299) (1984) and references therein and in notes of lectures given at NIKHEF.

[Dre74] B. Dreher *et al.*, *Nucl. Phys.* **A235** (1974) 219.

[Eri88] T. Ericson and W. Weise, *Pions and Nuclei*, Clarendon press, Oxford 1988.

[For83] T. de Forest, Jr., *Nucl. Phys.* **A392** (1983) 232.

[Gea93] *GEANT Detector Description and Simulation Tool*, version 3.21/94b, CERN Program library 1993.

[Gom95] J.A. Gómez Tejedor, M.J. Vicente-Vacas, and E. Oset, *Nucl. Phys.* **A588** (1995) 819.

[Gro99] D.L. Groep *et al.*, *Phys. Rev. Lett.* **83** (1999) 5443.

[Gro00] D. Groep, *Correlations and Currents in* ^{3}He *Studied with the* $(e, e'pp)$ *Reaction*, Ph.D. thesis, Universiteit Utrecht (2000).

[Hig98] D.W. Higinbotham, *Nucl. Instr. and Meth. Phys. Res., Sect. A* **414** (1998) 332.

[Hir79] M. Hirata, J. H. Koch, F. Lenz and E. J. Moniz, *Ann. Phys.* **120** (1979) 205.

[Jan94] P.P.M. Jansweijer, M.G. van Beuzekom, J.C. Verkooijen, J. Stolte, A.T.H. van Reen, *Recoil Digitizer Module*, NIKHEF ETR 94–08.

[Kam01] S.S. Kamalov *et al.*, *Phys. Rev. C* **64** (2001) 032201(R).

[Koc83] J. H. Koch and E. J. Moniz, *Phys. Rev. C* **27** (1983) 751 and J. H. Koch and E. J. Moniz, *Phys. Rev. C* **20** (1979) 235.

[Koc84] J. H. Koch, E. J. Moniz, and N. Ohtsuka, *Ann. Phys.* **154** (1984) 99.

[Koh02] M. Kohl *et al.*, *Phys. Lett. B* **530** (2002) 67.

[Lan98] Dirk-Jan de Lange, *A study of collective aspects of* ^4He *electrodisintegration with the BigBite spectrometer*, Ph.D. thesis, Universiteit Utrecht (1998).

[Lan98a] D.J.J. de Lange *et al.*, *Nucl. Instr. and Meth. Phys. Res., Sect. A* **406** (1998) 182.

[Lan98b] D.J.J. de Lange *et al.*, *Nucl. Instr. and Meth. Phys. Res., Sect. A* **412** (1998) 254.

[Lee96] J.J. van Leeuwe, *Investigation of nucleon-nucleon correlations in* ^{4}He, Ph.D. thesis, Universiteit Utrecht (1996).

[Lee93] X. Li (F.X. Lee), L.E. Wright, and C. Bennhold, *Phys. Rev. C* **48** (1993) 816

[Lee97] Frank X. Lee, L.E. Wright, and C. Bennhold, *Phys. Rev. C* **55** (1997) 318.

[Leo94] W.R. Leo, *Techniques for Nuclear and Particle Physics Experiments*, Springer-Verlag, Berlin 1994.

[MCo96] M. MacCormick *et al.*, *Phys. Rev. C* **53** (1996) 41.

[MKe96] J.A. MacKenzie *et al.*, *Phys. Rev. C* **54** (1996) R6.

[MCa77] J.S. McCarthy *et al.*, *Phys. Rev. C* **15** (1977) 1396.

[MPh64] D.A. McPherson *et al.*, *Phys. Rev.* **136** (1964) B1465.

[Noz90] S. Nozawa *et al.*, *Phys. Rev. C* **41** (1990) 213.

[Ols75] M.G. Olsson and E.T. Osypowski, *Nucl. Phys.* **B87** (1975) 399.

[Ond98a] C.J.G. Onderwater *et al.*, *Phys. Rev. Lett.* **81** (1998) 2213.

[Ose79] E. Oset and W. Weise, *Nucl. Phys.* **A319** (1979) 477.

[Pas96] E. Passchier, *Electron scattering off an tensor-polarized deuterium target*, Ph.D. thesis, Universiteit Utrecht (1996).

[Pec69] R.D Peccei, *Phys. Rev.* **181** (1969) 1902.

[Pel99] A.R. Pellegrino *et al.*, *Nucl. Instr. and Meth. Phys. Res., Sect. A* **437** (1999) 188.

[Pha92] L.D. Pham *et al.*, *Phys. Rev. C* **46** (1992) 621.

[Poo99] H.R. Poolman, *Quasifree Spin-dependent Electron Scattering from a Polarized* ^{3}He *Internal Target*, Ph.D. thesis, Vrije Universiteit Amsterdam (1999).

[Qui88] E. Quint, *Limitations of the Mean-Field Description for Nuclei in the Pb-Region, Observed with the* $(e, e'p)$ *Reaction*, Ph.D. thesis, Universiteit van Amsterdam (1988).

[SAI03] The SAID database for the $^1\mathrm{H}(\gamma,\pi^+)n$ reaction, which contains data from among others refs. [Ahr00, MCo96, MPh64].

[Sam97] M.J.M. van Sambeek, *Study of coherent π^0 electroproduction on ^{4}He with recoil detection*, Ph.D. thesis, Vrije Universiteit Amsterdam (1997).

[Sam99] M.J.M. van Sambeek *et al.*, *Nucl. Instr. and Meth. Phys. Res., Sect. A* **434** (1999) 279.

[Sch82] P. Schwandt *et al.*, *Phys. Rev. C* **26** (1982) 55.

[Sta99a] R. Starink *et al.*, *Phys. Lett. B* **474** (2000) 33.

[Sta99] R. Starink, *Short-range correlations studied with the reaction $^{16}\mathrm{O}(e,e'pp)^{14}\mathrm{C}$*, Ph.D. thesis, Vrije Universiteit Amsterdam (1999).

[Str79] K. Stricker, H. McManus and J.A. Carr, *Phys. Rev. C* **19** (1979) 929.

[Tak88] T. Takaki and M. Thies, *Phys. Rev. C* **38** (1988) 2230.

[Ude97] M.A. van Uden, *The HARP liquid hydrogen system and a high resolution $^{16}\mathrm{O}(\gamma,\pi^-p)$ experiment*, Ph.D. thesis, Universiteit Utrecht (1997).

[Ude98] M.A. van Uden *et al.*, *Phys. Rev. C* **58** (1998) 3462.

[Vdh95a] M. Vanderhaeghen, L. Machenil, J. Ryckebusch, V. Van der Sluys, and M. Waroquier, *Exclusive reactions induced by real and virtual photons*, Proceedings of the Second Workshop on Electromagnetically induced Two-nucleon Emission, Gent, May 17–20 (1995) 137.

[Vdh95b] M. Vanderhaeghen, L. Machenil, J. Ryckebusch, V. Van der Sluys, and M. Waroquier, *Nucl. Phys.* **A595** (1995) 219.

[Vri84] C. de Vries *et al.*, *Nucl. Instr. and Meth. Phys. Res.* 223 (1984) 1.

[Wei79] G.L. Weissler and R.W. Carlson, *Vacuum physics and technology*, Methods of experimental physics 14, Academic Press, New York 1979.

[Wit93] P.K.A. de Witt Huberts, *Nucl. Phys.* **A553** (1993) 845c.

[Wri53] G.T. Wright, *Phys. Rev.* **91** (1953) 1282.

[Zwa96] A. Zwart and J.C. Verkooijen, *Hadron Digitizer Module*, NIKHEF ETR 96–07.

Samenvatting

Quasi-vrije pionelektroproduktie op ^{4}He in het gebied van de Δ-resonantie

De Δ-resonantie, de eerste aangeslagen toestand van het nucleon, speelt een belangrijke rol in reacties van nucleonen met fotonen, elektronen, pionen en nucleonen. Een ongebonden Delta vervalt vrijwel altijd in een pion en een nucleon. Dankzij verschillende γN en πN experimenten zijn produktie en verval van de 'vrije' Δ-resonantie goed bekend. Dit is echter veel minder het geval als de Delta zich in een kern bevindt.

Het experiment dat is beschreven in dit proefschrift is opgezet om meer te weten te komen over pionproduktie in een kern en de rol die de Delta daarin speelt. Hiervoor zijn de reacties $^4\mathrm{He}(e,e'p\,^3\mathrm{H})\pi^0$ en $^4\mathrm{He}(e,e'p\,^3\mathrm{He})\pi^-$ onderzocht. De dichtheid van de ^{4}He kern is vergelijkbaar met die van zwaardere kernen. Bovengenoemde reacties zijn tegelijkertijd gemeten onder dezelfde experimentele omstandigheden. Hierdoor was het mogelijk om een vergelijking te maken tussen de produktie van ongeladen pionen (overwegend met de Δ-resonantie als tussenstap) en die van geladen pionen (met een aanzienlijke bijdrage van niet-resonante processen). Tevens stelde het ons in staat te onderzoeken in welke mate de pionproduktie quasi-vrij kan worden genoemd. Dit is de eerste keer dat het reactiekanaal $(\gamma^*, p\pi^0)$ is onderzocht en bovendien is het de eerste keer dat het kanaal $(\gamma^*, p\pi^-)$ is bestudeerd op de kern ^{4}He.

De metingen werden uitgevoerd bij de "Internal Target Facility" van het NIKHEF. Er werd gebruik gemaakt van elektronen met een energie van 670 MeV en een trefplaat bestaande uit gekoeld ^{4}He gas. De impulsen van de verstrooide elektronen werden gedetecteerd met de "BigBite" elektronenspectrometer en die van de protonen in de HADRON4-detector. Beide reacties konden gelijktijdig bestudeerd worden door de ^{3}He en ^{3}H restkernen te detecteren in de "Recoil"-detector. Deze detector was geplaatst in de richting tegengesteld aan die van de

overgedragen impuls **q**. Door de restkernen te detecteren kon de detectie van ongeladen pionen worden vermeden.

De magnetische elektronenspectrometer was onder een hoek van 30° met de elektronenbundel geplaatst en bestreek een ruimtehoek van 96 msr. Dankzij de grote impulsacceptantie van 200–900 MeV/c was het mogelijk om gebeurtenissen afkomstig van elastische verstrooiing, quasi-vrije verstrooiing en pionproduktie gelijktijdig te registreren.

De Recoil-detector bevond zich onder een hoek van 115° met de elektronenbundel en in deze opstelling was de gemiddelde openingshoek 97 msr. Het bereik voor de kinetische energie is 0.5–40 MeV voor tritonen en 1.0–80 MeV voor ^{3}He kernen. De detector bestaat uit vier afzonderlijke detectoren, te weten een lage-druksdradenkamer, twee lagen met ieder drie silicium stripdetectoren en een plastic scintillator. Bijna alle ^{3}He kernen werden gestopt in de eerste silicium-laag (SiX). Van de ^{3}H kernen werd 30% gestopt in de tweede siliciumlaag, SiY, en de overige kernen, met lagere kinetische energie, in de eerste laag. Door de hoge achtergrondstraling tijdens het experiment was het onmogelijk om de dradenkamer te gebruiken bij de optimale hoogspanning. Dit heeft geresulteerd in een relatief laag rendement, dat ook niet constant was gedurende het experiment. Gemiddeld was het rendement voor de detectie van ^{3}H kernen 0.6 en van ^{3}He kernen 0.9.

De protondetector HADRON4 maakte een hoek van 53° met de bundellijn, aan dezelfde kant als de **q**-vector. De openingshoek van deze detector is 504 msr. Met deze detector konden protonen met kinetische energie in het bereik 25–248 MeV worden gemeten. De protonen zijn geïdentificeerd met behulp van de ΔE-E-methode. De dode tijd van de elektronica van HADRON4 werd bepaald voor elke 'data run' en werd tevens gecorrigeerd voor veranderingen in de bundelstroom tijdens het experiment.

Om de uitlijning en de energiecalibraties van de detectoren te kunnen controleren en corrigeren zijn er metingen gedaan aan de kinematisch overbepaalde reactiekanalen ^{4}He$(e,e'\,^4$He$)$, ^{1}H$(e,e'p)$ en ^{4}He$(e,e'p\,^3$H$)$. Uit de analyse van de metingen bleek dat de vertexpositie 1 cm verschoven was, hetgeen te wijten was aan een fout in de uitlijning van BigBite. Hiervoor werd gecorrigeerd in de analyse van de metingen. Bovendien bleek dat er een correctie nodig was op de energie van de elektronen in de bundel.

De reacties waarin een pion was geproduceerd konden worden herkend op grond van de verdeling van de zogenaamde 'ontbrekende massa'; deze werd gere-

construeerd door de impulsvectoren van de drie gedetecteerde deeltjes te combineren. De grote bijdrage van gebeurtenissen waarin het electron voor of na de ^{4}He$(e,e'p\,^3$H) reactie straling uitzendt kon grotendeels worden onderdrukt door te eisen dat de 'ontbrekende impuls' noch de richting van het inkomende elektron noch die van het verstrooide elektron had. De bijdrage, veroorzaakt door interacties met de wand van de ^{4}He buis, bleek verwaarloosbaar. Na correctie is het aantal gedetecteerde ongeladen en geladen pionen respectievelijk 500 en 1200.

De nauwkeurigheid van de analysemethode is getoetst aan de ^{4}He$(e,e'p\,^3$H) reactie. Voor deze reactie is de werkzame doorsnede goed bekend. Het verschil van 5% tussen de gemeten impulsdichtheid en de resultaten van DWIA-berekeningen ligt binnen de systematische fouten. Zowel de parameters voor de golffunctie van het gebonden nucleon in ^{4}He als de parameters in het optische model dat is gebruikt voor de DWIA-berekeningen zijn zodanig bijgesteld, dat de impulsdichtheden die zijn gemeten door Van Leeuwe *e.a.* en Van den Brand *e.a.* goed worden beschreven.

De differentiële werkzame doorsnede voor de reactie $A(e,e'p\pi)A-1$ hangt af van zeven onafhankelijke variabelen. Vanwege het kleine aantal gemeten gebeurtenissen voor beide reactiekanalen was het slechts mogelijk de afhankelijkheid van één variabele te onderzoeken, waarbij gemiddeld werd over de andere variabelen. Op deze manier is onderzocht hoe de werkzame doorsnede afhangt van de volgende grootheden: de impuls $p_{\rm rec}$ van de restkern, de invariante massa $W_{\pi\rm N}$ van het πN systeem, de hoek $\theta_{\pi,\rm q'}$ tussen de aan het πN systeem overgedragen impuls $\mathbf{q'}$ $(=\mathbf{q}-\mathbf{p}_{\rm rec})$ en de impuls van het pion, en de kinetische energie T_π van het pion. De afhankelijkheid van de werkzame doorsnede van de azimuthhoeken $\phi_{\pi,\rm q'}$, Φ en $\Delta\Phi$ werd ook bestudeerd. De gemeten werkzame doorsneden zijn vergeleken met de resultaten van DWIA-berekeningen die werden uitgevoerd met het programma van Lee *e.a.* In deze berekeningen werd dezelfde golffunctie voor de gebonden nucleonen gebruikt als in de berekeningen voor het reactiekanaal ^{4}He$(e,e'p\,^3$H) en ook is dezelfde optische potentiaal gebruikt voor het uitgestoten proton. De parameters voor de optische potentiaal voor het pion zijn ontleend aan πA verstrooiingsexperimenten. De invloed van het nucleaire medium op de tussentijds geproduceerde Delta is slechts op indirecte wijze verwerkt in de berekeningen.

Over het algemeen worden de gemeten werkzame doorsneden voor pionproduktie goed beschreven door de DWIA-berekeningen en in het bijzonder de afhankelijkheid van de werkzame doorsnede van $p_{\rm rec}$. De werkzame doorsnede voor pionproduktie als functie van $p_{\rm rec}$ komt qua vorm sterk overeen met de impuls-

dichtheid die is bepaald met de ^{4}He$(e,e'p\,^3$H) metingen. Dit wijst erop dat het pionproduktieproces grofweg als quasi-vrij bestempeld kan worden.

Verder wordt de $W_{\pi\mathrm{N}}$ afhankelijkheid van de werkzame doorsnede goed beschreven door de DWIA-berekeningen. Het verschil in de relatieve bijdragen van Born en Δ-resonantie processen aan de werkzame doorsneden voor ongeladen (vooral Delta bijdrage) en geladen (Born + Delta) pionproduktie is duidelijk waarneembaar. De $W_{\pi\mathrm{N}}$ afhankelijkheid van de werkzame doorsnede als functie van p_{rec} geeft echter duidelijk aan dat de benadering als quasi-vrij proces niet meer opgaat in het Δ-resonantie gebied voor $p_{\mathrm{rec}} > 180$ MeV/c.

De presentatie van de werkzame doorsneden voor beide reacties als functie van $\theta_{\pi,\mathrm{q}'}$ laat zien dat de metingen goed worden beschreven in het Born-gebied ($W_{\pi\mathrm{N}} < 1160$ MeV), maar dat er duidelijke afwijkingen zijn in het Delta-gebied ($1160 < W_{\pi\mathrm{N}} < 1260$ MeV). Soortgelijke verschillen zijn zichtbaar in de T_π afhankelijkheid van de werkzame doorsneden, hetgeen erop wijst dat de in de DWIA-berekeningen gebruikte golffuncties voor het pion mogelijk niet helemaal correct zijn.

Deze waarneming ligt in dezelfde lijn als de resultaten van een recent onderzoek naar de ^{3}He$(e,e'\pi^+)$ reactie door Kohl *e.a.*, waarin de sterke invloed van het nucleaire medium op de σ_{LT} term is aangetoond. Deze term bepaalt de gemeten asymmetrie in de $\theta_{\pi,\mathrm{q}'}$ verdelingen, die eveneens is waargenomen in het in dit proefschrift beschreven onderzoek. De verschillen tussen de gemeten en berekende $\theta_{\pi,\mathrm{q}'}$ afhankelijkheid van de werkzame doorsneden kunnen daarom worden opgevat als een aanwijzing dat een 'medium-modified' Δ-propagator, zoals bijvoorbeeld wordt gebruikt in een 'Δ-hole' model, vereist is voor een goede beschrijving van quasi-vrije pion uitstoot.

De gereduceerde werkzame doorsneden als functie van $\phi_{\pi,\mathrm{q}'}$, Φ en $\Delta\Phi$ worden goed beschreven door de DWIA-berekeningen. Dit bevestigt dat de reactie gedomineerd wordt door quasi-vrije uitstoot van pionen.

Nawoord

Lang heb ik naar het moment uitgekeken dat ik aan dit nawoord kon beginnen. Het onderzoek, waar ik enerzijds met veel plezier aan heb gewerkt, heeft ook veel bloed, zweet en tranen gekost en helaas niet alleen de mijne. Allen die mij geholpen, ondersteund en gemotiveerd hebben gedurende mijn onderzoek wil ik bij deze bedanken. Ook al zit het nawoord, zoals het een goed nawoord betaamt, een beetje verstopt achterin, staat dat geenszins symbool voor mijn waardering voor jullie. Bovendien weet ik uit ervaring dat bij de meeste mensen proefschriften automatisch bij het dankwoord openvallen.

Laten we aftrappen met (co)promotoren Henk, Willem en Ger. Willem, mede dankzij jouw geduld, enthousiasme en vertrouwen in mij *en* mijn data ben ik ook moeilijkere perioden te boven gekomen. Op de momenten dat mijn hoofd niet naar mijn onderzoek stond bood je me een luisterend oor, maar ook op het gebied van de pionenfysica heb ik veel aan je gehad. Jouw bijdrage aan dit proefschrift is op alle fronten zeer groot geweest! Henk, ook door jou heb ik me altijd zeer gesteund gevoeld. In jou denk ik de ideale mix tussen experimenteel en theoretisch fysicus te hebben aangetroffen en ik heb dan ook veel van je geleerd; je hebt me veel wijs(zer) kunnen maken. Ger, tijdens het grootste deel van mijn onderzoek was je door je drukke werkzaamheden als directeur van het NIKHEF wat meer op de achtergrond aanwezig, maar in de afrondende fase werd je rol als promotor (en aanjager) van je laatste promovendus steeds actiever. Ik waardeer het zeer dat je tijdens je emeritaat toch nog bereid was mijn promotie op je te nemen.

Het pionproduktie experiment dat uiteindelijk heeft geleid tot dit boekje is (het lijkt alweer een eeuwigheid geleden) kundig uitgevoerd door Blaine, David, Dirk-Jan, Doug, Eddy, Gail, Henk, Hans, Igor, Junho, Louk, Luminita, Marcel van B, Peter, Ronald, Thomas, Tjeerd en Willem H. Thanks a heap! We hebben het ons destijds zeker niet gemakkelijk gemaakt; de fotomultiplier buizen van de Čerenkov detector gedroegen zich niet zoals gewenst en pas na het sjouwen van vele loodblokken werd het wat rustiger in de dradenkamers van de BigBite detector. De HADRON4 detector werd verplaatst van de EMIN hal, waar hij zich altijd zo thuis had gevoeld, naar ITH, met alle problemen van dien. Gelukkig

hebben Eddy en Willem uiteindelijk alle problemen kunnen oplossen (bedankt !). Verder bleek het niet eenvoudig de dradenkamer van de Recoil detector op de gewenste spanning te houden, ondanks uitgebreide lekkentests, hoge isobutaan-verversingssnelheden (mooi woord), water- en zuurstoffilters, builen gevuld met argon etc. etc. Fortunately, I could lean on the Recoil-detector guru, Peter Heimberg, with whom I've spent a few 24 hour shifts in order to get the wire chamber leakage free. Peter, I've really appreciated your dedication to the project, persisting even when you were about to become father for the second time (or third, if you count the Recoil detector among your children). Bedankt, hoor!

Wat betreft de technische ondersteuning voor de Recoil en HADRON4 detectoren heb ik veel te danken gehad aan Frans Mul (bedankt voor de mooie tekeningen van de 125° flens) en Frans Sturm. De stabiele elektronenbundel was te danken aan de versnellergroep van Ber, in het weekend vooral aan Herman. Tot aan het experiment was ik kind aan huis bij de vacuumafdeling van het NIKHEF (met name bij Onno en Edwin), wier lekkentesters ik tot het uiterste heb gedreven (en soms nog tot meer dan dat).

Mijn dagelijkse leven op het NIKHEF speelde zich vooral af binnen de EMIN groep en in het bijzonder op de kamer die ik tot mijn grote genoegen deelde met Jochen. Bedankt, Jochen, voor de muzikale intermezzo's, voor de heftige (althans van mijn kant) discussies over voetbal en geschiedenis, voor de tocht naar de totale zonsverduistering, kortom voor de gezellige tijd die we samen doorgebracht hebben. Bij Marcel van B. kon ik altijd terecht voor theoretische vraagstukken, discussies over het al dan niet Keltisch zijn van de stam der Batavieren (ik geloof, dat inmiddels dubbel en dwars is aangetoond dat de Batavieren van boven tot onder Germaans waren) en voor sprints op de fiets richting de Bijlmer. Hartelijk dank daarvoor. Tevens wil ik me nog verontschuldigen voor mijn afwezigheid op jouw promotie, maar ja, mijn zoontje had er nu eenmaal zijn zinnen gezet om op *die* dag geboren te worden. David G. en Ronald, jullie vormden onze lokale helpdesk op het gebied van alles wat met computers te maken had: aan jullie hebben we het voortreffelijke analyse 'framework' ADAM te danken, een groot deel van de HADRON analyse software en (vermoedelijk) de installatie van XBlast. Zoals zovelen heb ik blindelings unix login profiles en LaTeX style files van jullie gecopiëerd. Dank jullie wel. David, jou wil ook nog bedanken voor het wekken van mijn interesse voor het EDG project, waar ik inmiddels al twee en een half jaar voor werk. Pablo, thanks for the lessons about particular Spanish expressions and good luck with your thesis project. Ondanks dat (club-)voetbal

natuurkundigen over het algemeen koud laat, heb ik er toch twee gevonden die er warm voor kunnen lopen: Laurens en Niels. En gelukkig support geen van beiden de plaatselijke voetbalvereniging! Laurens, bedankt voor het bieden van enig tegenwicht in de discussies en voor je hulp bij onze verhuizing. Niels, geboren PSVer, de 'successen' van onze club boden regelmatig gespreksstof. Bedankt voor het optreden als klankbord. Voor Rood-Wit gezongen ...
Verder wil ik Beni, Chiara, David B., Dirk-Jan, Doug, Ed, Eddy, Gerco, Hans, Hans-Roeland, Henk, Henk-Jan, Igor, Jo, Jos, Louk, Marcel van S., Marco, Massi, Maurice, Paul, Peter, Tancredi, Vladas, Willem H. en Willem K. bedanken voor de gezellige jaren bij EMIN.

De laatste jaren heb ik gewerkt in de CT groep in het kader van het "EU Datagrid" (EDG) project. Ik heb het daar uitstekend naar mijn zin en wil daar Antony, Arjen, David G (alwéér), Gerben, Hui, Jason, Jeff, Kors, Krista (op naar Harry Potter 6!), Oscar, Paul, Willem van L., Wim H., Wim S. de C. en Ton hartelijk voor bedanken. Wim H., ik wil je ervoor bedanken dat ik eveneens heb mogen werken aan mijn proefschrift!

Mijn dank gaat ook uit naar mijn lieve ouders en zusje, die voortdurend voor morele steun hebben gezorgd.

De laatste woorden zijn voor Merian en Arne: de afgelopen drie jaar van mijn onderzoek waren niet altijd gemakkelijk en ik weet zeker dat ik het zonder jullie niet had gered. Lieve Merian en Arne, ik houd van jullie.